Title
Characterization of nanostructured materials for lithium-ion batteries and electrochemical capacitors

Author
Augustyn, Veronica

Publication Date
2013

Peer reviewed|Thesis/dissertation

UNIVERSITY OF CALIFORNIA

Los Angeles

Characterization of nanostructured materials for lithium-ion batteries and electrochemical capacitors

A dissertation submitted in partial satisfaction of the requirements for the degree Doctor of Philosophy in Materials Science and Engineering

by

Veronica Augustyn

2013

ABSTRACT OF THE DISSERTATION

Characterization of nanostructured materials for lithium-ion batteries and electrochemical capacitors

by

Veronica Augustyn

Doctor of Philosophy in Materials Science and Engineering

University of California, Los Angeles, 2013

Professor Bruce S. Dunn, Chair

In this dissertation, nanostructured materials are examined for electrochemical energy storage devices with high energy and power densities. While previous research on nanostructured materials for energy storage has mostly focused on the effects of reduced dimensionality on diffusion distances, the research presented here demonstrates how nanostructuring can lead to new charge storage mechanisms. The first part of the dissertation describes the low-potential reactivity of V_2O_5 aerogels and how nanostructuring leads to significantly improved reversibility of the charge storage process. The second part details the rapid kinetic response of *T*-Nb_2O_5 and in addition, how the combination of nanostructure and appropriate crystalline structure leads to a mechanism called intercalation pseudocapacitance. The third part examines how a 2D nanosheet morphology changes both the redox potentials and kinetics of lithium ion storage in TiO_2. These investigations underscore how reducing a material's dimensions and morphology lead to unique electrochemical behavior beyond simple decreasing of diffusion distances, and how such structures could lead to ultimately higher energy and power density electrochemical energy storage devices.

The dissertation of Veronica Augustyn is approved.

Yunfeng Lu

Vidvuds Ozolins

Bruce S. Dunn, Committee Chair

University of California, Los Angeles

2013

To my Parents, Elizabeth and Edward Augustyn and

my Husband, Alexander Bataller

Table of Contents

List of Figures

List of Tables

Acknowledgements

I would like to thank my advisor, Professor Bruce Dunn, for his wonderful mentorship over the past 6 years. Electrochemical energy storage was quite foreign to me when I came to UCLA, but with his enthusiasm and continuous guidance I have developed my own passion for this field. My growth as a researcher is entirely due to the high standards, creativity, and team work fostered by Prof. Dunn in his lab. I was very fortunate to complete my Ph.D. in Prof. Dunn's lab, as in addition to the exciting research opportunities I was also encouraged to participate in outreach activities which included travelling to Ethiopia as part of the U.S.-Africa Materials Initiative. None of these opportunities would have been possible without the support of Prof. Dunn.

Through Prof. Dunn I have had the chance to collaborate with a number of faculty members at UCLA, including my dissertation committee: Prof. Yunfeng Lu, Prof. Vidvuds Ozolins, and Prof. Sarah H. Tolbert. Thank you for your time and assistance in evaluating my dissertation. I would like to thank my collaborators at the Université Paul Sabatier: Prof. Patrice Simon, Dr. Pierre-Louis Taberna, and Dr. Jérémy Come; Cornell University: Dr. Michael Lowe and Prof. Héctor Abruña; and at UCLA: Prof. George Grüner, Dr. Zheng Chen, Dr. Shun Wan, and Dr. Iris Rauda. I would also like to thank Dr. Debra Rolison (Naval Research Laboratory) for her research and career advice.

I thank my labmates in the Dunn Lab who helped make this research possible, especially: Dr. John Wang, Dr. Peter Malati, Dr. Nicolas Cirigliano, Dr. Grant Umeda, Dr. Steven Jonas, Wade Richardson, Prof. Erik Menke, Dr. Hyun Cheol Lee, Dr. Esther Lan, Dr. Jong Woung Kim, Daniel Membreno, Dr. Julien Polleux, Dr. Emilie Perre, Jesse Kim, and Hyungseok Kim. Dr. Wang introduced me to electrochemistry in his characteristic simple and elegant teaching style. Dr. Malati taught me about mechanical and electrical systems during the great glovebox rebuild of 2010. Dr. Cirigliano was always happily available to philosophize

about electrochemistry and puzzling results. Dr. Grant Umeda and Dr. Steven Jonas continually advise me on career options and I learn much from their great examples.

I would like to thank my internship mentors, Dr. Ping Liu of HRL Laboratories (currently ARPA-E) and Prof. Philippe Barboux of the ENSCP. I would also like to thank Dr. Ignacio Martini, Dr. Sergey Prikhodko, Laurie Ultan-Thomas, Patti Barrera, and Dr. Jia Ming Chen for their help during my time at UCLA.

I would like to thank my Family and Friends for being there for me, whether it was after a hard day in the lab or a happy day celebrating exciting results. During the course of my graduate studies, my amazing Husband, Alex, wore many hats, from psychologist to chef to cheerleader to airport chauffeur. I cannot thank him enough for doing all this while working hard on completing his Ph.D. My Parents, Edward and Elizabeth, instilled in me that lifetime learning and hard work were admirable qualities. My Mom taught me how to read and didn't bat an eye at jars filled with snails and other childhood experiments that first engendered my love of science. My Siblings, Caroline, Alex, and Renata, always supported me and we shared many a road trip driving back to Chicago from wherever my research and education took me. I would also like to thank my friends, especially Wade, Jessica, and Mikhail, for the camping getaways, karaoke and happy hours in Westwood. I thank my yoga teacher, Joan Moran, for her inspiring practice and wisdom.

Chapter 4, "Conversion reactions in V_2O_5 aerogels" is a modified version of the published work "Low-potential lithium-ion reactivity of vanadium oxide aerogels" by myself and Prof. Bruce Dunn in *Electrochimica Acta* (doi: 10.1016/j.electacta.2012.10.145). The TEM images were taken by Dr. Hyun Cheol Lee.

Chapter 6, "Pseudocapacitive behavior in *T*-Nb_2O_5" is a modified version of the published work "The effect of crystallinity on the rapid pseudocapacitive response of Nb_2O_5" by Dr. Jong Woung Kim, myself, and Prof. Bruce Dunn in *Advanced Energy Materials* (doi:

10.1002/aenm.201100494). The synthesis and physical characterization of Nb_2O_5 were carried out by Dr. Jong Woung Kim.

Chapter 7, "Intercalation pseudocapacitance in *T*-Nb_2O_5" is a modified version of the published work "High-rate electrochemical energy storage through Li^+ intercalation pseudocapacitance" by myself, Dr. Jérémy Come, Dr. Michael A. Lowe, Dr. Jong Woung Kim, Dr. Pierre-Louis Taberna, Prof. Sarah H. Tolbert, Prof. Héctor D. Abruña, Prof. Patrice Simon, and Prof. Bruce Dunn in *Nature Materials* (doi: 10.1038/nmat3601). The electrochemistry on the thick Nb_2O_5 electrode was performed by Dr. Jérémy Come and the *in situ* X-ray absorption was carried out by Dr. Michael Lowe.

Chapter 8, "Pseudocapacitance in TiO_2 nanosheets" is a manuscript for submission prepared with Prof. George Grüner and Prof. Bruce Dunn. The HR-TEM and ED images were taken by Dr. Sergey Prikhodko. The TEM images were taken by Hyungseok Kim.

In Chapter 10, "Future work on metal organic frameworks for EES," the synthesis and physical characterization of the Cu-CAT were performed by Dr. Shun Wan.

This research was supported by the National Science Foundation (NSF) Integrative Graduate Education and Research Traineeship Program (IGERT): Materials Creation Training Program (MCTP), the Center for Molecularly Engineered Materials (MEEM), an Energy Frontier Research Center funded by the U.S. Department of Energy, Office of Science, Office of Basic Energy Sciences, and the Office of Naval Research (ONR).

Vita

2005	*Intern*, Faculty and Student Teams (FaST) Program
	Pacific Northwest National Laboratory, Richland, Washington
2005-2007	*Teaching Assistant*, Department of Materials Science and Engineering
	The University of Arizona, Tucson
2007	*B.S. in Materials Science and Engineering*
	The University of Arizona, Tucson
2007-2012	*Graduate Student Researcher*, Department of Materials Science and Engineering
	University of California, Los Angeles
2008-2010	*Trainee*, Materials Creation Training Program (MCTP)
	National Science Foundation Integrated Graduate Education and Research Training (IGERT) Program
2008-2013	*Member*, High School Nanoscience Institute Outreach Program
	California NanoSystems Institute
2009	*Intern*, HRL Laboratories, Malibu, California
2010	*M.S. in Materials Science and Engineering*
	University of California, Los Angeles
2012	*Visiting Graduate Student Researcher*
	École nationale supérieure de chimie de Paris, France
2012-2013	*Dissertation Year Fellowship,* University of California, Los Angeles
2012	*Fellow*, Joint U.S.-Africa Materials Initiative, Addis Ababa, Ethiopia

Publications

1. **V. Augustyn**, J. Come, M.A. Lowe, J.W. Kim, P.-L. Taberna, S.H. Tolbert, H.D. Abruña, P. Simon, and B. Dunn. "High rate electrochemical energy storage via Li^+ intercalation pseudocapacitance." *Nature Materials*, 12 (2013) 518.

2. I. Rauda, **V. Augustyn**, B. Dunn, and S.H. Tolbert. "Enhancing pseudocapacitive charge storage in polymer templated mesoporous materials." *Accounts of Chemical Research*, 46 (2013) 1113.

3. **V. Augustyn** and B. Dunn. "Low-potential lithium-ion reactivity of vanadium oxide aerogels." *Electrochimica Acta*, 88 (2013) 530.

4. M. Hmadeh, Z. Lu, Z. Liu, F. Gándara, H. Furukawa, S. Wan, **V. Augustyn**, R. Chang, L. Liao, F. Zhou, E. Perre, V. Ozolins, X. Duan, B. Dunn, Y. Yamamoto, O. Terasaki, and O.M. Yaghi. "New porous crystals of extended metal-catecholates." *Chemistry of Materials*, 24 (2012) 3511.

5. I. Rauda, R. Buonsanti, L.C. Saldarriaga-Lopez, K. Benjauthrit, L.T. Schelhas, M.M. Stefik, **V. Augustyn**, J. Ko, B. Dunn, U. Wiesner, D.J. Milliron, and S.H. Tolbert. "A general method for the synthesis of hierarchical nanocrystal-based mesoporous materials." *ACS Nano*, 6 (2012) 6386.

6. E.R. White, S.B. Singer, **V. Augustyn**, W.A. Hubbard, M. Mecklenburg, B. Dunn, and B.C. Regan. "*In situ* transmission electron microscopy of lead dendrites and lead ions in aqueous solution." *ACS Nano*, 6 (2012) 6308.

7. Z. Chen, **V. Augustyn**, X. Jia, Q. Xiao, B. Dunn, and Y.F. Lu. "High-performance sodium-ion pseudocapacitors based on hierarchically porous nanowire composites." *ACS Nano*, 6 (2012) 4319.

8. J.W. Kim, **V. Augustyn**, and B. Dunn. "The effect of crystallinity on the rapid pseudocapacitive response of Nb_2O_5." *Advanced Energy Materials*, 2 (2012) 141.

9. X. Wang, G. Li, Z. Chen, **V. Augustyn**, X. Ma, G. Wang, B. Dunn, and Y.F. Lu. "High-performance supercapacitors based on nanocomposites of Nb_2O_5 nanocrystals and carbon nanotubes." *Advanced Energy Materials*, 1 (2011) 1089.

10. Z. Chen, **V. Augustyn**, J. Wen, Y.W. Zhang, M.Q. Shen, B. Dunn, and Y.F. Lu. "High-performance supercapacitors based on intertwined CNT/V_2O_5 nanowire nanocomposites." *Advanced Materials*, 23 (2011) 791.

11. **V. Augustyn** and B. Dunn. "Vanadium Oxide Aerogels: Nanostructured Materials for Enhanced Energy Storage." *Comptes Rendus Chimie*, 13 (2010) 130.

Chapter 1. Objectives and Introduction

The need for more abundant, clean, secure, and efficient energy is one of the most serious social and engineering issues of our time. This is due to the combination of declining fossil fuels, the increasing climate concerns associated with the use of these fuels, and the growing global population. Much of the population growth is expected to occur in Africa and Asia, areas that have heretofore not contributed greatly to the global energy consumption. Electrochemical energy storage (EES) can play a large role in the newly developing energy landscape provided that some long-standing challenges are overcome. Many of these issues relate to the need for new materials as indeed "technology is always limited by the materials available."[1]

Figure 1.1. Cartoon from 1993 depicting the emerging use of portable electronics and the need for better EES devices. Reproduced from Ref. 2.

The primary objective of this research is to characterize the behavior of lithium-ion charge storage mechanisms in nanodimensional solids. One of the major issues affecting EES devices is low energy density, particularly for transportation applications. Charge storage reactions that involve multiple electrons result in high capacities. Due to structural

considerations, however, intercalation reactions in transition metal oxides rarely result in the storage of more than one electron per transition metal. To access further redox states, highly reducing potentials as well as significant structural changes are usually necessary. In the first part of the dissertation, the low-potential reactivity of V_2O_5 aerogels is investigated for high capacity lithium storage reactions involving multiple redox states. Another major issue for certain energy storage devices is low power density. Many applications require intermittent energy storage, with cycles on the order of seconds or minutes, as in regenerative braking. The second part of the dissertation details charge storage reactions that occur due to the fast pseudocapacitive response of orthorhombic Nb_2O_5 nanocrystals. With these materials, there is the possibility of designing energy storage materials for both high power and high energy densities. The third part of the dissertation presents the electrochemical behavior of TiO_2 nanosheets, materials that are molecular-layer thick, to explore whether the confinement of crystal growth in one dimension leads to unique charge storage behavior. Last, the preliminary results on the charge storage behavior of copper catecholate metal organic frameworks is described.

The desire to increase the capacity of lithium-ion energy storage devices led to the consideration of the low potential (*vs.* Li/Li^+) reactivity of V_2O_5 aerogels. Although V_2O_5 is a well-known electrochemical material that serves as a positive electrode in lithium-ion batteries, its behavior at lower potentials (below 1 V) is not well-known. The V_2O_5 aerogel was electrochemically lithiated to 0.1 V *vs.* Li/Li^+, the lowest safe voltage possible before lithium plating begins to occur on the surface of the electrode. The high capacity of 800 mAh g^{-1} achieved after cycling to such reducing potentials was reversible, and represented the storage of more than 5 Li^+/V_2O_5. The goals of this study were to elucidate the reaction mechanism responsible for such high capacity and reversibility.

A second research area focused on high rate energy storage reactions, those occurring through capacitive mechanisms. The electrochemical behavior of Nb_2O_5 nanocrystals was

characterized through cyclic voltammetry, and several analysis techniques were developed to understand the pseudocapacitive behavior. The goal of this study was to determine whether pseudocapacitive behavior was an inherent property of nanostructured orthorhombic Nb_2O_5, and also to further understand the behavior of intercalation pseudocapacitance in non-aqueous lithium-ion electrolytes.

The next research area has to do with the electrochemical characterization of TiO_2 anatase nanosheets. Nanosheet structures, where a particular crystal facet is exposed, provide an excellent experimental system in which to investigate the effect of the surface on charge storage behavior. TiO_2 nanosheets with a thickness of ~7.6 Å were synthesized and their electrochemical behavior examined in a lithium-ion electrolyte. The nanosheets had significantly faster kinetics than the nanocrystal counterparts, and even exhibited some capacity for the storage of sodium ions.

In the final research area, the idea of designing energy storage materials from the bottom-up is explored. The ability to tailor properties by selecting appropriate linkers and metals to form a networked structure could lead to new, inexpensive energy storage materials. Currently, the behavior of copper catecholates in non-aqueous electrolytes is being investigated. The cyclic voltammetry results indicate that there are several reversible redox processes active in this material.

This dissertation covers four separate and yet interrelated topics. The first part describes the characterization of V_2O_5 aerogel electrodes at low potentials. This work represents the first report of a very high reversible capacity in this material, 800 mAh g^{-1}, indicating the storage of more than 5 Li^+/V_2O_5. The second part details a study of the exciting transport properties of Nb_2O_5 nanocrystals. Nb_2O_5 may represent a model system that exhibits intercalation pseudocapacitance. The third part describes the unique electrochemical behavior of TiO_2 nanosheets where the very thin 2D material exhibits different properties from nanocrystals. The fourth part describes progress on designing metal organic frameworks for energy storage. Metal

organic frameworks are well-known network solids but their charge-storage properties have received very limited study.

Chapter 2. Electrochemical Energy Storage

2.1 Historical Perspective

As this dissertation considers materials for both electrochemical capacitors and batteries, it is useful to look at the historical development of these two technologies. While the idea that some materials could be "charged" was known since ancient times- for example, amber that was rubbed with a cloth would attract small particles (interestingly, the Greek word for amber is elektron)[3]— the reason for this attraction would not be known until the 19th century. The first capacitors, known as Leyden jars (Figure 2.1), were built independently by von Kleist and van Musschenbroek in the mid-18th century. The full understanding of capacitive charge storage would not emerge until much later.

Figure 2.1. Leyden jar, Museé des Arts et Métiers, Paris.

The study of electrochemistry, and the dawn of electricity, began in the late 18th century when Luigi Galvani noted that a frog's leg twitched when touched with a charged metal scalpel. This discovery led Alessandro Volta to develop the first battery, called the Volta pile (Figure 2.2), which consisted of alternating disks of copper and zinc separated by salt water soaked cardboard

or felt. The discovery of the Volta pile was a gateway for the field of electrochemistry which enjoyed a renaissance in the early 19th century. At the time, the Volta pile was the only way to generate a consistent direct current and voltage. The Volta pile led to the discovery of the electrolysis of water (1800, Nicholson & Carlisle) and to the discoveries, within several years (1807-1808), of sodium, potassium, calcium, boron, barium, strontium, and magnesium by Humphry Davy. Michael Faraday used the Volta pile to develop his 1st and 2nd laws of electrochemistry.[4]

Figure 2.2. Volta pile, Museé des Arts et Métiers, Paris.

The early impact of the Volta pile was to enable a number of important scientific discoveries, as noted above. The importance of electrochemical energy as a power source did not emerge until the 20th century when electronic devices, first as simple electric bells but later as complex integrated circuits in computers, became ubiquitous. It is interesting to note that most of the battery technologies in use or development today were invented in the previous two centuries, the exception being the lithium-ion battery (Table 2.1).

Table 2.1. Development of various battery technologies. Adapted from Ref. 5.

Inventor	Technology	Year
A. Volta	First battery	1800
A. Smee	Metal air batteries	1840
G. Plante	Lead acid battery	1859
G. Leclanché	Zn-MnO_2 primary battery	1868
T. deMichalowski	Ni-Zn battery	1899
W. Jungner	Ni-Cd battery	1901
Multiple inventors	Li-ion battery	1991

The development of electrochemical capacitors came much later than batteries- more than a century. The first electrochemical capacitor was developed in 1957 when a patent was granted to General Electric for electrical energy storage through the electric double layer at a porous carbon electrode.[6] Pseudocapacitance was first described in 1971 for RuO_2 by Trasatti and Buzzanca[7] while the theoretical understanding was further developed by Conway.

2.2 Fundamentals of Electrochemical Energy Storage with Batteries and Electrochemical Capacitors

2.2.1 Thermodynamics of Electrochemical Energy Storage

EES involves the storage of charge, either directly through electrostatic interactions or indirectly through chemical bonds, on two electrode surfaces separated by an electrolyte. Batteries store electrical energy faradaically, or through the formation of chemical bonds through oxidation/reduction reactions that involve electron transfer. Capacitors store electricity non-faradaically, so that the energy storage does not involve electron transfer and is electrostatic in nature. In either device, the total energy stored (G) is an integral function of the overall capacity (Q) and voltage (E):

$$G = \int Q dE \tag{2.1}$$

The relationship between capacity and voltage is fundamentally different for batteries and capacitors. This is entirely due to the fact that faradaic reactions utilized in batteries often result in a phase transformation when an electrode material transforms from the oxidized to the reduced form:

$$O + ne^- \leftrightarrow R \tag{2.2}$$

The coexistence of two phases leads to a constant potential according to the Gibbs Phase Rule:

$$F = C\text{-}P+2 \tag{2.3}$$

where F is the number of degrees of freedom, C is the number of components, and P is the number of phases in thermodynamic equilibrium. In the two-phase equilibrium described above (C = 2, P = 2), F is 2 so that if the temperature and pressure of the reaction are fixed, then there are no degrees of freedom left and the reaction potential is constant. This means that for an ideal battery with an invariant potential, the total stored energy is simply:

$$G = QE \tag{2.4}$$

The theoretical (or maximum) capacity of a battery material can be determined by knowing the redox reaction taking place and from using Faraday's laws of electrolysis which state that:

$$Q = Fn/M \tag{2.5}$$

where F is the Faraday constant (96,485 C mol^{-1}), n is the number of electrons transferred, and M the molar mass of the material. The potential of a battery material (assuming activities of 1 for a standard potential, E^o) is directly related to the Gibbs energy change (ΔG) of the redox reaction and thus the chemical potential change ($\Delta\mu$) upon reduction:[8]

$$E^o = -\Delta G/nF = -\Delta\mu/nF \tag{2.6}$$

This relationship forms the basis of the Nernst equation, which also accounts for different activities of the materials involved in the redox reaction.

As no charge transfer occurs in a capacitor, no phase transformations occur and the relationship between the potential and capacity is linear:

$$\Delta E = Q/C \tag{2.7}$$

The proportionality constant, C, is the capacitance. Thus for an ideal capacitor, including electrochemical capacitors based on the electric double layer, the capacitance remains constant over the entire operation potential. As a result of this linear change in capacity with potential, the energy stored by a capacitor can be written as:

$$G = \tfrac{1}{2}\, CE^2 = \tfrac{1}{2}QE \tag{2.8}$$

In a capacitor, the potential is no longer related to the chemical potential and instead is dependent upon the stable potential window of the electrolyte. The capacitance is dependent upon the structure of the electrode material as well as the properties of the electrolyte:[9]

$$C = A\varepsilon/d \tag{2.9}$$

where A is the surface area of the electrode material, ε is the relative permittivity of the electrolyte, and d is the thickness of the electric double layer.

The fundamental difference between batteries and capacitors based on their relationship with potential is shown in Figure 2.3. This figure demonstrates several of the important fundamental differences between faradaic and non-faradaic charge storage, and what these differences mean for device applications.

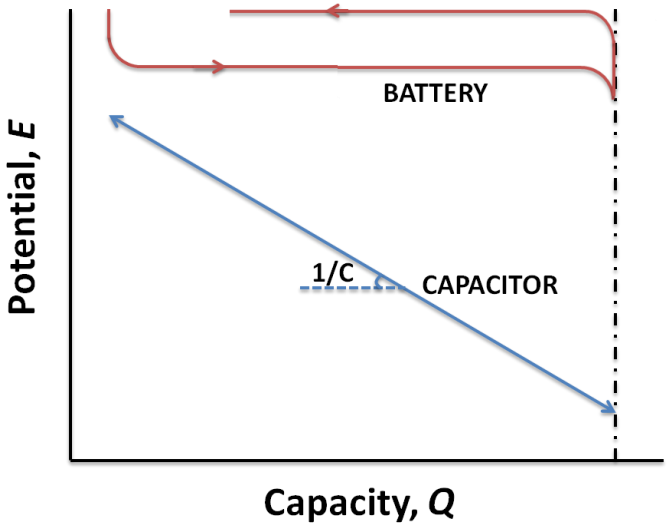

Figure 2.3. Comparison between the potential and capacity in an ideal battery and a capacitor. Adapted from Ref. 3.

First, it is apparent that assuming the same starting potential and total capacity, the maximum energy stored by a capacitor will be 1/2 that of the maximum energy stored by a battery. Secondly, while the reversibility of a capacitor is ideal, with the potentials upon charging and discharging remaining the same, this is not the case in a battery as will be explained in more detail later.

A Ragone plot comparison of capacitors, electrochemical capacitors, and batteries on a gravimetric basis is shown in Figure 2.4. The power and energy density differences between these devices stem from the mechanism of charge storage: bulk storage in batteries gives high energy densities but low power while surface storage in capacitors gives high power but low energy storage. The characteristic time response of the various devices is also indicated. Lithium-ion batteries typically store between 100-200 Wh kg^{-1} in hours while electrochemical capacitors store between 1-10 Wh kg^{-1} in less than 1 minute.

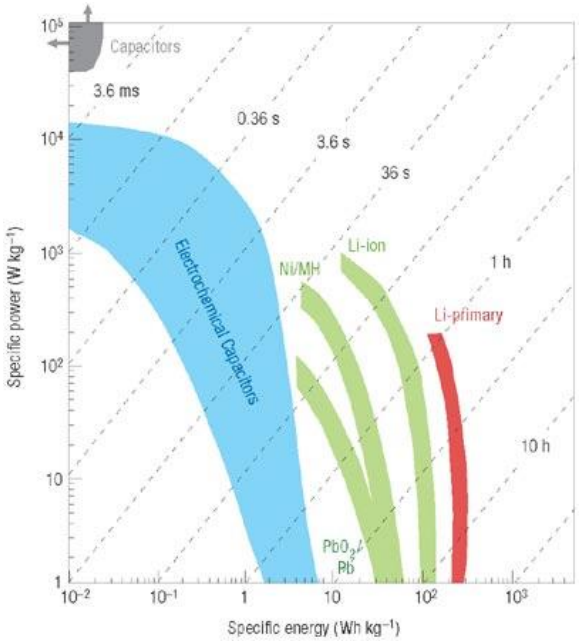

Figure 2.4. Ragone plot comparison of various energy storage technologies. Reproduced from Ref. 10.

2.2.2 Types of Electrochemical Capacitors

The discussion of capacitors in the previous section describes the thermodynamics of charge storage in a type of electrochemical capacitor called an electric double-layer capacitor (EDLC). However, as was first discovered in 1971 with RuO_2, there is another mechanism that gives rise to capacitive behavior and this is termed pseudocapacitance. Here, the charge storage is due to faradaic processes but the electrochemical response is like that of a capacitor. Figure 2.5 shows the different types of charge storage for double layer and pseudocapacitor types of electrochemical capacitors.

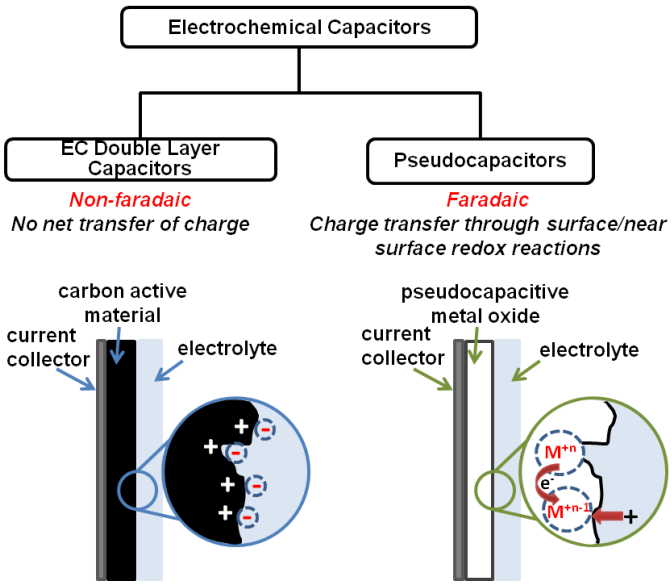

Figure 2.5. The different types of charge storage mechanisms in electrochemical capacitors. Reproduced from Ref. 11.

The electric double layer responsible for charge storage in an EDLC forms whenever an electrode material is inserted into an electrolyte solution. The basic structure of the electric double layer, based on the Grahame model, is shown in Figure 2.6. When the metal electrode is inserted into the electrolyte solution, the cations in the electrolyte move towards the metal surface at the same time as the free electrons in the metal move toward the surface. As shown in the figure, the electrode has an overall negative charge on its surface while there is an equal but opposite charge on the electrolyte solution side. On the metal/electrolyte interface, the first layer that forms is the Helmholtz Plane which consists of adsorbed anions and cations as well as neutral solvent molecules. The difference in solvation between cations and anions led to the distinction between an Inner and an Outer Helmholtz plane, the former corresponding to desolvated ions and the latter to ions that retain their solvation shell.[12] Beyond the tightly adsorbed Helmholtz Layer is the Guoy-Chapman diffuse layer that accounts for the thermal fluctuation of ions in a solution. The capacitance of the double layer then contains contributions

from the Helmholtz and the Guoy Chapman layers and is determined by the smaller of the two components.[3]

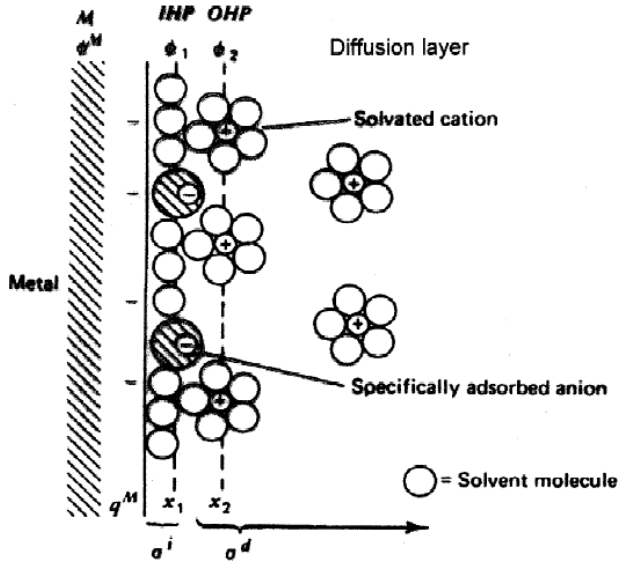

Figure 2.6. Schematic of the electric double layer at the surface of a metal immersed in an electrolyte, based on the Grahame model. IHP = inner Helmholtz plane, OHP = outer Helmholtz plane. Reproduced from Ref. 9.

From a physical standpoint, the electrostatic nature of the electric double layer formation at one electrode/electrolyte interface is directly analogous to a single dielectric capacitor. Equations 2.7-2.9, derived from dielectric capacitors, apply for the EDLC. However, unlike the dielectric capacitor, a single electrode/electrolyte interface cannot function as a device; it must be coupled with a second electrode. Therefore, the circuit diagram of an ideal EDLC consists of two capacitors (C_1 and C_2, corresponding to the capacitance of two electrodes) in series and the total cell capacitance (C_{tot}) contains contributions from both:

$$1/C_{tot} = 1/C_1 + 1/C_2 \qquad (2.10)$$

When an external potential is applied to the electrode, the size of the double layer increases in proportion to the induced charge on the electrode. The maximum capacitance

obtained through such a process is obtained from Eqn. 2.9 as for a dielectric capacitor, and a major research objective in the field of EDLCs is to understand the dependence of electrode area, including pore structure, on the capacitance.[13] Currently, the best carbon materials achieve double-layer capacitances of approximately 150 F g^{-1} for optimum carbon pore sizes in ionic liquid electrolytes.[10] Despite these advances in materials, commercial EDLCs store between 3-6 Wh kg^{-1},(Ref. 14) well below the theoretical energy densities of the electrode materials. This is mostly due to the fact that the nanostructured carbons under research result in volumetric and areal energy densities that are the same or lower than those of commercial devices.[15] While gravimetric capacitance values are useful for fundamental material characterization, when it comes to devices these values are no longer of great importance unless the capacitors are to be used in vehicular applications.

In some materials, there is an additional mechanism available for capacitive charge storage termed pseudocapacitance. This can occur when fast, reversible charge-transfer reactions take place at the interface between the electrolyte and the electrode. While the physical mechanism is no longer electrostatic, the electrochemical response is like that of the EDLC. There are many materials that exhibit pseudocapacitance: transition metal oxides[16] and nitrides,[17] conductive polymers,[18] oxygen and nitrogen functionalized carbons,[19] and molecular redox species in the electrolyte that adsorb onto an electrode surface.[20] By far, the most well-studied of these have been the transition metal oxides due to their stability, ease of synthesis, and variety of redox states.

2.3 Applications of Electrochemical Energy Storage

EES is used in a number of applications, and the type of device used (electrochemical capacitor *vs.* battery) is determined by the power and energy demands as well as cost. The main applications of EES are in portable electronics, transportation, and standby power.[21] Electrochemical capacitors and batteries fulfill different requirements and are sometimes paired

to fully meet the application demand, which is often more demanding than what a single EES device can provide. In general, batteries are used when portable power is necessary for periods of hours. Electrochemical capacitors are used for applications that require fast delivery or uptake of electrical energy. In terms of cost, aqueous-electrolyte based EES devices are always less expensive than ones that require non-aqueous electrolytes, which include lithium-ion devices and most EDLCs.

In portable electronics, the main use of EES is to provide electricity for the whole device. Historically, the majority of electronics were powered with alkaline Zn-MnO_2 ("Leclanché") batteries developed in the mid-19th century. However, as the energy demands of electronics increased this function was taken over by rechargeable batteries such as the aqueous electrolyte-based nickel-metal hydride batteries and lithium-ion batteries. Since their emergence in the early 1990s, Li-ion batteries have become the EES technology of choice for mobile phones and laptops. Electrochemical capacitors may be used in portable electronics for power demanding applications, such as the camera flash[22] or digital communication as in GPS.[23]

In the transportation sector, over 250 million rechargeable lead-acid batteries are manufactured every year for starting, lighting and ignition (SLI) of internal combustion engines.[21] There are other uses for EES in internal combustion vehicles that have been largely untapped. This includes catalytic converter pre-heating with electrochemical capacitors,[24] which could reduce hydrocarbon emissions of internal combustion engines by 60%. However, the major drive for research into EES devices has been to develop storage technologies for electric vehicles that can perform similarly to those powered by fossil fuels. By all accounts, this is an enormous challenge for EES due to the high energy content of hydrocarbons (> 10,000 Wh kg^{-1});[25] the best lithium-ion batteries today store 50x less energy. Nevertheless, the pursuit of higher energy density batteries is ongoing due to the importance of curbing carbon emissions and fossil fuel use.

Another major application for EES technologies is in standby power for use during emergencies, to provide electricity to crucial equipment and data until emergency generators start up or grid power returns. For example, EDLCs are used to provide power during emergencies to doors on the Airbus A380 jet airliner.[26] EES is well established for standby power applications, and the important EES properties include low self-discharge and long lifetimes. These can be fulfilled by EDLCs and where more energy storage is required, lead-acid batteries.[21] As this is a stationary application, high gravimetric energy densities are not as crucial.

Another emerging application of EES technology is in the power grid, where both electrochemical capacitors and batteries can play a role in lowering costs and improving reliability as well as reducing fossil fuel use in electricity generation.[27] Some renewable energy converters such as photovoltaics and windmills give intermittent electricity generation. In the case of photovoltaics, the peak demand time does not coincide with the peak generation.[28] Cost is one of the main obstacles for the adoption of EES technologies for this application as cheaper energy storage options are available.[27]

2.4 Nanomaterials for Electrochemical Energy Storage

Although there is no official definition of nanomaterial, the term is generally used to describe those materials where at least one of the dimensions is on the nanoscale, between 1-100 nm. When the size of a material becomes nanoscale, interesting new properties emerge due to quantum confinement effects as well as the increased number of surface atoms. Electrochemistry fundamentally involves interfaces between an electrolyte and electrode, and this interface increases by using the high surface area of a nanomaterial. In addition, the potentials at which a redox reaction occur are directly related to the change in Gibbs free energy of a substance, as described by Eqn. 2.6. In a nanomaterial, the surface adds an extra term to the Gibbs free energy of formation, called the Gibbs-Thomson effect:[29]

$$\Delta_f G^{\circ}_{nano} = \Delta_f G^{\circ}_{bulk} + 2\sum_j v_j \frac{\bar{\gamma}_j}{\bar{r}_j} V_j \quad (2.11)$$

here, v_j is the stoichiometric coefficient of the reaction, $\bar{\gamma}$ is the effective surface tension, $\bar{r}$ the effective radius, and V the molar volume. The result of the Gibbs-Thomson effect is that for a spherical particle of 1 nm diameter, the reaction potential increases by approximately 0.1 V from the bulk.[29] The advantages as well as disadvantages of utilizing nanomaterials for energy storage are summarized in Table 2.2.

Table 2.2. A comparison of the general advantages and disadvantages of utilizing nanomaterials for EES, adapted from Ref. 30.

Advantages	Disadvantages
▪ *Enable reactions that cannot occur in micron-sized particles* ▪ *Increase charge/discharge rates due to smaller diffusion distances* ▪ *Enhanced electron transport* ▪ *High contact area with electrolyte enabling high lithium flux* ▪ *Chemical potential for lithium ions may be modified leading to potential shifts* ▪ *Extended composition range for solid solutions* ▪ *Better strain accommodation*	▪ *Difficult to synthesize and control size or shape* ▪ *High contact area with electrolyte may lead to significant side reactions* ▪ *Lower volumetric energy density due to high porosity*

Chapter 3. Lithium-ion Batteries

3.1 Current State-of-the-Art

Lithium-ion batteries enabled the portable electronics revolution to take place over the past 20+ years. Today the batteries utilize reversible lithium-ion intercalation into both the cathode and anode to store energy. While electrochemical insertion of lithium into transition metal compounds was reported in the 1970s,[31] it wasn't until the discovery of lithiated transition metal oxides and lithium intercalation into graphite that the first battery was commercialized by Sony. The basic configuration of a lithium-ion battery is shown in Figure 3.1. The cathode material is usually $LiCoO_2$ while the anode is graphite. The advantage of utilizing these two electrode materials is that they result in a high cell voltage of 3.6 V and an energy density of approximately 120-150 Wh kg^{-1}.(Ref. 32) The electrolyte is $LiPF_6$ in a mixture of organic solvents such as ethylene carbonate and dimethyl carbonate. The reactions during the energy-storage (charging) stage are:

$$\text{Cathode: } LiCoO_2 \leftrightarrow Li_{1-x}CoO_2 + xLi^+ + xe^- \quad (3.1)$$

$$\text{Anode: } C_6 + Li^+ + e^- \leftrightarrow LiC_6 \quad (3.2)$$

These reactions are reversed during the discharge cycle; commercial lithium-ion batteries are rated for approximately 500 charge/discharge cycles.[21]

The high energy density of lithium-ion batteries comes from maximizing the voltage and capacities, as indicated by Eqn. 2.4. Both of these parameters are determined by the choice of anode and cathode materials, although the maximum voltage is limited by the potential window of the electrolyte. In the case of electrolytes based on $LiPF_6$ and liquid carbonates, the maximum voltage is limited to < 4 V for safety reasons. The voltage is maximized by utilizing a cathode with a high redox potential and an anode with a low redox potential; the difference between them gives the cell potential. The capacity is maximized by storing multiple lithium ions per formula unit, ideally with lightweight materials. The properties of the anode and

cathode materials currently utilized in lithium-ion batteries will be described in the next two sections.

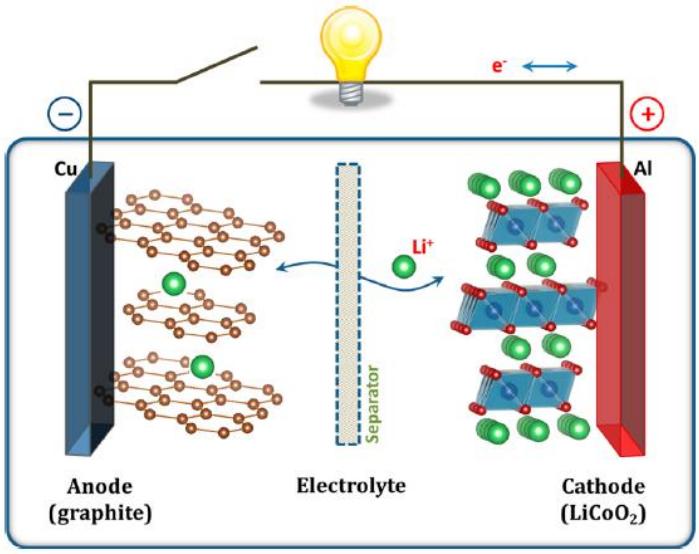

Figure 3.1. The configuration of a Li-ion battery used today. Reproduced from Ref. 33.

3.2 Cathode Materials

Commercially important cathode materials for Li^+ batteries include $LiCoO_2$, $LiMn_2O_4$, $LiNi_{1/3}Mn_{1/3}Co_{1/3}O_2$ ("NMC"), and $LiFePO_4$; the structure of these materials is shown in Figure 3.2.(Ref. 1) In all of these cases, a well-crystallized material is necessary for the intercalation reaction so the synthesis requires calcination temperatures between 600-800°C. $LiCoO_2$ and NMC both have a layered geometry consisting of transition metal-oxygen octahedra separated by a layer of lithium. In $LiCoO_2$, the redox reaction between $Co^{+3+/+4}$ occurs at a high voltage of 3.9 V *vs*. Li/Li^+. The practical capacity of 150 mAh g^{-1} is lower than the theoretical (270 mAh g^{-1}) due to the structural instability of removing more than 0.5 Li.[1] The advantage of the NMC material is that it uses less cobalt than $LiCoO_2$ while exhibiting a similar energy density. In this material, Mn is in the +4 state and electrochemically inactive and the charge storage occurs from redox reactions between $Ni^{+2/+4}$ and $Co^{+3/+4}$ valence states.[34] On the other hand, spinel

$LiMn_2O_4$ and olivine $LiFePO_4$ exhibit 3D framework structures that are more stable at high levels of delithiation and also utilize earth-abundant transition metals. However, their voltage (and in the case of $LiMn_2O_4$, capacity) are lower than $LiCoO_2$ so the energy densities of batteries built with these materials are lower. Significantly higher capacities of around 250 mAh g^{-1} are possible by utilizing families of materials based on $xLi_2MnO_3 \cdot (1-x)LiMn_{0.5}Ni_{0.5}O_2$ (Ref. 35) as well as $xLi_2MnO_3 \cdot (1-x)LiNi_{1.3}Mn_{1/3}Co_{1/3}O_2$ (Ref. 36). In both of these cases, high levels of lithium can be reversibly extracted from the structure due to the stabilizing effect of electrochemically inactive Li_2MnO_3. Currently, these materials still suffer from low power capability and the disproportionation of Mn^{3+} during discharge.[1]

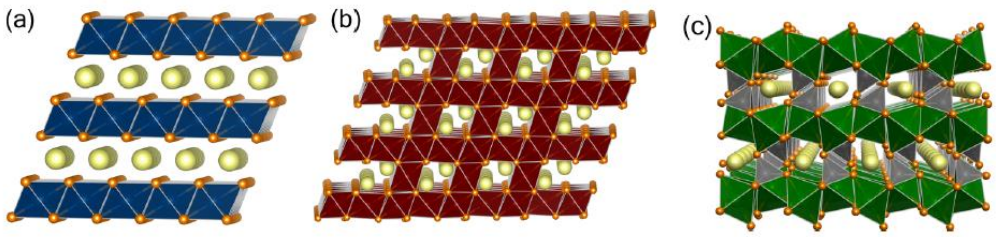

Figure 3.2. Structure of commercially used cathode materials for lithium-ion batteries: **a)** $LiCoO_2$, **b)** $LiMn_2O_4$, and **c)** $LiFePO_4$. Reproduced from Ref. 1.

In general, the issues plaguing cathode materials based on intercalation reactions stem from the structural and chemical instabilities that occur when a large amount of lithium is removed from the structure. The amount of lithium storage is limited to x =1 even for the highest-capacity materials. The high redox voltage required of a cathode material limits the transition metal elements available for the design of new materials to vanadium, manganese, iron, cobalt, and nickel; sustainability and toxicity concerns would limit that number further.[1] While a number of new cathode materials have been suggested such as the tavorite $LiFeSO_4F$, these also suffer from low power capability and storage of less than 1 Li per formula unit.[37]

3.3 Anode Materials

The energy density limitations plaguing cathode materials are not as severe for intercalation-based anode materials due to the ease of reducing a wide variety of materials at potentials just above the reduction potential of lithium. The most common anode material is graphite, which stores 1 lithium per C_6 at approximately 0.1 V for a theoretical capacity of 372 mAh g^{-1}.(Ref. 8) The structure of graphite before and after lithium insertion to LiC_6 is shown in Figure 3.3. LiC_6 is the final of the four lithiation stages of graphite and as a result of the intercalation the stacking order changes from "ABAB" to "AAAA". This corresponds to a phase change and so the lithiation of graphite exhibits plateaus corresponding to the different lithiation stages, as shown in Figure 3.4. Most of the charge storage occurs between 0.1 and 0.2 V, and at high rates lithium plating may occur which presents a serious safety issue. The capacity of graphite is more than 2X higher than that of $LiCoO_2$ so that in a cell the mass loading of the cathode is higher than that of the anode. Also, extra $LiCoO_2$ has to be added to allow for the irreversible solid-electrolyte interphase (SEI) formation on graphite during the first charging cycle.

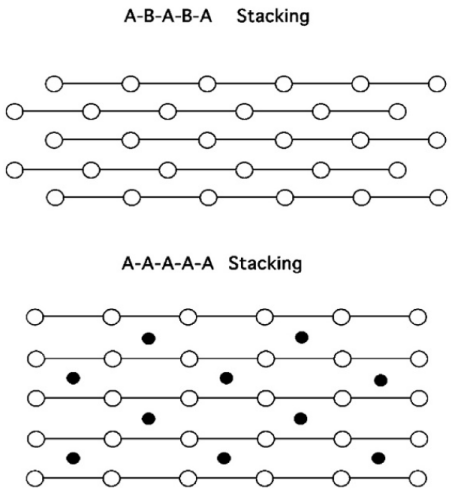

Figure 3.3. Stacking of graphite (top) and fully lithiated graphite, LiC_6 (bottom). Reproduced from Ref. 8.

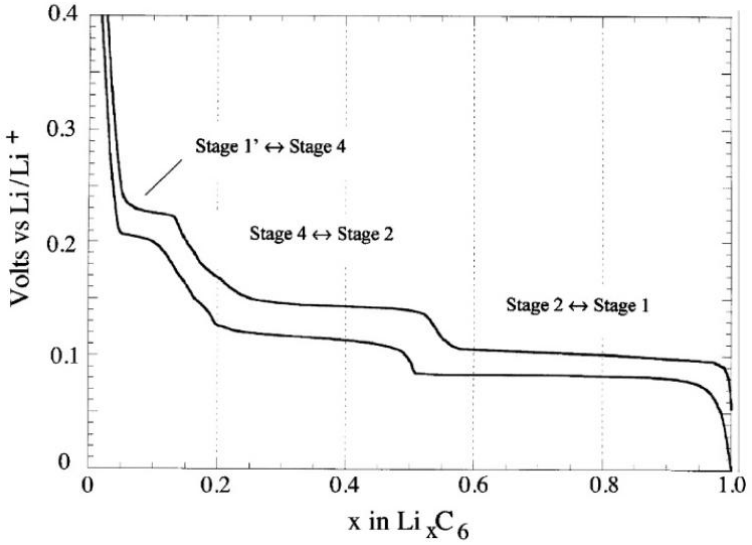

Figure 3.4. Lithiation and delithiation of graphite at a C/50 rate. Reproduced from Ref. 8.

3.4 Limitations of Intercalation Reactions

Intercalation reactions can offer a high degree of reversibility due to the small voltage differences during insertion and de-insertion for many materials. However, outside of their stability limits, intercalation materials experience severe structural changes and dissolution that lead to severe problems such as capacity fading and thermal runaway. As was discussed in the cathode section, intercalation reactions usually store 1 lithium per formula unit and this value has not increased over the years despite extensive research on the topic. Energy density can also be improved by increasing the voltage of the cathode material from the 3.6-3.9 V of $LiCoO_2$; the voltage of the graphite is already quite low. A number of higher voltage cathodes have been proposed, among them a family of materials based on the spinel $Li_yM_xMn_{2-x}O_4$, where M = Cr, Fe, Co, Ni and Cu.[38] In these materials, the energy storage occurs between 4 and 5 V. The higher voltage route has an additional challenge of finding suitable electrolytes for a 5 V potential window.

3.5 Conversion Reactions for High Energy Density Li-ion Batteries

Another method of increasing the energy densities of Li^+ batteries was proposed by Tarascon, *et al.* in 2000, based on the low-potential reactivity of certain transition metal oxides with lithium.[39] In this work, micrometer-sized *M*O (*M*=Co, Ni, Cu, Fe) with the rocksalt structure was found to react with lithium ions by reduction to nanometer-sized metal nanoparticles embedded in a Li_2O matrix:

$$MO + 2Li^+ + 2e^- \leftrightarrow M^0 + Li_2O \qquad (3.3)$$

The reversibility of the reaction was due to the *in situ* nanostructuring that occurred during the first lithiation cycle. The capacity for a conversion reaction is much larger than for an intercalation reaction due to the fact that more than 1 lithium is stored per formula unit. For CoO, the capacity is 700 mAh g^{-1}, more than 4X the practical capacity of $LiCoO_2$. However, for thermodynamic reasons, the voltage for conversion reactions of transition metal oxides is at or below 1 V. Conversion reactions have been reported in transition metal oxides, fluorides, sulfides, nitrides, hydrides, and phosphates.[40] The choice of anion dictates the conversion reaction potential as well as the hysteresis upon cycling, as described below.

This process is illustrated in Figure 3.5 for a material that has vacancies for lithium to intercalate. First, at relatively high potentials, the material will intercalate lithium based upon its allowed occupancy (Li-*M*-*X*, where *M* is the transition metal and *X* is the anion). Once the intercalation limit is reached, further lithiation occurs through a conversion process characterized by a voltage plateau. During this process, there is significant structural change from the initial material, which may be microns in size, into small (< 1 nm) metal nanoparticles and Li-*X*.[41] The number of lithium reacted depends on the oxidation state of the transition metal after the intercalation step. After this process, further charge storage occurs in a sloping region due to electrolyte decomposition or an interfacial storage mechanism. When the current is reversed, the plateau region is minimized due to the nanostructured nature of the product

formed after the first cycle. All of the lithium is not recovered because of SEI formation, which, due to the *in situ* nanostructuring, usually leads to large first-cycle irreversibility. On subsequent cycles, there is a significant hysteresis between the lithiation and delithiation cycles that partially depends on the anion: its value ranges from 0.4 V for Li*M*P_2 to 1.5 V for Li*M*F_2.

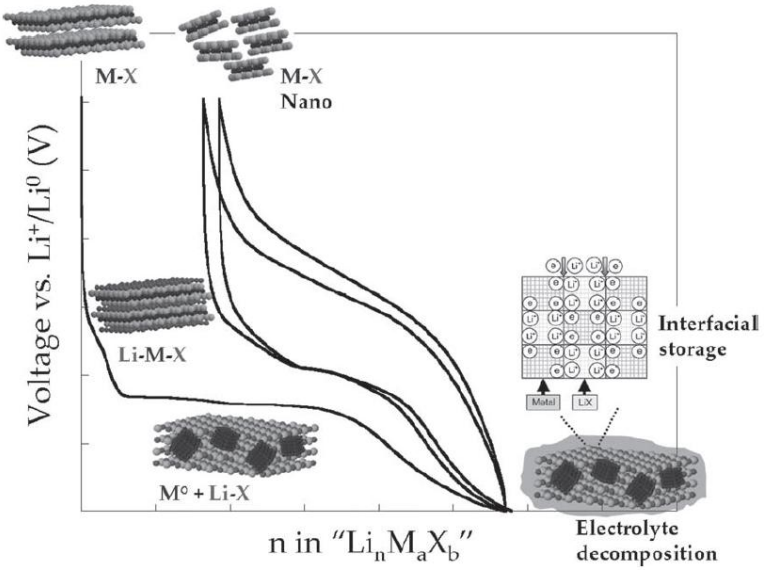

Figure 3.5. Charge-discharge of a layered transition metal compound, *M-X*, undergoing a conversion reaction with lithium. Reproduced from Ref. 40.

3.6 Voltage and Capacity of a Conversion Reaction

The capacity of a transition metal oxide undergoing a conversion reaction can be determined from the number of Li^+ necessary for a full reduction of the transition metal. The voltage of the reaction can be calculated from knowing the $\Delta G°$ values for the products and reactants. For a binary transition metal oxide undergoing a conversion reaction:[42]

$$M_xO_y + 2yLi^+ + 2ye^- \rightarrow xM° + yLi_2O \qquad (3.4)$$

the $\Delta G°$ for the reaction is calculated by subtracting the change in free energy of the products from the reactants and then converted into a cell potential using Eqn. 2.6. The calculated capacity and potentials for selected transition metal oxides are shown in Table 3.1.

Experimentally it has been found that for transition metal oxides, the actual cell potential is lower than the calculated cell potential by approximately 1 V. This difference is attributed to the overpotential necessary to overcome the activation barrier associated with the conversion reaction.[42] The 1 V overpotential means that conversion reactions would not occur for TiO_2, Cr_3O_4, and MnO, among others.

Table 3.1. Calculated average potential and capacity for a conversion reaction of selected transition metal oxides with lithium ions. Adapted from Ref. 43.

Metal Oxide	**Potential** (V *vs.* Li/Li^+)	**Capacity** (mAh g^{-1})
TiO_2	0.625	1342
V_2O_5	1.41	1474
Nb_2O_5	1.082	1008
Cr_2O_3	1.085	1058
MoO_3	1.75	1117
MnO_2	1.708	1233
Fe_2O_3	1.631	1007
RuO_2	2.12	806

3.7 Conversion Reaction Hysteresis

Figure 3.5 shows the galvanostatic profile for a general transition metal compound undergoing a conversion reaction. The hysteresis between the lithiation and delithiation stage is typically ~0.9 V for transition metal oxides.[30] This difference represents a very large energy inefficiency, one that occurs at all rates. The reason for the hysteresis is not clear, and it may vary from material to material; it has already been shown that the choice of anion changes its value.

Currently there is no consensus on the origin of the hysteresis but there are several possible theories. Results of density functional theory (DFT) calculations for the conversion

reaction of FeF_3 with lithium indicate that the reason for the voltage hysteresis in this material is due to the difference in mobility between iron and lithium cations; the iron cations are much slower.[44] This results in different reaction pathways for the lithiation and delithiation steps and therefore different reaction potentials. On the other hand, DFT calculations for the conversion of CoO with lithium point to asymmetry between various interfaces that form as a result of the conversion reaction as the cause of the hysteresis.[45] Pinpointing the cause of the hysteresis in conversion reactions is paramount if such materials are to be utilized in actual devices.

Chapter 4. Conversion Reactions in V_2O_5 Aerogels

4.1 Introduction

Vanadium oxide aerogels are unique materials that are able to intercalate reversibly a variety of ions leading to high gravimetric capacities,[46,47] making them useful for batteries and electrochemical capacitors.[48,49] Their energy storage properties can be attributed to a high surface area, three-dimensional mesoporous architecture which enables the electrolyte to penetrate the aerogel particles and access the redox-active, fibrous aerogel network. The specific capacity for lithium in vanadium oxide aerogels is greater than that of either the corresponding xerogel or crystalline V_2O_5.[46,50] The lithium capacity for these materials occurs from a reversible intercalation/de-intercalation reaction:

$$V_2O_5 + xLi^+ + xe^- \leftrightarrow Li_xV_2O_5 \qquad (4.1)$$

These intercalation reactions occur at potentials that are usually above ~ 1.5 V (*vs.* Li/Li^+).

In V_2O_5 xerogels, the structure consists of corner and edge shared VO_5 square pyramids that are separated by an interlayer gap;[51] the structure of the aerogel is probably similar to the xerogel, except the ribbon orientation is random. X-ray absorption experiments show that the local structure of the aerogel is similar to orthorhombic V_2O_5.(Ref. 52) The interlayer gap enables the lithium ion transport involved in the intercalation reactions.

It is well-accepted that the intercalation limit for inserting lithium-ions into orthorhombic V_2O_5 is the rocksalt ω-$Li_3V_2O_5$ phase formed below ~ 2 V.[53] The properties of V_2O_5 at lower potentials, especially < 1 V (*vs.* Li/Li^+), have received only limited study. Amorphous V_2O_5 films prepared by chemical vapor deposition exhibit high capacity (600 mAh g^{-1}) when cycled between 4 and 0 V.[54] V_2O_5 xerogels also have high capacity and exhibit the formation of Li_2O when cycled to potentials as low as 0.1 V.[55] Low potential studies with crystalline orthorhombic V_2O_5 show irreversible behavior when cycled to 0.02 V as the initial high capacity (675 mAh g^{-1}) fades completely within 40 cycles.[56]

The purpose of this study was to extend the study of low potential lithium-ion reactions to vanadium oxide aerogels at voltages < 1 V. Due to the multiple redox states of V_2O_5, the maximum capacity (assuming a 10-electron redox reaction) would be 1,472 mAh g^{-1} (Table 3). This is the first investigation of a metal oxide aerogel architecture being cycled down to 0.1 V *vs.* Li/Li^+, a potential regime usually restricted for conversion and decomposition reactions in metal oxides. Due to the high surface area and mesoporous architecture, vanadium oxide aerogels exhibit large reversible capacities for lithium as the aerogel morphology is very beneficial for lithium-ion reactions that involve significant structural changes.

4.2 Experimental Methods

Materials. Vanadium (V) triisopropoxide (96%) was purchased from Alfa Aesar. Acetone was purchased from Fisher Scientific. Vanadium (V) oxide (99.99%), lithium perchlorate (battery grade, 99.99%), ethylene carbonate (anhydrous, 99%), propylene carbonate (99%) and dimethyl carbonate (anhydrous, 99%) were purchased from Sigma-Aldrich. The chemicals were used with no further purification steps.

Synthesis and Electrode Preparation. The synthesis of vanadium oxide aerogels was published previously.[57] To make the gel, 0.4 mL of vanadium triisopropoxide, 2.4 mL of acetone, and 1.2 mL of deionized water were chilled in an ice bath for 1 hour. Then, the acetone and water were added to the vanadium triisopropoxide while agitating to mix the components. After about 30 seconds a red gel forms. The gel is aged for 7 days and then washed with acetone for 3 days. Next, the gel is transformed into an aerogel through supercritical drying with CO_2 at 40°C and 1,300 psi. Vanadium oxide aerogel electrodes were composed of 80 wt. % vanadium oxide aerogel, 15 wt. % carbon black (Ketjen Black, Akzo Nobel), and 5 wt. % polyvinylidene fluoride (Kynar Flex, Arkema) with a stainless-steel mesh serving as the current collector. Typical electrode loadings were between 0.8-1 mg cm^{-2}. Orthorhombic V_2O_5 electrodes were prepared in the same manner.

Characterization. Electrochemical measurements were carried out in an argon glovebox with moisture and oxygen levels of < 1 ppm. A BioLogic VMP3 Multichannel Workstation was used to make the galvanostatic and electrochemical impedance measurements. Three electrode experiments were performed in cells consisting of lithium foil reference and counter electrodes, a vanadium oxide aerogel working electrode, and 1 M $LiClO_4$ in ethylene carbonate/dimethyl carbonate (EC/DMC, 1:1 by volume) electrolyte. For 2-electrode experiments, custom-made stainless steel Swagelok cells[58] were assembled with a vanadium oxide aerogel cathode, a lithium foil anode, 1 M $LiClO_4$ in EC/DMC electrolyte, and a 260 μm-thick Whatman glass fiber filter that served as the separator. Room temperature electrochemical impedance measurements were made when the cells were on open circuit over a frequency range of 0.1 Hz to 100 kHz and a 10 mV (RMS) potential. For the samples prepared for the transmission electron microscopy (TEM) studies, a copper TEM grid served as the current collector. A diluted electrode slurry was deposited on the copper TEM grid which served as the working electrode in the electrochemical cells. After the cells reached the desired potential, the grids were rinsed with DMC and transferred under an inert atmosphere into the TEM with minimal ambient atmosphere exposure. TEM images were taken with the JEOL Jem1200-EX. X-ray photoelectron spectroscopy (XPS) measurements were taken with the Kratos AXIS Ultra using a monochromated Al X-ray source at 10 mA and 15 kV and a 20 eV pass energy. XPS of cycled aerogel electrodes was performed by rinsing the samples with DMC and loading them into an inert atmosphere transfer chamber, which was then connected directly to the XPS chamber. All XPS spectra were calibrated to the C 1s peak at 284.9 eV (Figure 4.1) and peak fitting was performed with the CasaXPS program using a 70:30 Gaussian-Lorentzian lineshape. X-ray diffraction (XRD) measurements were performed using the Panalytical X'Pert Pro X-ray Powder Diffractometer using Cu K_α radiation (λ=1.5425 Å).

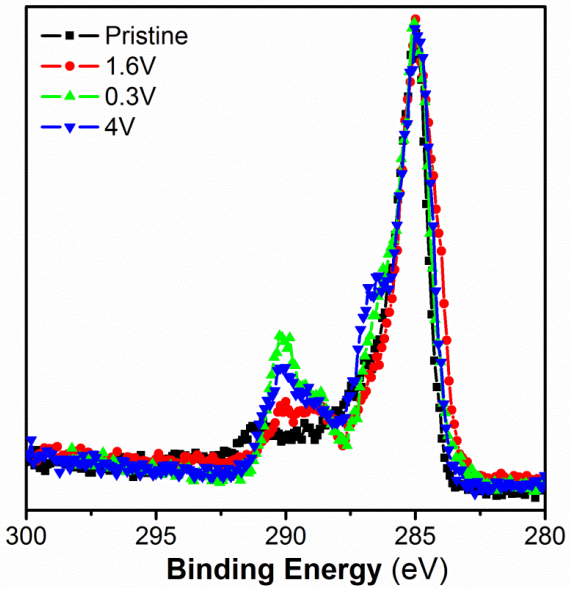

Figure 4.1. XPS of the C 1s region at different points in the lithiation cycle. The tallest peak corresponds to the presence of adventitious hydrocarbons on the surface and other species containing C-C and C-H bonds. This peak was used to calibrate the XPS spectra to 284.9 eV. The peaks at higher binding energies likely correspond to electrolyte degradation products, and their intensities are dependent upon potential.

4.3 Results & Discussion

The as-synthesized vanadium oxide aerogel morphology consists of fibrous ribbons that are approximately 10 nm wide, 1 nm thick, and 1 micrometer long; these structural features are retained after electrode processing (Figure 4.2a). The ribbons form a three-dimensional network structure; however, there is significant porosity between the ribbons. The XRD pattern for the aerogel gives several broad peaks, characteristic of a nanocrystalline material (Figure 4.3). These peaks are attributed to the internal ribbon structure of the aerogel material.[47,59]

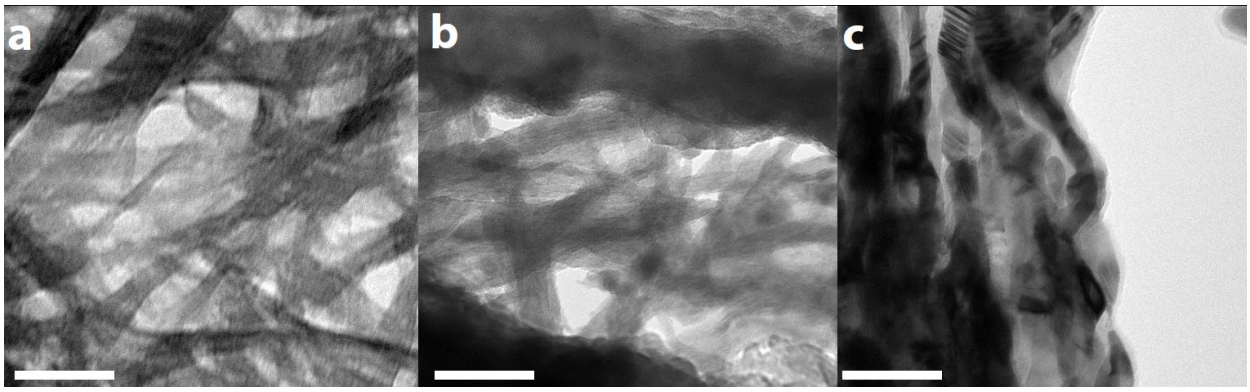

Figure 4.2. TEM images of the vanadium oxide aerogel electrode at various points in the lithiation process (obtained by cyclic voltammetry at 0.1 mV s^{-1}): **a)** pristine, **b)** at 1.8 V, and **c)** at 0.1 V. Scale bar = 50 nm.

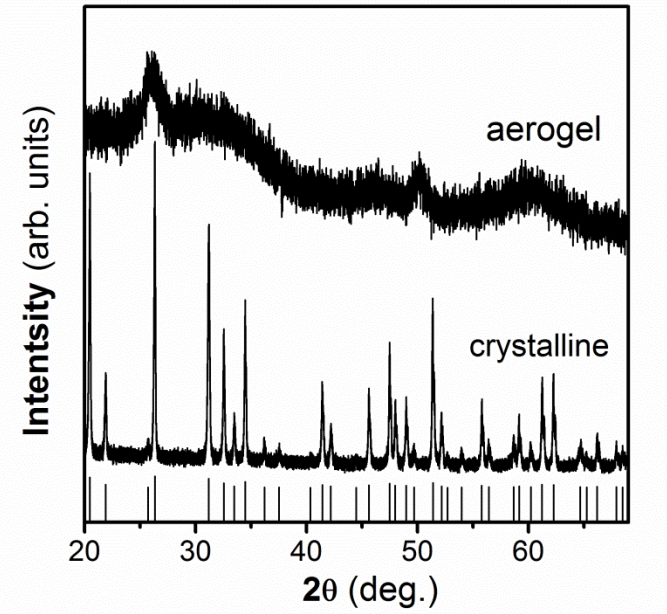

Figure 4.3. XRD patterns for aerogel and crystalline orthorhombic V_2O_5. The aerogel material contains short-range order and the major peaks correspond to the most intense peaks in the crystalline material. The XRD pattern for crystalline V_2O_5 corresponds well to shcherbinaite V_2O_5 (JCPDS #00-009-0387).

Galvanostatic cycling in a 2-electrode Swagelok cell was performed at various rates, from C/10 (118 mA g^{-1} or 0.09 mA cm^{-2}) to C/2 (590 mA g^{-1} or 0.47 mA cm^{-2}), where C = 1,178 mAh g^{-1} (based on an 8 e^- redox reaction with V_2O_5 due to the improbability of a full conversion to V^0, *vide infra*). The first and 50th cycles, both at a C/10 rate, are plotted in Figure 4.4a. In the first lithiation cycle, the shape of the curve is sloping, with a slight plateau around 2 V. At a potential of 1.5 V, the capacity is 330 mAh g^{-1}, or 2.24 Li^+/V_2O_5, comparable to previous results at this potential range.[46] With continued lithiation to 0.1 V, the capacity increases significantly. At approximately 1 V, a small plateau region emerges followed by a linear voltage decrease to 0.1 V. The capacity for the first lithiation is very high, approximately 1,400 mAh g^{-1}. Subsequent delithiation of the material to 4 V results in the removal of most of the lithium (840 mAh g^{-1}). The remaining lithium is likely used up in the formation of electrolyte degradation products, as has been found in many low-potential lithium-ion reactions.[40,60] By the fiftieth lithiation cycle, the plateau regions observed in the first cycle are minimized, and the capacity had stabilized to approximately 1,000 mAh g^{-1} or 6.8 Li^+/V_2O_5. Both lithiation and delithiation curves are less structured with only a few shoulders evident. On the fiftieth delithiation, the capacity retention is much better than during the first cycle, with a coulombic efficiency of 99.7%. The good capacity retention of the vanadium oxide aerogel electrode indicates that vanadium dissolution, which has been noted to occur below 1.5 V *vs.* Li/Li^+,[59] is not severe. The electrolyte degradation layer formed at low potentials (*vide infra*) could be acting as a protective layer, limiting further vanadium dissolution.

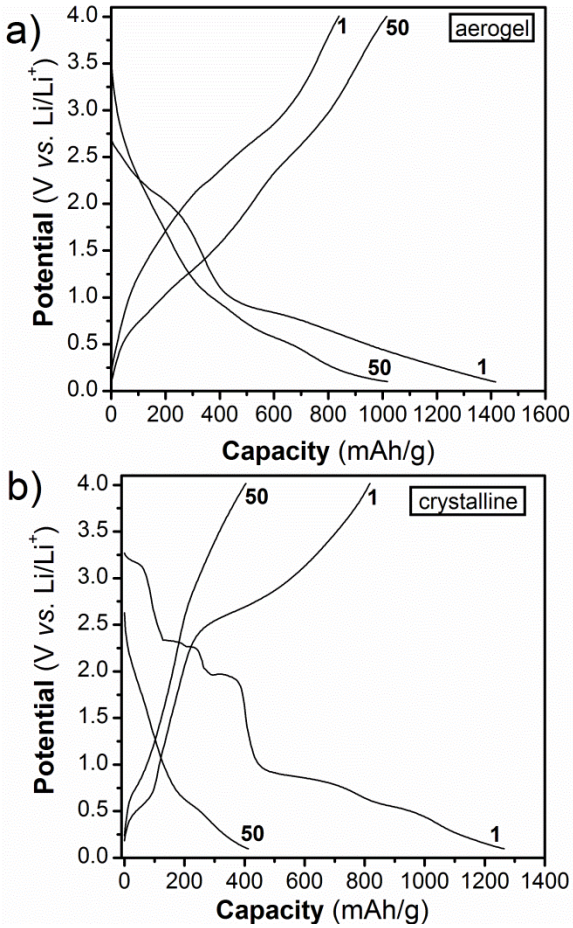

Figure 4.4. Galvanostatic charge/discharge curves between 0.1 and 4 V at a C/10 rate for the first and fiftieth cycles of **a)** a vanadium oxide aerogel electrode and **b)** a crystalline V_2O_5 electrode under the same experimental conditions.

Cycling the vanadium oxide aerogel electrode to low potential leads to remarkably high lithium capacity and retention. For comparison, we extended our studies to crystalline orthorhombic V_2O_5, whose crystallite size was estimated to be ~86 nm using the Scherrer formula (Figure 4.3). The first and fiftieth cycles of a crystalline V_2O_5 electrode are shown in Figure 4.4b. Up to 1.8 V, the lithiation of V_2O_5 proceeds through the formation of several well-known $Li_xV_2O_5$ phases.[53] By 1.5 V, the capacity is 400 mAh g^{-1}, corresponding to the storage of 2.7 Li/V_2O_5 and the formation of ω-$Li_3V_2O_5$. Continuing the lithiation to 0.1 V results in a discharge curve and capacity (approximately 1,200 mAh g^{-1}) that are similar to that of the

aerogel. During the delithiation cycle, 817 mAh g^{-1} is found to be reversible, and the featureless charging curve implies that the V_2O_5 is no longer crystalline. Upon continued cycling, the capacity decreases monotonically and after 50 cycles, the capacity of the material is ~400 mAh g^{-1}.

The rate capabilities for the aerogel and the crystalline electrodes are compared in Figure 4.5a. Both the aerogel and the crystalline electrodes exhibit a high initial discharge capacity. It is interesting to note that during the first few cycles at C/10 the capacity of the aerogel increases somewhat. The reason for the capacity improvement with cycling may be due to the reversible formation and dissolution of the polymer degradation layer.[61] Such capacity improvement was also observed in amorphous thin-film V_2O_5.(Ref. 54) The rate capability of the aerogel electrode is very good, with a capacity of ~700 mAh g^{-1} at a C/2 rate and full capacity recovery to ~ 1,000 mAh g^{-1} when cycled at C/10. In contrast to the stable behavior shown by the aerogel, the crystalline V_2O_5 electrode exhibits a continuous capacity decline with cycling. The capacity fading of orthorhombic V_2O_5 exhibited in the present study is not as severe as that reported previously by Poizot, *et al.*;[56] one reason for this could be that the present study utilizes a $LiClO_4$ electrolyte, and the lack of HF (a trace contaminant found in $LiPF_6$ electrolytes) may improve the stability of V_2O_5.(Ref. 62)

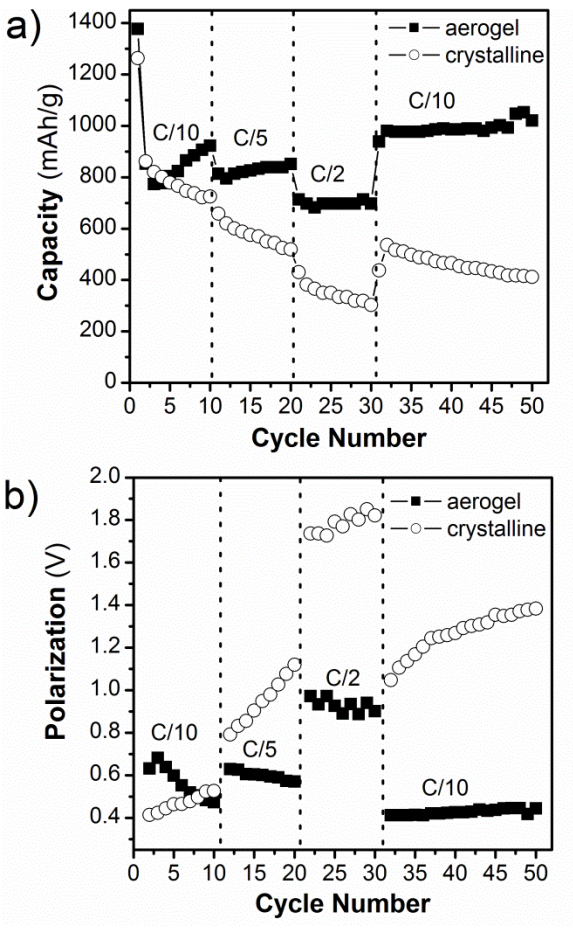

Figure 4.5. Comparison of a vanadium oxide aerogel electrode and a crystalline V_2O_5 electrode at **a)** various galvanostatic cycling rates and **b)** the polarization voltage during cycling.

The *iR* polarization voltage (voltage drop upon current application) as a function of cycle number is plotted in Figure 4.5b for both electrodes. The increase in polarization voltage of the crystalline electrode with cycling correlates well with the decrease in capacity. If the crystalline electrode is being structurally degraded, portions may become electrically disconnected, leading to higher polarization voltages. In contrast, the polarization voltage decreases after the second cycle in the aerogel electrode, and thereafter remains more or less stable. The decrease in the polarization voltage is accompanied by an increase in the capacity. Moreover, as shown in Figure 4.6, the impedance spectrum for the aerogel electrode cell remains fairly constant after

the first 10 cycles (C/10 rate). With the crystalline electrode, however, the observed increase in polarization voltage with cycling results in a continuous increase in impedance (Figure 4.7).

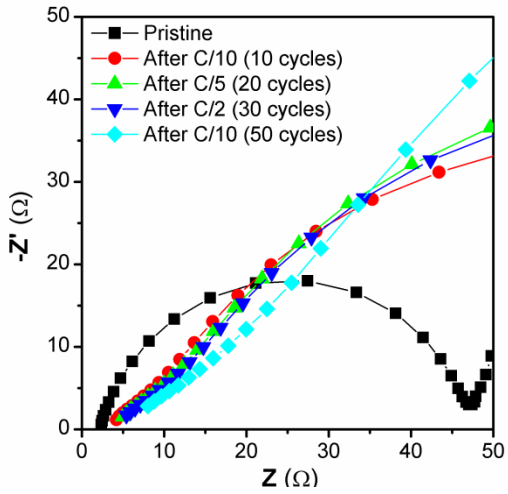

Figure 4.6. Electrochemical impedance of a vanadium oxide aerogel cell after galvanostatic cycling at various discharge rates. The measurements were taken at open circuit after charging (V ~ 4.0V). After the initial cycling at C/10, the impedance remains effectively unchanged.

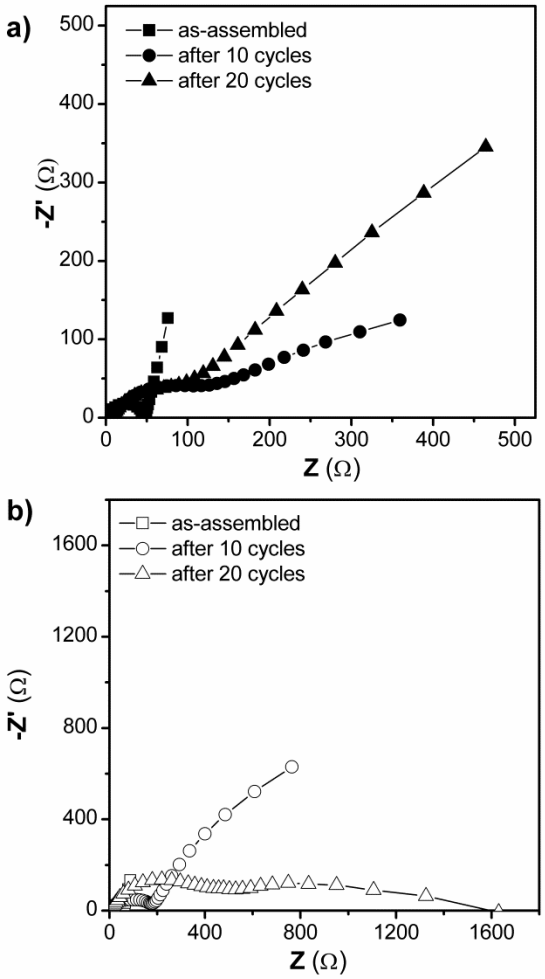

Figure 4.7. Comparison of electrochemical impedance before and after cycling for **a)** vanadium oxide aerogel and **b)** V_2O_5 crystalline cells. After 10 cycles, the crystalline cell exhibits higher impedance than the aerogel and after 20 cycles, the impedance of the crystalline cell increases significantly while that of the aerogel cell remains approximately the same. The measurements were taken at open circuit after charging (V ~ 4.0V).

The ability for the vanadium oxide aerogel to sustain high lithiation levels is significantly different from the crystalline orthorhombic material, a difference that is rooted primarily in the morphology of the redox-active material. After the first cycle to low potential, both the aerogel and the orthorhombic material exhibit relatively featureless charge-discharge curves which are characteristic of non-crystalline materials. The improved cycling behavior of the aerogel *vs*. the

crystalline electrode may be due to the fact that the aerogel structure is able to withstand the strain of reversibly storing a large amount of lithium. The storage of more than 6 Li^+/V_2O_5 should be accompanied by large volume changes. The low density (~0.1 g cm^{-3} for V_2O_5 aerogels)[57] of a porous aerogel results in a low Young's modulus,[63] which should allow the aerogel to flex. The advantage of a nanocrystalline architecture of the aerogel cannot be underestimated, as it has been found that MoO_3 nanocrystals cycled to 0.005 V exhibit significantly higher capacity retention than their bulk counterpart.[64] In that work the improved cycling is believed to be due to the stability of the nanocrystals during volume expansion. As indicated above, significant porosity in the aerogel electrode would enable reversible volume expansion.

In order to understand the structural and chemical changes that accompany the high capacity behavior, we performed *ex situ* TEM and XPS at various points in the discharge curve of the vanadium oxide aerogel electrode. The TEM results on lithiated vanadium oxide are shown in Figure 4.2b and c for electrodes discharged to 1.8 and 0.1 V, respectively. The electrochemical signal of the Cu TEM grid used as the current collector did not interfere with the electrochemical signal of the V_2O_5 aerogel (Figure 4.8). At 1.8 V, the morphology of the aerogel is similar to the electrode before lithiation (Figure 4.2a), with retention of the fiber morphology and porous network. Upon further lithium insertion to 0.1 V, there is a much larger change in the morphology. First, a thick layer of 5-10 nm seems to encompass the material, consistent with galvanostatic cycling results which indicate the formation of an electrolyte degradation layer due to the large irreversible first cycle capacity. Secondly, the nanoribbons are no longer seen clearly, although a rope-like structure appears to have formed. Finally, the porosity seen in the pristine and 1.8 V material is either entirely filled in with the film or has been decreased due to the morphology change. These TEM micrographs show that at low potentials the vanadium oxide aerogel undergoes a major morphological change that does not occur at higher potentials.

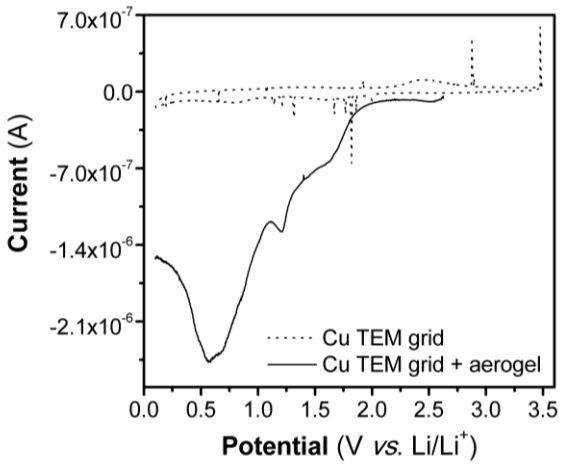

Figure 4.8. Cyclic voltammetry at 0.1 mV/s in 1 M $LiClO_4$ in EC/DMC of a copper TEM grid (Cu TEM grid) and a copper TEM grid onto which a dilute vanadium oxide aerogel electrode slurry was drop cast (Cu TEM grid + aerogel). In the experiment shown, the potential of the grid with the aerogel was limited to 0.1 V and this electrode was subsequently imaged by TEM as shown in Figure 4.2c.

In addition, it is interesting to compare the current work with recent results on conversion reactions with metal fluorides, where the presence of an electron transport network through metal nanocrystals allows for higher reversibility.[65] The rope-like structure observed at high lithiation levels in the vanadium oxide aerogel may lead to improved reversibility of the low potential reaction in the aerogel material *vs.* the crystalline structure, owing to a better electronic pathway for electrons in an electrode structure that is enveloped by insulating matrices such as the electrolyte degradation layer and, perhaps, Li_2O.

The oxidation state of vanadium at various points in the galvanostatic cycling process was investigated with XPS of the V 2p region (Figure 4.9). In the pristine electrode, the V 2 $p^{3/2}$ peak is centered at 517.8 eV, consistent with an oxidation state of +5. Peak fitting (Figure 4.10) further confirms the presence of V^{+5} along with a significant amount of V^{+4} (~ 49%), as a result of the synthesis conditions.[46] Upon lithium insertion to 1.6 V, the V 2 $p^{3/2}$ peak shifts to lower

binding energies, consistent with a change to a lower oxidation state for the vanadium. The peak maximum occurs at 516.3 eV, corresponding to the majority of vanadium existing in the V^{+4} state. Further discharging to 0.3 V shifts the peak to even lower binding energies, indicating that the reduction of vanadium is responsible for the additional capacity observed at the low potentials. At this voltage, the peak maximum occurs at 514.1 eV, corresponding to having the majority of vanadium in the V^{+2} state. Peak deconvolution at this voltage is difficult due to the low signal from the V 2p region, a result of the electrolyte degradation layer that forms on the surface. Upon lithium removal to 4 V, the peak shifts to higher binding energies, with a peak maximum at 517.5 eV, very close to the original peak maximum in the un-lithiated material. Interestingly, the peak width is considerably narrower, demonstrating that the cycled, delithiated material contains a larger percentage of V^{+5} than the pristine material. Also, at this voltage, the electrolyte degradation layer is diminished significantly and there were no problems with acquiring the V 2p signal.

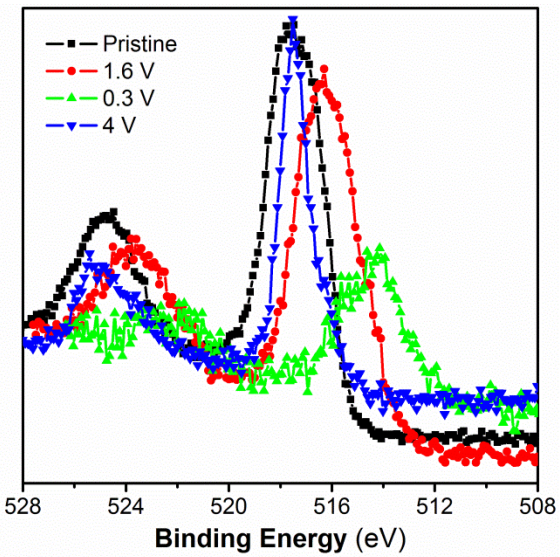

Figure 4.9. XPS of the V 2p peak at different points during lithiation/delithiation: pristine, after lithiating to 1.6 V, after lithiating to 0.3 V, and after delithiating to 4 V.

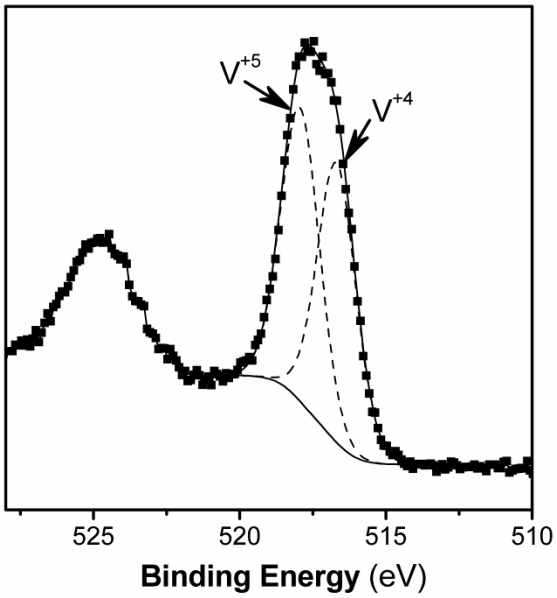

Figure 4.10. Peak fitting of the V 2p region in the pristine vanadium oxide aerogel electrode. The broad peak can be attributed to the presence of V^{+4}, which is due to the aerogel synthesis process.

Given the reversible high capacity of vanadium oxide aerogels when they are cycled to low potentials, the question remains as to how the lithium ions are stored. Reversible lithium-ion storage in metal oxides can be due to intercalation, decomposition, or conversion reactions, with more than one mechanism possible. The experimental data presented here demonstrates that up to 6.8 Li^+/V_2O_5 can be reversibly stored at the slowest rate examined (C/10), giving rise to a nominal vanadium oxidation state that is somewhat less than +2. From the XPS experiments, a vanadium oxidation state of +2 is observed and this changes back to the +5 state upon delithiation.

It is well-known that above ~ 1.5 V *vs.* Li/Li^+ the charge storage occurs through intercalation. Therefore, the reactant at lower potentials is $Li_xV_2O_5$. Given that the V_2O_5 is already lithiated, the thermodynamic data available for V_2O_5 and its suboxides are no longer useful; nevertheless it should be noted that the full conversion from V_2O_5 to V^o is calculated to

occur at an average voltage of 1.41 V, ending with the reaction of VO to V^0 at 0.85 V.[66] Previous results on binary metal oxides reacting with lithium indicate that, in general, a 1 V overpotential is necessary;[42] this would render the conversion to vanadium metal unlikely and indeed, the XPS results did not indicate that V^0 was present. A previous XPS study of chemical lithiation in amorphous V_2O_5 thin films indicated that for long lithiation times, the vanadium oxidation state changed to $V^{+2/+1}$ and was accompanied by the formation of Li_2O.[67] The presence of Li_2O was also reported in X-ray absorption studies of chemically lithiated V_2O_5 xerogels for compositions containing more than 1 Li^+/V_2O_5.(Ref. 55) The presence of Li_2O would indicate that a decomposition or conversion reaction has occurred. In the present study, *ex situ* XPS of the Li 1s region at 1.6 and 0.3 V gives a single broad peak at 54.8 eV that can be attributed to LiOH (Figure 4.11). The presence of LiOH is due to the reactivity of surface lithium with water molecules which are ubiquitously present in the environment. Previous research has shown that this peak cannot be used unambiguously to determine the presence of Li_2O.[68]

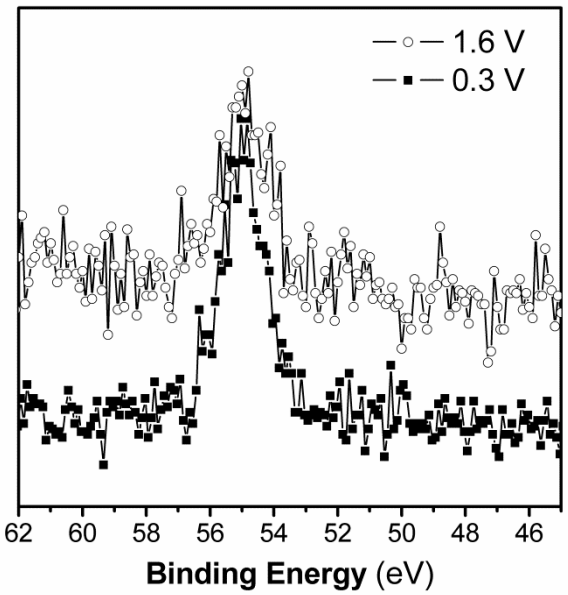

Figure 4.11. XPS of the Li 1s region of vanadium oxide aerogel electrodes after lithiation to 1.6 and 0.3 V. In both cases, the peak maximum occurs at 54.8 eV, indicating the presence of LiOH.

First-principles calculations of the layered transition metal oxides of composition LiMO$_2$, where M is Mn, Co, Ni, or Mn, have found that for an additional storage of 1 mol of Li, conversion reactions are always energetically favorable as compared to intercalation or decomposition.[69] Experimentally both $LiCoO_2$ and $LiNiO_2$ follow a reaction pathway of intercalation followed by an irreversible decomposition to a monoxide.[70] Once the formation of a monoxide occurs, the conversion reaction is favored, as the monoxides of the 3d transition metal oxides exist in the rocksalt structure.

Given these results, the high capacity of vanadium oxide aerogels is expected to involve a two-step process of intercalation followed by decomposition:

$$V_2O_5 + xLi^+ + xe^- \rightarrow Li_xV_2O_5 \quad (4.2)$$

$$Li_xV_2O_5 + 2Li^+ + 2e^- \leftrightarrow V_2O_3 + Li_2O \quad (4.3)$$

$$V_2O_3 + 2Li^+ + 2e^- \leftrightarrow VO + Li_2O \quad (4.4)$$

The formation of VO at the end of the discharge step would explain the +2 oxidation state observed in the XPS results. Moreover, the porous architecture of the vanadium oxide aerogel can readily accommodate a high volume of intercalated lithium along with the Li_2O phase that forms.

4.4 Conclusions

Vanadium oxide aerogels exhibit a reversible capacity of > 1,000 mAh g^{-1} when cycled to 0.1 V in a lithium-ion electrolyte. The behavior is attributed to the aerogel morphology, as the reversibility is significantly better than that of crystalline orthorhombic V_2O_5. The vanadium oxide aerogel possesses several attributes that have been previously found beneficial for reactions that involve the storage of significant amounts of lithium: high surface area, interconnected porosity and a fibrous morphology. *Ex situ* TEM data indicates that the fibrous morphology of the aerogel is retained even after cycling to low potentials, and the oxidation state

of vanadium at 0.3 V is +2, indicating that charge storage occurs due to the reduction of vanadium from +5 to +2. These results demonstrate that aerogels are able to sustain deep electrochemical lithiation levels when cycled to low potentials. The mechanism of charge storage is expected to involve a two-step process of lithium intercalation followed by decomposition reactions. The ability to access lower oxidation states of vanadium in the vanadium oxide aerogel results in an electrode material that can be used over essentially the entire lithium-ion voltage range as either a cathode or an anode in charge storage devices.

Chapter 5. Pseudocapacitance

5.1 Thermodynamic Understanding of Pseudocapacitance

The origin of pseudocapacitance was described thoroughly by Conway.[3] In this description, pseudocapacitance occurs whenever the amount of charge storage (ΔQ) depends on the change in potential (ΔV), giving the form of a capacitance ($\Delta Q/\Delta V$). This contrasts to the constant potential process associated with battery materials. There are three pseudocapacitive processes that can occur when a redox-active material is immersed in electrolyte (Figure 5.1). (a) Metal ions form a monolayer at a metal surface well above the redox potential of the metal in a mechanism termed underpotential deposition. (b) Ions are electrochemically adsorbed onto the surface of the material. In this mechanism, referred to as redox pseudocapacitance, adsorption is associated with a change in the valence change in the material. (c) Ions intercalate into the tunnels or layers of a redox-active material accompanied by a valence change of the material. This third process is referred to as intercalation pseudocapacitance.

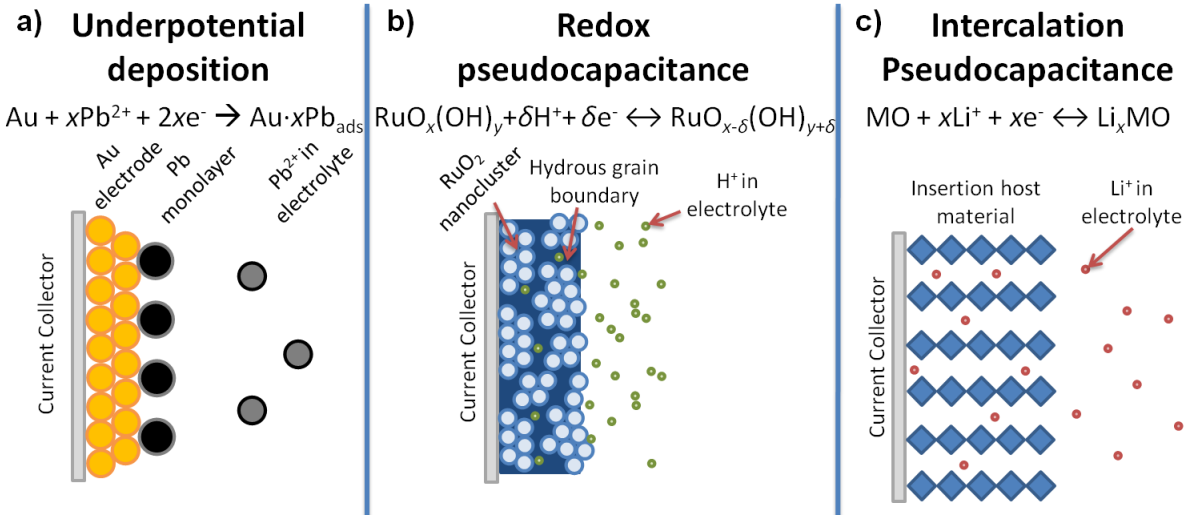

Figure 5.1. Different types of reversible redox mechanisms that give rise to pseudocapacitance: **a)** underpotential deposition, **b)** redox pseudocapacitance, and **c)** intercalation pseudocapacitance.

For all three pseudocapacitive mechanisms, the extent of charge storage and potential are related. The mechanisms can be thought of as adsorption processes that follow a Langmuir-type isotherm:

$$\left(\frac{X}{1-X}\right) = Kexp\left(\frac{E\mathrm{F}}{\mathrm{RT}}\right) \tag{5.1}$$

where X is the extent of fractional coverage of the surface or interior structure, K is the reaction equilibrium constant, E is the potential, F is the Faraday's constant, R is the ideal gas constant, and T is the temperature. Taking the natural log of both sides gives the principal relationship between potential and extent of charge storage:

$$E \sim \frac{RT}{F} ln\left(\frac{X}{1-X}\right) \tag{5.2}$$

5.2 Types of Pseudocapacitance

Underpotential deposition is illustrated in Figure 5.1a. In this example, lead ions in the electrolyte adsorb/desorb onto the surface of a gold electrode. The cyclic voltammogram (CV) for this reversible process is shown in Figure 5.2. The main feature of this CV is that it is symmetric for the cathodic and anodic sweeps, with no peak offset even at 50 mV s^{-1}. The fractional coverage of the surface, θ, *vs*. potential is the bottom plot of Figure 5.2. It is clear that θ depends upon the potential although the relationship is not perfectly linear as for an ideal capacitor. If the potential was decreased beyond the redox potential for lead (-0.13 V *vs*. SHE), eventually lead ions would deposit on top of lead ions for the electrodeposition of lead resulting in an asymmetric CV with a large offset between the deposition and stripping peak currents. While the underpotential deposition process is kinetically facile due to its high reversibility, the potential window is too small for applications, *ca*. 200 mV in the case of lead.[71]

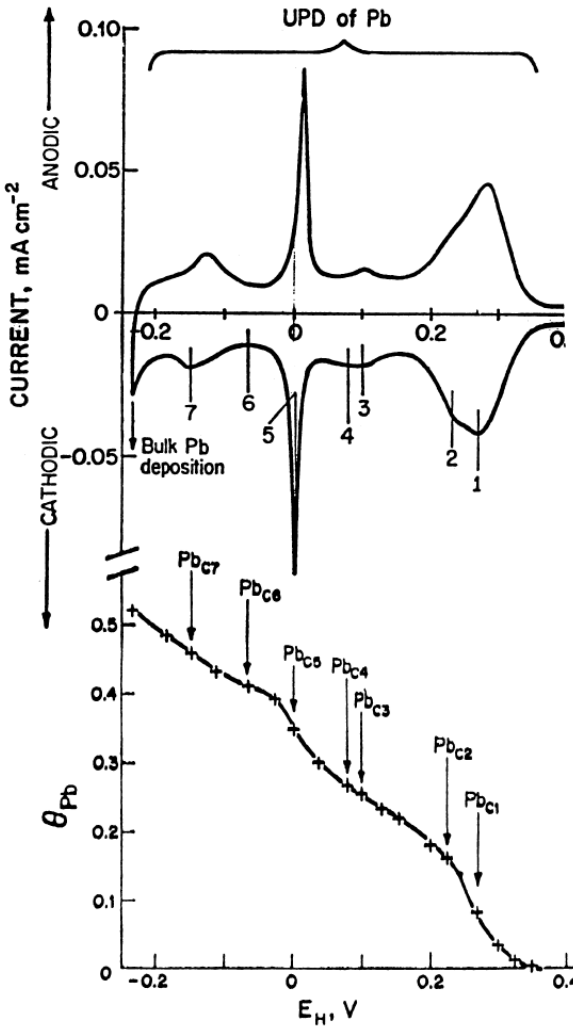

Figure 5.2. Underpotential deposition of lead ions onto gold. **Top**: Cyclic voltammetry at 50 mV s^{-1} in aqueous $HClO_4$ electrolyte. **Bottom**: Integration of the cathodic sweep as a function of potential. Reproduced from Ref. 71.

Redox pseudocapacitance occurs with transition metal oxides, conductive polymers, and surface-functionalized carbons. This type of capacitance occurs over a wider potential window than underpotential deposition and is therefore relevant for device applications. It is illustrated in Figure 5.1b for the case of hydrous RuO_2, one of the best and also first identified redox pseudocapacitive materials. RuO_2 is a metallic conductor, one of the few metal oxides that exhibits this property along with a high oxidation state. Its single crystal electronic conductivity

is on the order of 10^4 S cm^{-1}.(Ref. 72) The theoretical capacitance for the storage of 2 H^+ per RuO_2 over a 1.4 V window is ~1000 F g^{-1}. In Figure 5.3, the CV of RuO_2 in sulfuric acid demonstrates its almost constant current response as a function of potential, as would be expected for a capacitor.

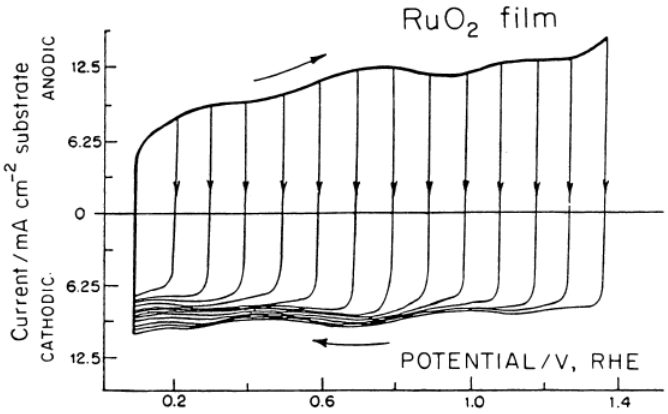

Figure 5.3. Cyclic voltammetry of RuO_2 in 0.1 M H_2SO_4 at 50 mV s^{-1}. The CV was performed by cycling between different potentials from 0.1 to 1.3 V to demonstrate the reversibility of the pseudocapacitive process. Reproduced from Ref. 71.

The redox mechanism in this material is believed to involve nanodimensional hydrous grain boundaries that serve as proton-conducting channels while the electron transport occurs through nanocrystalline RuO_2 particles.[73] The redox reaction and storage take place within the first few layers of the surface.[74] As a result of this mixed conduction mechanism, the highest capacitance values occur for $RuO_2 \cdot xH_2O$ where x = 0.5.(Ref. 75) Despite its excellent electrochemical properties, the high price of RuO_2 (~$2742 per kg *vs.* $774 per kg of silver, as of May 2013), makes it practical only for niche applications. Since its discovery in 1971, RuO_2 has been the "gold standard" of pseudocapacitive materials and much research has focused on identifying materials similar to RuO_2, with limited success.

The third pseudocapacitive mechanism is intercalation pseudocapacitance. In materials that undergo intercalation without a concomitant phase change, the Gibbs phase rule (Eqn. 2.3) dictates that the extent of charge storage will vary with composition. This gives rise to a capacitance as in the previous two cases. For practical purposes, however, intercalation pseudocapacitance has not been considered because it is usually limited by solid state diffusion and does not exhibit the kinetic signatures of capacitance, as described in the next section.

5.3 Kinetic Features of Pseudocapacitance

Pseudocapacitance offers the promise of high-rate EES and while the thermodynamic (potential-dependent) behavior can identify pseudocapacitive systems, the usefulness of the material is identified by the kinetic behavior. The kinetics of electrochemical processes are fundamentally related to their current, and can be evaluated by using various transient electrochemical techniques. Cyclic voltammetry is a powerful technique that allows for the systemic variation of time and easy determination of peak potentials and currents. In the next few chapters, analysis techniques based on cyclic voltammetry will be utilized to separate surface (capacitive) from diffusion (battery-like) contributions to charge storage. The fundamental relationships between current and cyclic voltammetry sweep rate are described below.

The current density at the peak potential of a redox reaction (such as the one described by Eqn. 2.2) as a function of the sweep rate is given by the Randles-Sevcik equation as:

$$i_{\mathrm{p}} = 0.4463 n\mathrm{F} A C_{\mathrm{O}} D_{\mathrm{O}}^{1/2} \left(\frac{n\mathrm{F}}{\mathrm{R}T}\right)^{1/2} v^{1/2} \qquad (5.3)$$

Here, i_{p} is the peak current, n is the number of electrons transferred in Eqn. 2.2, F is the Faraday's constant, A is the electrode area, C_{O} is the concentration of species O, $D_{\mathrm{O}}^{1/2}$ is the diffusion coefficient of species O, R is the ideal gas constant, T is the temperature, and v is the sweep rate of the cyclic voltammetry experiment. This equation is derived by solving for Fick's

2nd law of diffusion and utilizing appropriate boundary conditions for semi-infinite diffusion. That is, this equation applies in situations where the reaction is limited by diffusion in the electrolyte or the electrode.

In cases where no diffusion limitations are observed, such as simple surface adsorption, the relationship between current and sweep rate is:

$$i = Cv \tag{5.4}$$

This type of response is usually associated with the surface adsorption processes of double-layer capacitors, and termed "capacitive current." By comparing Eqns. 5.3 and 5.4, it is evident that the capacitive current will increase faster with v than the diffusion-controlled current.

Chapter 6. Pseudocapacitive Behavior in *T*-Nb_2O_5

6.1 Introduction

The electrochemical behavior of Nb_2O_5 was first investigated by Bard *et al.*,[76,77] who demonstrated that Nb_2O_5 exhibits lithium and proton insertion and is also electrochromic. These studies led to further research of Nb_2O_5 as a lithium-ion battery electrode and as an electrochromic window. Lithium insertion into Nb_2O_5 occurs below 2 V (*vs.* Li/Li^+) and the material has been incorporated in 2 V lithium-ion secondary batteries that employ a lithium alloy as the negative electrode.[78] The reversibility of the lithium intercalation process is well established; the amount of lithium insertion in $Li_xNb_2O_5$ varies between x = 1.6 to 2, for a maximum capacity of 728 C g^{-1} or ~ 200 mAh g^{-1}. In the electrochromics field, kinetics played a larger role since fast coloration times are needed and Nb_2O_5 films can color in as fast as 10 seconds.[79] This kinetic response, along with a large difference between the colored and bleached state, renders Nb_2O_5 as one of the best inorganic electrochromic materials.[79]

The prior research does not indicate whether one particular phase of Nb_2O_5 is better than another; the application area seems to determine the desired Nb_2O_5 phase. Thus, the pseudohexagonal phase of Nb_2O_5 is preferred for electrochromic devices[79] while the tetragonal phase seems to lead to the best battery electrodes.[78] In general, the basic question of how crystal structure and phase influence capacitive storage is only beginning to be considered. The work reported by Favier *et al.*[80] on MnO_2 polytypes demonstrated that the crystallographic structure has a significant influence on the capacitive storage behavior of the material. In particular, three-dimensional MnO_2 spinels exhibited greater specific capacitance than MnO_2 phases with either 2D or 1D structures.

In this chapter, the effects of phase and crystallinity on the fundamental charge storage properties of Nb_2O_5 nanoparticles are examined. For the most part, the capacitive storage properties of Nb_2O_5 have not been investigated. What is particularly attractive for this system is that the linear dependence of peak current on sweep rate for mesoporous Nb_2O_5 suggests that

this material possesses much better charge storage kinetics than other transition metal oxides.[81] In the current study, different phases of Nb_2O_5 nanoparticles were synthesized through sol gel routes and the electrochemical properties were determined using electrodes composed only of nanoparticle powders, *i.e.*, with no binders or conductive additives to complicate the measured response. Electrochemical studies show that orthorhombic Nb_2O_5 exhibits high specific capacitance at high rates, with nearly 400 F g^{-1} being stored reversibly within 12 seconds. These values are comparable to what has been reported for RuO_2. In addition, the crystal phase of the Nb_2O_5 nanoparticles and the size of the ion are identified as being significant factors in the charge storage process.

6.2 Methods

Synthesis. Both amorphous and *T*-Nb_2O_5 were synthesized using an aqueous sol-gel technique. Anhydrous $NbCl_5$ (2.56 mmol) was dissolved in ethanol (2 mL) while a solution of DI water (0.23 mL) in ethanol (2 mL) was prepared in a separate vial. Both solutions were cooled in an ice bath for 2 hours in order to prevent uncontrolled hydrolysis and condensation which leads to precipitate rather than gel formation. The two solutions were then mixed together while propylene oxide (~1 mL) was slowly injected until a transparent gel formed. The Nb_2O_5 wet-gel was aged for 1 day to promote network formation, immersed in acetone, which was replaced periodically for 5 days before the gel was supercritically dried using CO_2.(Ref. 57) The resulting amorphous Nb_2O_5 aerogel was calcined at 400°C in air for 2 hours to remove any remaining adsorbed water and organics. This treatment did not crystallize the material (Figure 6.1a). To produce the *T*-Nb_2O_5 phase the amorphous aerogel was annealed at 600°C for 2 hrs in air.

Material Characterization. The phase of each Nb_2O_5 sample was identified using a powder X-ray diffractometer (PANalytical X'PertPro) using Cu Kα (λ=1.54 Å) radiation. Brunauer-Emmett-Teller (BET) surface areas were obtained from nitrogen adsorption isotherms at 77 K using a gas adsorption analyzer (Micromeritics ASAP 2010). The particle size and crystalline

nature of Nb_2O_5 were further characterized by transmission electron microscopy (TEM; CM 120, FEI) and high resolution transmission electron microscopy (HR-TEM; TITAN S/TEM, FEI).

Electrochemical characterization. Electrochemical measurements were performed in a three-electrode cell with a nanoparticle film of Nb_2O_5 serving as the working electrode. To prepare the working electrode, nanoscale sized powders of Nb_2O_5 aerogel or the crystallline phase (~ 20 μg) were cast from an ethanol solution onto an oxygen-plasma treated stainless steel foil (~ 1 cm^2 area), which was subsequently heated at 110°C for one hour to evaporate the ethanol. The mass of the nanoparticles deposited on the stainless steel foil was determined using a microbalance. The electrolytes used were 1 M $LiClO_4$ or $NaClO_4$ in propylene carbonate (PC). Lithium or sodium metal foils were used as the counter and reference electrodes. Cyclic voltammetry was performed between 1.2 and 3 V *vs.* Li/Li^+ (or Na/Na^+) using a PAR EG&G 273A potentiostat. All tests were performed in an argon glovebox with oxygen and water levels of < 1 ppm. For the *ex-situ* HR-TEM experiment, *T*-Nb_2O_5 particles were deposited directly on a copper TEM grid which served as the working electrode. After the electrochemical measurements, the sample could be placed directly into the TEM.

6.3 Material Characterization

Nb_2O_5 has a variety of polymorphs which can be obtained mainly through thermal treatment.[82] The phases of Nb_2O_5 examined here are amorphous and orthorhombic (*T*-Nb_2O_5). These were synthesized by heat treatment of a niobium oxide aerogel precursor prepared by an aqueous sol-gel route.

The phase and morphology of the Nb_2O_5 materials were characterized using XRD and TEM. XRD patterns for each of the Nb_2O_5 phases synthesized are shown in Figure 6.1. As-synthesized Nb_2O_5 aerogel is amorphous (not shown) and has a BET surface area of 442 $m^2\ g^{-1}$. After calcination at 400°C to dehydrate the structure, the Nb_2O_5 is still amorphous (Figure 6.1a) but the BET surface area is reduced to 187 $m^2\ g^{-1}$. Heating as-synthesized Nb_2O_5 aerogel to

600°C in air leads to *T*-Nb_2O_5, as shown in Figure 6.1b. The *T*-phase material has a surface area of 70 m^2 g^{-1} and an average particle size of 35 nm. TEM images of the Nb_2O_5 particles synthesized in this work show the different sizes and morphologies for the various phases (Figure 6.2). The orthorhombic nature of *T*-Nb_2O_5 was further confirmed using HR-TEM. The lattice parameter (3.157Å) in Figure 6.4a corresponds to the (180) plane of *T*-Nb_2O_5.

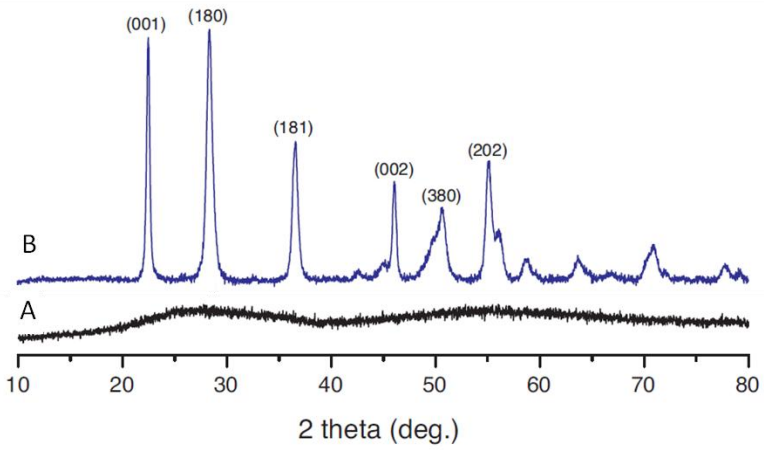

Figure 6.1. XRD patterns for **a)** dehydrated amorphous Nb_2O_5 aerogel and **b)** orthorhombic *T*-Nb_2O_5. The *T*-phase indexes to JCPDS card #30-873.

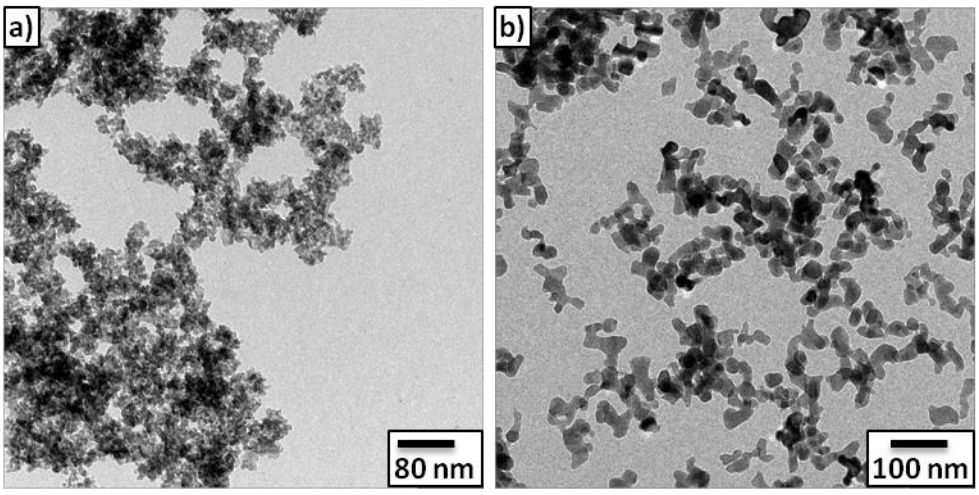

Figure 6.2. TEM images for **a)** dehydrated Nb_2O_5 aerogel and **b)** orthorhombic *T*-Nb_2O_5.

6.4 Electrochemical Behavior

The charge storage properties were investigated in 3-electrode cells using lithium (or sodium) as the counter and reference electrodes. Cyclic voltammetry with lithium and sodium-ion electrolytes (1 M $LiClO_4$ or $NaClO_4$ in PC) was used to determine the electrochemical properties of the Nb_2O_5 nanoparticles. For Nb_2O_5 in a lithium ion electrolyte, charge storage occurs through the insertion of lithium ions with concomitant reduction of Nb^{+5} to Nb^{+4}, for a maximum theoretical storage of $x = 2$ (or 726 C g^{-1}):[83]

$$Nb_2O_5 + xLi^+ + xe^- \rightarrow Li_xNb_2O_5 \qquad (6.1)$$

In order to investigate the capacitive properties of Nb_2O_5, sweep rates were varied from 5 to 100 mV s^{-1}. For a typical range of 1.2 V, these conditions corresponded to a charge/discharge time between 12 seconds and 4 minutes.

The crystalline phase of Nb_2O_5 exhibits a much greater level of charge storage compared to the amorphous material. The CVs in Figure 6.3a show that for the crystalline material, the current response increases dramatically below 2.2 V *vs*. Li/Li^+, giving rise to several broad cathodic peaks around 1.75 V and 1.5 V. During lithiation, the electrode exhibits blue coloration, demonstrating the well-known electrochromic property of crystalline Nb_2O_5.(Ref. 84) On sweep reversal, identification of anodic peaks for the Nb_2O_5 is more difficult, with two very broad peaks apparent at about 1.5 V and 1.8 V for *T*-Nb_2O_5. Based on the small difference between insertion and deinsertion peak voltages, the lithiation process is highly reversible in crystalline Nb_2O_5. The scans shown in Figure 6.3a cover the range between 3.0 and 1.2 V (*vs*. Li/Li^+) and establish the absence of any redox peaks above 2.4V. In fact, it is possible to scan between 2.4 V and 1.2 V to obtain the redox behavior shown in Figure 6.3a.

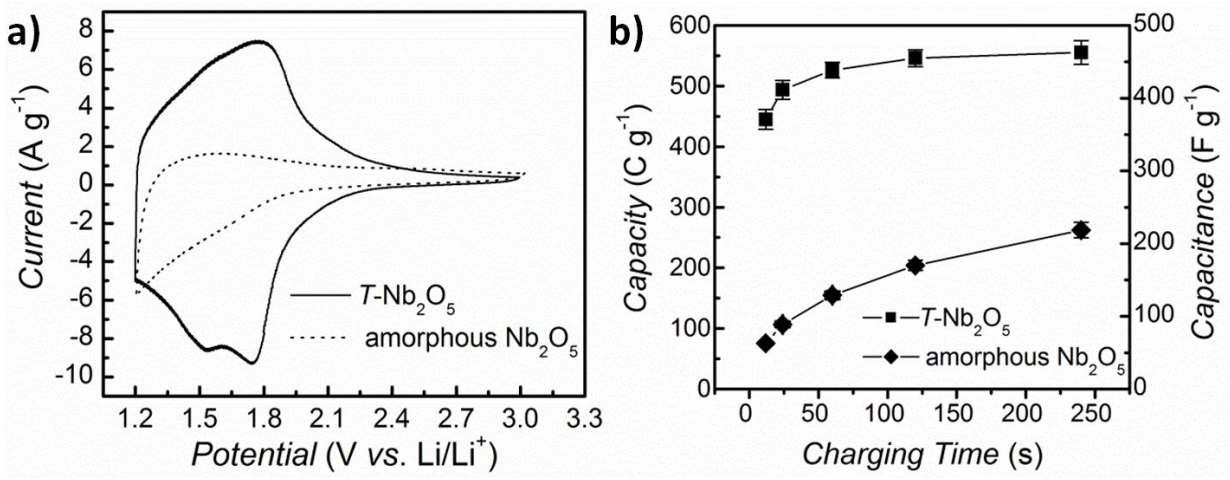

Figure 6.3. Voltammetric sweeps for Nb_2O_5 in lithium ion electrolyte: **a)** CVs at 10 mV s^{-1} for different Nb_2O_5 phases and **b)** charge storage as a function of charging time for the same materials. The *T*-phase demonstrates the highest level of charge storage capacity for all sweep rates investigated.

The amorphous aerogel material does not show any peaks in the CV scan and the specific current is significantly lower than the crystalline material. Amorphous Nb_2O_5 has been shown to have lower lithium capacity than crystalline Nb_2O_5 in mesoporous and sol-gel films as well.[79,81] Instead of the blue coloration seen in the crystalline materials, amorphous Nb_2O_5 exhibits a brown color during lithiation because of strong absorption in the blue.[85]

The kinetics of charge storage are influenced significantly by crystallizing Nb_2O_5. The differences between the crystalline and amorphous materials are quantified in Figure 6.3b based on a voltage window of 1.2 V. The highest capacity is achieved with the *T*-Nb_2O_5: at a charging time of only 12 seconds the capacity is approximately 450 C g^{-1}, corresponding to a capacitance of 370 F g^{-1}. As charging time increases, the capacity increases until a consistent value of 560 C g^{-1} is attained after about 2 minutes. The fact that over 80% of the capacity is accessed within 12 seconds indicates that the kinetic response for *T*-Nb_2O_5 is one of the fastest reported for transition metal oxides (*vide infra)*. The observation that surface area has limited effect on total

charge storage was reported for MnO_2 polytypes[80] and thus seems to be a characteristic of systems in which charge storage is faradaic and particle size is sub-micron. In contrast, the amorphous Nb_2O_5 aerogel has a significantly lower specific capacitance than the crystalline phase even though its surface area (187 m^2 g^{-1}) is much higher than *T*-Nb_2O_5. The great difference between the amorphous and crystalline phase shown in Figure 6.3b is a good indication of how faradaic processes lead to an additional capacitive storage mechanism which does not occur with the non-crystalline material. Moreover, as indicated by the kinetic response, this faradaic contribution occurs at very short timescales where diffusion-related processes are expected to be minimal.

Ex situ HR-TEM was used to investigate the ion intercalation and the structural stability of *T*-Nb_2O_5 during high-rate (100 mV s^{-1}) lithium insertion and extraction. To obtain the lithiated and delithiated *T*-Nb_2O_5, the cycling was stopped at 1.2 V and 3 V (*vs.* Li/Li^+), respectively. Figure 6.4b shows that the lattice parameter (3.25 Å) of *T*-Nb_2O_5 after lithiation was slightly larger than the lattice parameter (3.15 Å) of the pristine (180) plane. This indicates that the lattice parameter of the (180) plane is increased by 3% due to lithium insertion, which is in good agreement with prior XRD studies on lithium insertion into *T*- Nb_2O_5.(Ref. 86) The prior results of Kumagai and the study involving iso-oriented meosporous films suggest that the (180) plane of *T*-Nb_2O_5 may provide a favorable pathway for Li^+ transport[81] while the vacant interstitial sites between (001) planes are first occupied by lithium ions.[86] Upon delithiation, there is no evidence of a phase change. The HR-TEM image shown in Figure 6.4c corresponds to the (001) plane of *T*-Nb_2O_5. The *d*-spacing studies of HR-TEM images indicate that the structure of *T*-Nb_2O_5 did not change after 10 cycles of lithium insertion and extraction. In addition, Figure 6.4b and c demonstrate that a SEI layer was formed on the surface of Nb_2O_5 as expected from the use of low potentials during cycling.

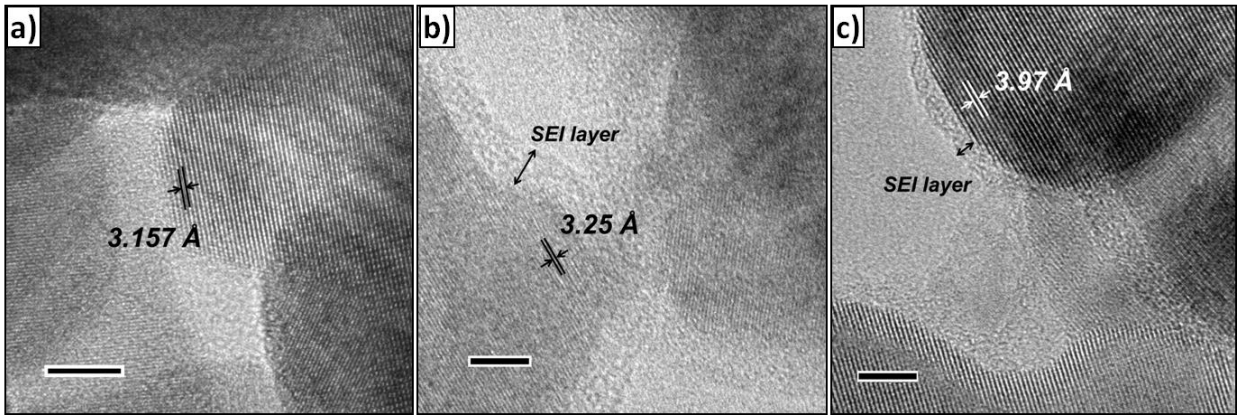

Figure 6.4. HR-TEM images of *T*-Nb_2O_5: **a)** pristine material, **b)** lithiated to 1.2 V (*vs.* Li/Li^+), **c)** delithiated to 3 V (*vs.* Li/Li^+) after cycling 10 times at 100 mV s^{-1}. (scale bar = 5 nm)

6.5 Electrolyte Ion Size Effects

The crystallographic dependence observed for Li^+ charge storage led us to consider the effect of ion size. The results shown in Figure 6.5a for the *T*-Nb_2O_5 are quite dramatic as substantially greater current occurs using the lithium-ion electrolyte as compared to the sodium ion electrolyte. Surface area-normalized capacitance (Figure 6.5b) shows that with the sodium-ion electrolyte, the amount of charge storage does not depend on crystallinity. The measured value of 20 μF cm^{-2} is a level generally associated with double-layer capacitance.[3] If capacitive energy storage using the sodium electrolyte occurs only from electrical double layer contributions, it is expected that the specific capacity increases with surface area. Thus, because of its greater surface area, it is not surprising that the amorphous Nb_2O_5 aerogel exhibits a larger gravimetric capacity (~40 C g^{-1} at 5 mV s^{-1}; Figure 6.6) than that of the crystalline phase. This behavior is very different from what is observed when using lithium electrolytes. Because of charge storage from faradaic reactions, the surface-area normalized capacitance of the crystalline material in lithium-ion electrolyte is at least an order of magnitude larger than in sodium for all sweep rates. The inability for the larger Na^+ to move within the frameworks of *T*-

Nb_2O_5 was reported by Kumagai *et al.*[87] and is a commonly observed feature for other intercalation compounds.

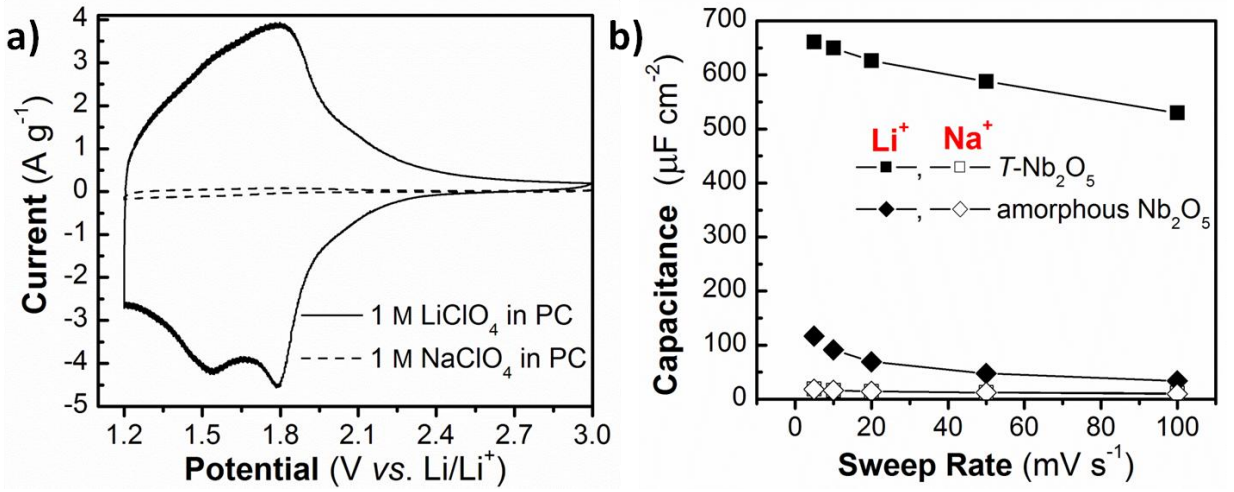

Figure 6.5. Effect of electrolyte ion size on electrochemical behavior of Nb_2O_5: **a)** CV at 5 mV s^{-1} for *T*-Nb_2O_5 using electrolytes for Li^+ or Na^+, **b)** the surface-area normalized capacitance for different Nb_2O_5 materials in Li^+ (closed) and Na^+ (open) electrolytes. Significant charge storage occurs only when using Li^+ electrolyte for the crystalline phase.

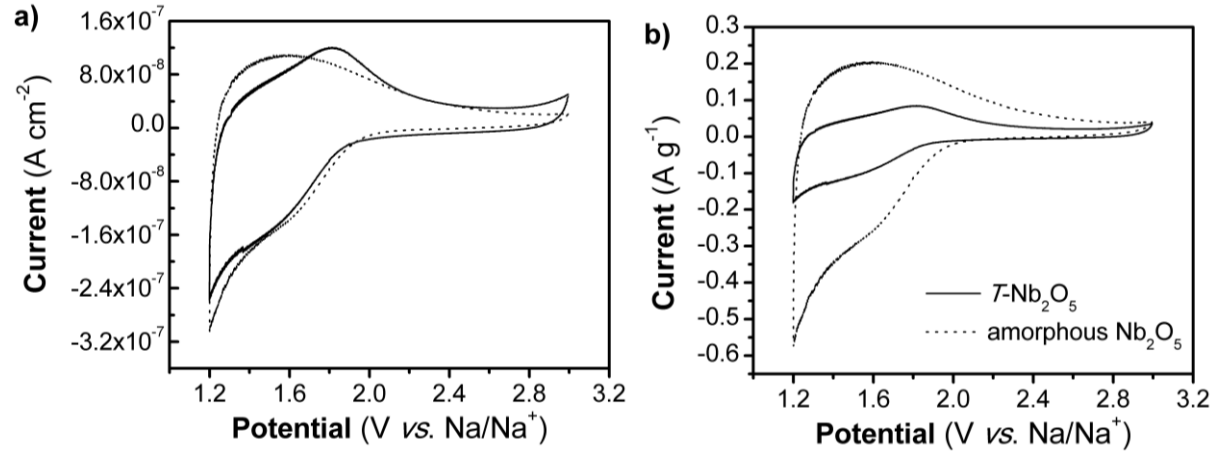

Figure 6.6. Voltammetric sweeps for Nb_2O_5 materials in sodium ion electrolyte. The results for the different materials are normalized by **a)** surface area and **b)** weight. In this electrolyte, the

surface area is more important than crystallinity. This indicates that the charge storage of Na^+ is primarily on the Nb_2O_5 surface.

6.6 Kinetic Behavior of *T*-Nb_2O_5

To obtain further insight concerning the kinetics of charge storage in *T*-Nb_2O_5, we adapted an analysis first used by Trasatti *et al.* to characterize the charge storage of RuO_2, a well-known pseudocapacitive material.[88] In this analysis, the overall capacity (Q) of a material is assumed to contain two contributions, that from capacitive charge storage ($Q_{capacitive}$, the "outer surface") and that from bulk charge storage (Q_{bulk}, the "inner surface"):

$$Q = Q_{capacitive} + Q_{bulk} \tag{6.2}$$

The bulk charge storage depends upon ion diffusion and, assuming semi-infinite linear diffusion, is expected to vary as $t^{1/2}$. By rewriting the above equation in terms of the sweep rate (v), the following relationship arises:

$$Q(v) = Q_{capacitive} + \text{constant}(v^{-1/2}) \tag{6.3}$$

In this analysis, a plot of Q vs. $v^{-1/2}$ yields a straight line whose y-intercept ($v = \infty$) is the "outer surface" capacity or the infinite-sweep rate capacity. Due to the possibility of polarization at high sweep rates, deviation from a straight line usually occurs, and intermediate sweep rates are then chosen to extrapolate to the y-intercept.[89]

The extrapolated infinite sweep-rate capacitance for *T*-Nb_2O_5 (Figure 6.7a) is estimated to be around 400 F g^{-1}, in good agreement with the charging behavior shown in Figure 6.3b. This value represents the amount of charge storage from capacitive processes, namely double-layer and/or pseudocapacitance. At slower sweep rates, diffusion-related processes begin to contribute and the total amount of charge storage becomes a combination of capacitive and diffusion components. In some materials, diffusion-related charge storage increases significantly and far outweighs the capacitive contribution. In the case of TiO_2 nanoparticles, for example, diffusion processes contributed between 85% and 45% of the total amount of charge

storage depending upon crystallite size.[90] What is particularly interesting with Nb_2O_5 is that even at slow sweep rates and reasonably large crystallite sizes (30-40 nm), diffusion processes contribute only a small amount of the total charge, less than 20% at 5 mV/s (Figure 6.7b).

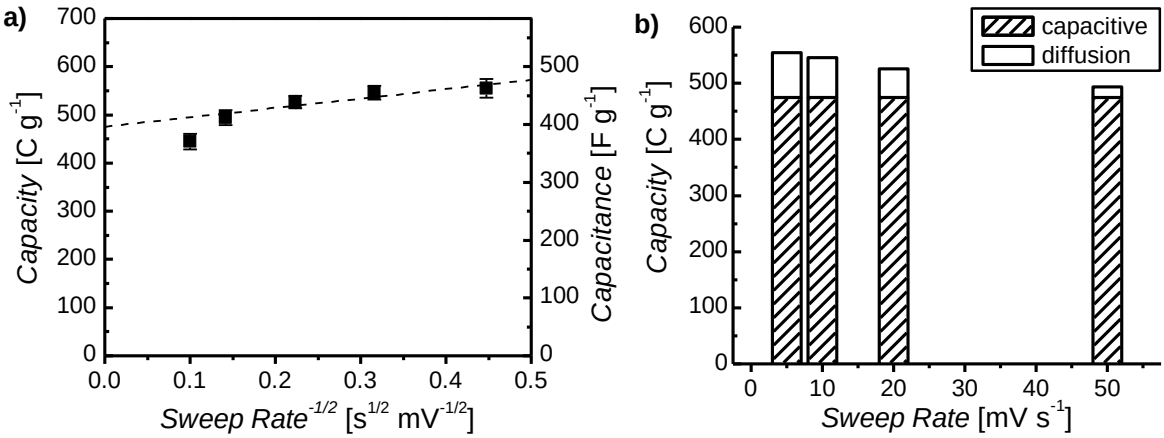

Figure 6.7. Determination of the infinite sweep-rate capacitance of *T*-Nb_2O_5: **a)** the capacity as a function of $v^{-1/2}$, the *y*-intercept is 470 C g^{-1} and represents the infinite sweep rate capacity, **b)** the contribution of the capacity at infinite sweep rate to the total charge storage is significant for all sweep rates investigated.

To provide some context for the extrapolated infinite sweep-rate capacitance, it is useful to make comparisons with both birnessite MnO_2 and RuO_2. Using non-aqueous lithium electrolytes similar to the experiments reported here, the results from Ma *et. al.* indicate a specific capacitance for birnessite of ~ 270 F g^{-1}.(Ref. 91) This is well below the 400 F g^{-1} shown in Figure 6.7a for *T*-Nb_2O_5. Direct comparisons with RuO_2 are not feasible for these electrolytes because crystalline anhydrous RuO_2 undergoes a phase transition upon lithiation.[92] With acid electrolytes, however, there is considerable experimental data. Recent results reported for 2 nm-thick RuO_2 nanoskins exhibited an infinite-sweep rate specific capacitance of ~ 480 F g^{-1}.(Ref. 93) Thus, even though the pseudocapacitance mechanisms are different for RuO_2 and *T*-Nb_2O_5, their charge storage kinetics at short times are quite comparable. While RuO_2 exhibits both high

electronic and ionic conductivity, Nb_2O_5, on the other hand, is an electronic insulator. Its bulk resistivity is ~ $3x10^4$ Ω-cm at 300K with a bandgap of ~3.4 eV.[94,95] However, the insertion of lithium into the structure apparently dopes the material and increases the electronic conductivity. Modeling the electrochemical impedance of *T*-Nb_2O_5 NCs before and after lithiation (Figure 6.8) indicates that the faradaic resistance decreases significantly after lithiation, from 14,309 Ω to 15.2 Ω. The mixed electronic and ionic conduction of reduced *T*-Nb_2O_5 was noted previously.[83] It should be noted that despite the dramatic improvement in electronic properties with lithiation, for practical applications utilizing thick electrodes, conductive additives would still be necessary for this material.

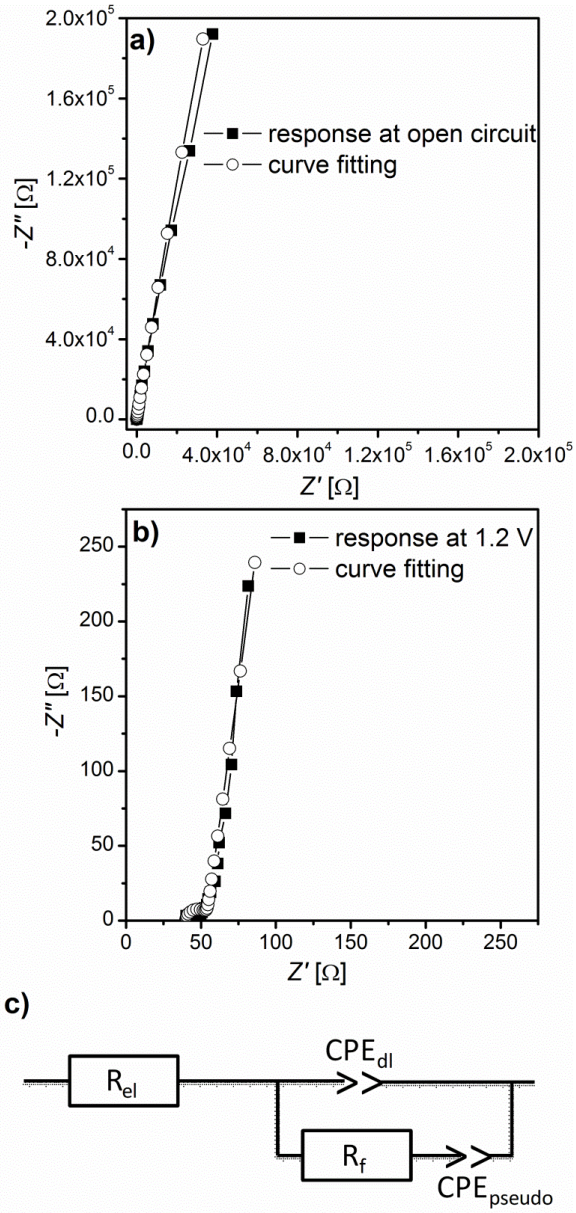

Figure 6.8. Nyquist representation of impedance spectra for the *T*-Nb_2O_5 electrode at two different potentials, **a)** before any lithiation at open-circuit and **b)** after lithiating to 1.2 V. The circuit model used for fitting is shown in **c)**, where R_{el} is the electrolyte resistance, CPE_{dl} is the double-layer capacitance present at all electrode/electrolyte interfaces, R_f is the faradaic charge transfer resistance, and CPE_{pseudo} is the pseudocapacitance. CPE is the constant phase element ($Z_{CPE} = [B(j\omega)^n]^{-1}$), where B and n are constants and ω is the frequency).

The question of how electronic conduction develops in lithiated Nb_2O_5 has been considered by several research groups. Orel *et al.* proposed that electron transport occurs due to a polaron hopping mechanism and showed that the conductivity increases by four orders of magnitude when Nb_2O_5 is chemically-lithiated.[79,96] Also relevant to the conductivity question is that shear structures of reduced monoclinic Nb_2O_5 become conductive with as little as four atomic % Nb^{+4} due to the addition of $4d^1$ electrons to the insulating structure.[94] Finally, a first-principles study of n-type doping in oxides suggested that Nb_2O_5 will become conductive once hydrogen is inserted into the lattice.[97] While the results of these studies are not necessarily consistent, they do underscore the point that the addition of small cation dopants into the crystalline Nb_2O_5 lattice increases the electronic conductivity, perhaps substantially and at relatively low dopant levels. It would seem that the development of enhanced electronic conductivity is of central importance in explaining why an insulator such as Nb_2O_5 exhibits a high rate pseudocapacitive response comparable to that of RuO_2.

6.7 Conclusions

The results presented here establish that the high specific capacitance observed with mesoporous iso-oriented films of Nb_2O_5 is, in fact, a fundamental property of this material. The significant difference between the crystalline and amorphous phases arises from the fast faradaic reactions which occur in crystalline Nb_2O_5, leading to an additional pseudocapacitive storage contribution. The extrapolated infinite sweep rate capacitance of ~400 F g^{-1} exceeds that of birnessite MnO_2 and is comparable to values obtained for RuO_2. Faradaic reactions in Nb_2O_5 occur over very short timescales and it is likely that Li^+ insertion occurs along preferred crystallographic pathways that provide an appropriate environment for fast ion transport. These pathways are apparently very size sensitive as experiments with a sodium electrolyte exhibit only double layer capacitance. The magnitude of electronic conductivity upon Li^+ insertion and the means by which electronic conduction develops in this wide band gap semiconductor remain

to be addressed. The surprising ability of Nb_2O_5 to store charge at high rates despite its insulating character is unusual as compared to most transition metal oxides. This work suggests that in searching for advanced electrochemical capacitor materials, compounds that become highly conductive during ion intercalation represent an exciting direction for the future.

Chapter 7. Intercalation Pseudocapacitance in *T*-Nb_2O_5

7.1 Introduction

Intercalation pseudocapacitance was introduced in Chapter 5 as a charge storage phenomenon characterized by ion insertion into a layered or tunnel structure, as illustrated in Figure 5.1c. Despite the fact that such a mechanism results in a change of potential with the amount of ion insertion, it is not considered capacitive due to kinetic limitations of solid-state diffusion. This limitation renders most intercalation-based materials suitable for timescales where charge storage occurs in hours, as in batteries. In the last chapter, the exceptionally rapid charge storage of *T*-Nb_2O_5 nanocrystals was demonstrated in a non-aqueous Li^+ electrolyte and it was shown that the charge storage was capacitive in nature. In this chapter, the kinetics of charge storage in *T*-Nb_2O_5 are quantified and, in the process, several characteristics necessary for intercalation pseudocapacitance are defined: a crystalline structure that offers 2D transport pathways and little structural change upon intercalation, currents that vary inversely with time, charge storage capacity that is mostly independent of rate, and redox peaks that exhibit small voltage offsets, even at high rates. The principal benefit realized from intercalation pseudocapacitance is that high levels of charge storage are achieved within short periods of time because there are no limitations from solid-state diffusion.

The phenomenon of intercalation pseudocapacitance and the high-rate behavior of *T*-Nb_2O_5 were investigated by using two different electrode techniques that provide a wide variation in sweep rates. For timescales between ~3 hours and 60 seconds (sweep rates of 0.1-20 mV s^{-1} within a voltage window of 1.2 V), a thin-film electrode was utilized. For shorter timescales where ohmic polarization is significant (60-500 mV s^{-1}), a cavity microelectrode was used where the active material was mixed with a conductive carbon black to alleviate the loss of electrical transport (ohmic losses).[98] In addition, thick films (~40 μm) of *T*-Nb_2O_5 were prepared to determine whether the high-rate capability was limited to thin films.

7.2 Methods

Synthesis. The synthesis of *T*-Nb_2O_5 nanocrystals was described in Chapter 6.2.

Characterization. Thin film electrodes were fabricated by drop-casting a well-sonicated solution of *T*-Nb_2O_5 in ethanol onto an oxygen plasma etched stainless steel foil. For thin film measurements, lithium foils served as the reference and counter electrodes, and the electrolyte was 1 M $LiClO_4$ in PC. For the microelectrode, *T*-Nb_2O_5 active material and carbon black (Timcal Super C65) powders were mixed in a 1:1 weight ratio to ensure good electrical contact. The mixture was packed into the microcavity (30 μm depth, 30 μm width), and subsequently immersed in the electrolyte. A 1 cm^2 platinum foil was used as the counter electrode and lithium foil served as the reference. Thick Nb_2O_5 electrodes were prepared by mixing the active material, carbon black (Timcal Super C65) and PVdF (Kynar) binder in a 80:10:10 weight ratio. The slurry was drop cast onto 12 mm diameter aluminum disk current collectors and dried at 80°C for 12 hours. The electrode loading was between 1 and 1.5 mg cm^{-2} with a thickness of 40±5 μm. Measurements of the thick Nb_2O_5 electrodes were performed in 3-electrode Swagelok cells with the Nb_2O_5 electrode as the working electrode, activated carbon as the counter electrode, a glass fiber separator (Whatman, GF/A) saturated with 1 M $LiClO_4$ in PC, and a lithium foil reference. All measurements were carried out in argon-filled gloveboxes between 1.2 and 3 V (*vs.* Li/Li^+) with oxygen and moisture levels of <1 ppm. Cyclic voltammetry and galvanostatic cycling were performed using PAR EG&G 273 and Bio-Logic VMP3 potentiostats.

In situ x-ray absorption was performed using thin films of *T*-Nb_2O_5 cast a from well-sonicated ethanol solution onto carbon-coated aluminum. 2032-type coin cells were modified to include an x-ray window by drilling ~3 mm diameter holes through the cathode casing and epoxying a 125 μm-thick Kapton window on the outside of the casing. Both sides of the window were then coated with 100 nm-thick aluminum layers using a vacuum evaporator. Cells were assembled with a lithium anode, a 1 M $LiClO_4$ in PC electrolyte, and a Whatman glassy fiber separator.

7.3 Electrochemical features of Intercalation Pseudocapacitance

Figure 7.1a shows CVs from 100-500 mV s^{-1} in a cavity microelectrode where it is evident that both anodic and cathodic peaks are broad, *ca*. 600 mV. There is also a noticeable peak shift (and increase in peak separation ΔE_p) as the sweep rate increases, but the capacity remains reversible. Figure 7.1b presents a plot of log(*i*) *vs*. log(*v*) from 0.1-500 mV s^{-1} for both cathodic and anodic peaks. Assuming that the current obeys a power-law relationship with the sweep rate leads to:[99]

$$i = av^b \tag{7.1}$$

where *a* and *b* are adjustable values. While a *b*-value of 0.5 would indicate that the current is controlled by semi-infinite linear diffusion, a value of 1 indicates that the current is surface-controlled. For sweep rates ranging from 0.1-20 mV s^{-1}, corresponding to charging times >60 seconds, the *b*-value for both the cathodic and anodic peaks is 1, indicating that the kinetics are surface-controlled, and thus fast. Figure 7.1b also exhibits a change in the slope of the anodic and cathodic peak currents at ~50 mV s^{-1}. This change in slope corresponds to a decrease in *b*-value to 0.8 and 0.7 for the cathodic and anodic currents, respectively, at sweep rates >50 mV s^{-1} (charging times <20 seconds). This limitation to the rate capability can arise from numerous sources including an increase of the ohmic contribution (active material resistance, SEI resistance) and/or diffusion constraints/limitations.[100] In the limit of slow diffusion, *b* would approach a value of 0.5 as described above.

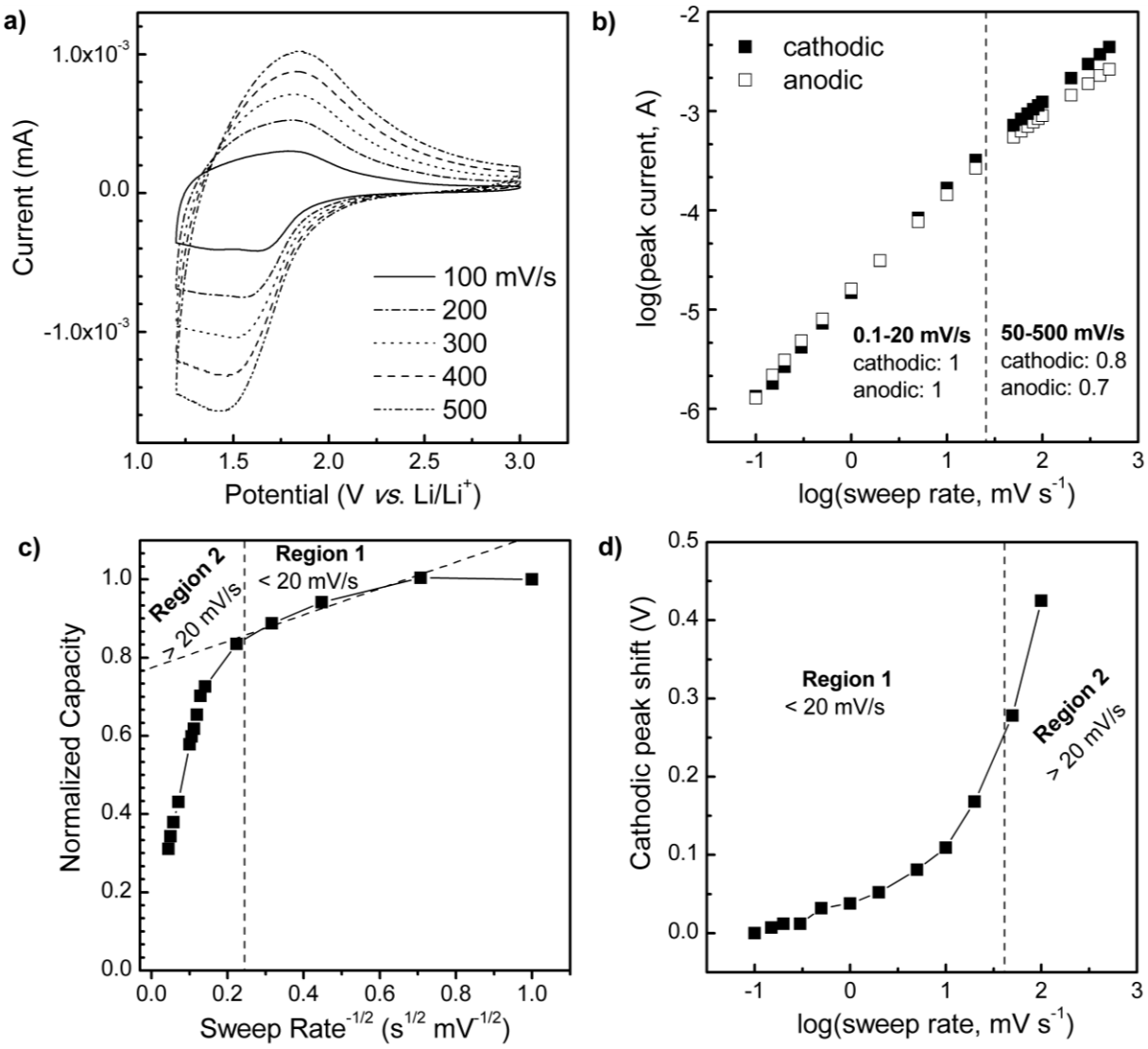

Figure 7.1. Kinetic analysis of the electrochemical behavior of *T*-Nb_2O_5: **a)** CVs from 100 to 500 mV s^{-1} demonstrate the high-rate capability of the material. **b)** *b*-value determination of the peak anodic and cathodic currents shows that this value is approximately 1 up to 50 mV·s^{-1}. This indicates that even at the peak currents, charge storage is capacitive. **c)** Capacity *vs.* $v^{-1/2}$ allows for the separation of diffusion-controlled capacity from capacitive-controlled capacity; two distinct kinetic regions emerge when the sweep rate is varied from 1 to 500 mV s^{-1}. The dashed diagonal line corresponds to the extrapolation of the infinite sweep rate capacitance using the capacity between 2 and 20 mV s^{-1}. **d)** The variation of the cathodic peak voltage with the sweep

rate exhibits a region of small peak separation followed by increased separation at 20 mV s^{-1}, and represents another method of identifying systems with facile intercalation kinetics.

As described by Eqn. 6.3, in a plot of Q *vs.* $v^{-1/2}$ regions that are linear represent capacity limited by semi-infinite linear diffusion whereas capacitive contributions are independent of the sweep rate. Figure 7.1c shows the plot of normalized capacity *vs.* $v^{-1/2}$ for T-Nb_2O_5 from 1-500 mV s^{-1}. Analogous to the behavior of the peak current in Figure 7.1b, there are two distinct regions in Figure 7.1c. In Region 1, at sweep rates <20 mV s^{-1}, the capacity is mostly independent of sweep rate. The magnitude of the capacity is ~130 mAh g^{-1} or ~65% of the theoretical value based on a 2-electron redox reaction with Nb_2O_5. In this range, solid-state lithium-ion diffusion is not the rate-limiting step for charge storage. In Region 2, from 50-500 mV s^{-1}, the capacity decreases linearly with $v^{-1/2}$. This indicates that charge storage is mainly diffusion-controlled at high sweep rates. That is, for charging times of <20 seconds, diffusion is rate-limiting, similar to most traditional battery electrodes. However, for charging times of 1 minute (60C) or longer, there is no indication of diffusion limitations and this intercalation-based system behaves in a fully capacitive manner.

Another feature of T-Nb_2O_5 at sweep rates <20 mV s^{-1} is that the peak voltage shifts with sweep rate are small (Figure 7.1d). The cathodic peak shift is <0.1 V at sweep rates below 10 mV s^{-1}. As a result, the anodic and cathodic peaks overlap at 0.1 mV s^{-1} (Figure 7.2) and it is in this behavior that the similarity to surface redox reactions is most apparent.[101] In many lithium-ion intercalation materials, the peak separation is significant even in thin films and at slow sweep rates (*e.g.* ΔE_p = 0.13 V for $LiCoO_2$ at 0.1 mV s^{-1}).[102] This type of behavior is often associated with crystallographic phase changes during the faradaic process, and contrasts with intercalation materials that form a solid solution, like T-Nb_2O_5. Besides identifying facile intercalation, the peak voltage separation is related to the high-power capability of a material. As the charging time decreases, that is at higher current densities, the peak separation in a

battery material increases due to polarization (reflecting the higher overpotentials necessary to deliver the higher currents), so that at higher rates the energy required to fully charge the material is significantly larger than the energy available upon discharge.

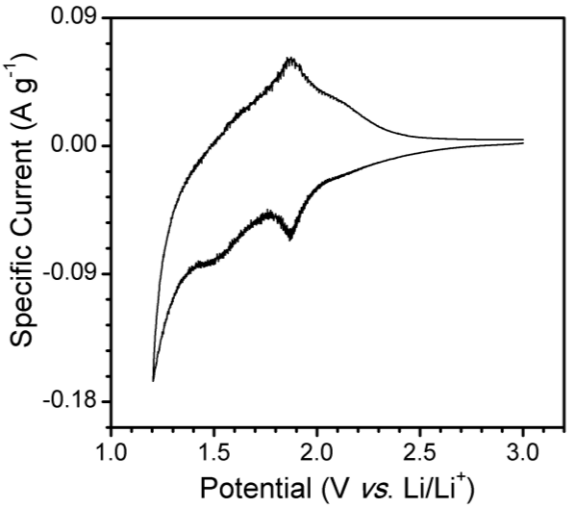

Figure 7.2. Cyclic voltammetry of a thin film electrode of *T*-Nb_2O_5 at 0.1 mV s^{-1}. There is no anodic and cathodic peak separation at this timescale. The irreversible peak at 1.2 V is likely due to the formation of the SEI layer, which accounts for the low coulombic efficiency at slow sweep rates in the thin film and microelectrodes.

The high-rate behavior of *T*-Nb_2O_5 is not limited to thin films or to experiments with small amounts of active material. The constant-current charge/discharge of a 40-μm thick *T*-Nb_2O_5 (1 mg cm^{-2}) electrode at a 10C rate is shown in Figure 7.3a. At this rate, the capacity is 130 mAh g^{-1} and *E* varies linearly with *Q* as expected for a pseudocapacitive process from Equation 5.2. This represents capacities typical of battery materials but at rates closer to those of supercapacitors. The rate capability of *T*-Nb_2O_5 from 1-1,000C is shown in Figure 7.3b and compared with that of $Li_4Ti_5O_{12}$ (of comparable electrode dimensions).[103] $Li_4Ti_5O_{12}$ is chosen as an example of a high-rate lithium-ion anode material. The rate capability for *T*-Nb_2O_5 is significantly better than $Li_4Ti_5O_{12}$ above 30C and even at a 1,000C-rate the capacity of the thick

T-Nb_2O_5 electrode is ~40 mAh g^{-1}. The thick electrode results verify that the intercalation pseudocapacitance mechanism is not due to thin-film or surface effects, such as vacancies or contributions of the first few atoms from the surface.

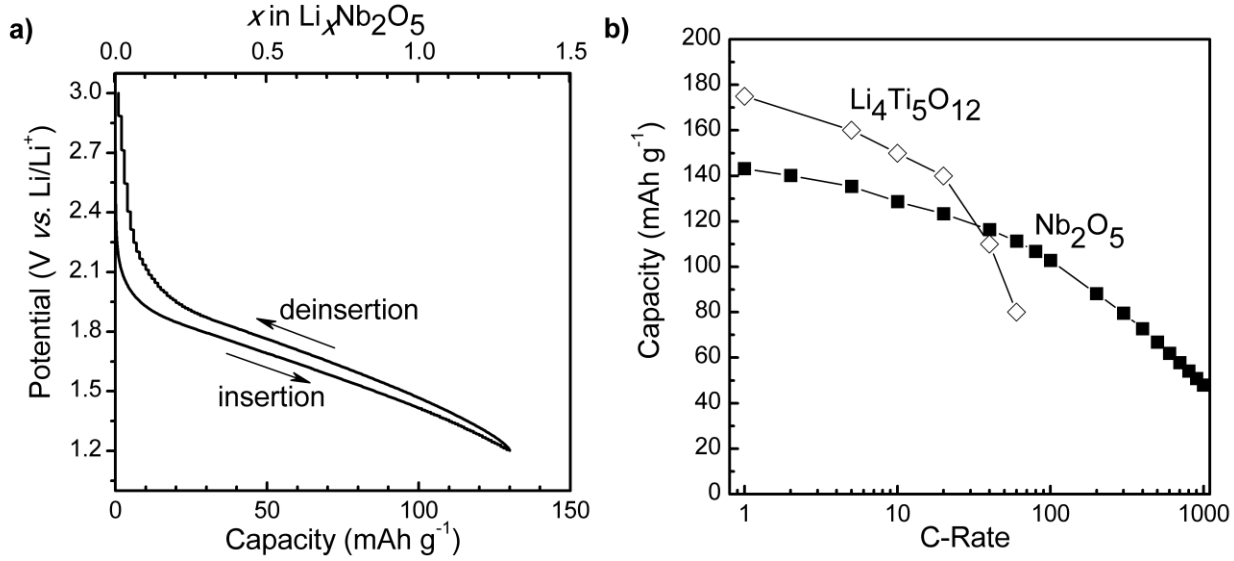

Figure 7.3. Electrochemical cycling of a 40 μm-thick *T*-Nb_2O_5 electrode: **a)** Galvanostatic cycling of a thick Nb_2O_5 electrode at a 10C rate. **b)** Comparison of the rate capability of *T*-Nb_2O_5 with a high-rate lithium-ion anode, $Li_4Ti_5O_{12}$, at various C-rates ($Li_4Ti_5O_{12}$ data reproduced from Ref. 103).

7.4 Structural Features of Intercalation Pseudocapacitance

The high-rate capability of *T*-Nb_2O_5 implies that the crystal structure permits exceptionally rapid ionic transport. As shown in Figure 7.4a, the unit cell has sheets of edge- or corner-sharing distorted polyhedra lying parallel to the (001) plane, with each Nb^{5+} surrounded by either 6 or 7 O^{2-}. The polyhedra are exclusively corner-sharing along the [001] direction with 5% of the Nb^{5+} ions randomly located in 9-coordinate sites between the (001) polyhedral planes.[104] The mostly empty octahedral sites between (001) planes provide natural tunnels for

lithium-ion transport throughout the *a*-*b* plane. Calculations indicate that the (001) plane allows degenerate pathways with low energy barriers for ion transport.[105]

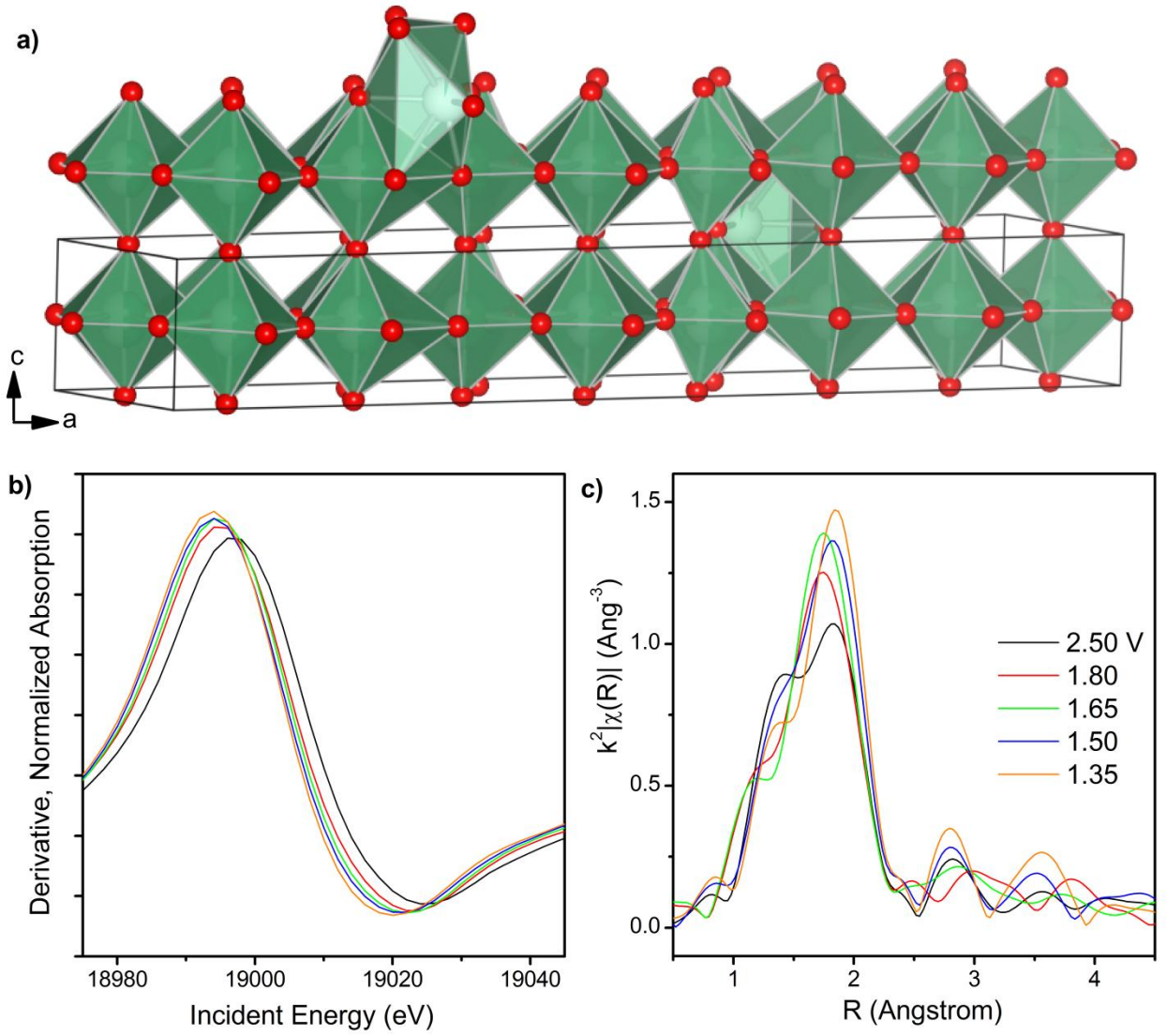

Figure 7.4. Structural features of lithium intercalation in *T*-Nb_2O_5: **a)** The structure of *T*-Nb_2O_5 stacked along the *c*-axis demonstrates the layered arrangement of oxygen (red) and niobium (inside polyhedra) atoms along the *a*-*b* plane. **b)** Derivative of Nb K-edge x-ray absorption near-edge spectra at selected cell voltages, showing a systematic shift to lower energies as Nb^{5+} is reduced to Nb^{4+}. **c)** k^2-weighted Fourier-transformed Nb K-edge extended x-ray absorption fine structure at selected cell voltages.

A previous *in situ* x-ray diffraction (XRD) study showed that the insertion of lithium into *T*-Nb_2O_5 results in a solid solution with no apparent phase changes,[78] and negligible changes to lattice constants[106] and unit cell volume[86] up to ~1.25 Li^+/Nb_2O_5, while *in situ* x-ray absorption spectroscopy (XAS) demonstrated that lithiation reduces Nb^{5+} to Nb^{4+}.(Ref. 78) The *in situ* XAS studies carried out here confirm that lithiation results in a continuous change in oxidation state (Figure 7.4b) while the Fourier-transform of the extended x-ray absorption fine structure (EXAFS) indicates that the insertion reaction proceeds through two stages (Figure 7.4c). From 2.5 to 1.75 V, the EXAFS signal from the various Nb-O bond lengths in Nb_2O_5 (1.40-1.85 Å) merges to a single peak at an intermediate bond length (1.75 Å) indicating that lithiation increases the Nb-centered symmetry. The lithiation is probably faster at low Li^+ levels[86] due to greater availability of sites and less interaction between cations. At lower potentials, the new EXAFS peak shifts to longer bond distances (1.85 Å) as a consequence of increased Li-O interactions at higher Li^+ content. These structural studies emphasize the value of an open, layered structure to enable rapid ion transport within the active material.

7.5 Conclusions

The results presented in this study establish that *T*-Nb_2O_5 exhibits electrochemical features of a pseudocapacitive material despite charge storage occurring in the bulk. Such behavior is consistent with intercalation pseudocapacitance. The electrochemical features indicative of this mechanism are currents that are linearly proportional to the sweep rate, capacity that does not vary significantly with charging time, and peak potentials that do not shift significantly with sweep rate. A key "design rule" for intercalation pseudocapacitance at the atomic scale is a structure that does not undergo phase transformations upon intercalation. In addition, facile 2D lithium-ion diffusion pathways are important. Charge storage that behaves as a quasi-2D process exhibits similar behavior to 2D surface adsorption reactions.[101] These

features contrast with those of pseudocapacitive $RuO_2 \cdot xH_2O$ where charge storage occurs mainly on the surface or near-surface[73–75,107] as summarized in Table 7.1.

Table 7.1. Comparison between charge storage in two different pseudocapacitive materials: $RuO_2 \cdot xH_2O$ and *T*-Nb_2O_5 both exhibit capacitive behavior. The mechanism of charge storage, however, is different and results in different structural requirements for high capacitance.

	$RuO_2 \cdot xH_2O$	***T*-Nb_2O_5**
Electrolyte	H^+, aqueous[75]	Li^+, non-aqueous
Structure	Amorphous/nanocrystalline[73,107]	Crystalline
Structural water	Necessary for proton conduction[107]	Not necessary
Charge storage mechanism	Surface/near-surface[73,74]	Bulk
Pseudocapacitance type	Adsorption redox	Intercalation

The results here are exciting because they demonstrate that for charging times as fast as 1 minute (60C rate), there are no diffusion limitations in *T*-Nb_2O_5. As the high-rate capability is due to fast ion diffusion in the bulk, this mechanism may be very good for thick electrodes because surface exposure to the electrolyte is not critical. To achieve devices with high energy density, further engineering at the nanoscale and beyond will be necessary to preserve the atomic scale behavior observed in thin films and microelectrodes. In particular, maintaining proper electronic conduction pathways will be critical.

Chapter 8. Pseudocapacitance in TiO_2 Nanosheets

8.1 Introduction

This section describes the electrochemical characterization of anatase nanosheets (NS) with exposed {001} facets. A detailed kinetic analysis is used to determine their energy storage and rate capabilities as compared to anatase nanocrystals (NCs), as well as to demonstrate for the first time the storage of sodium-ions in TiO_2. Nanosheets are intriguing for energy storage applications due to the fact that nearly the entire surface of the material can be exposed to the electrolyte leading to fast kinetics. In addition, the material can be engineered to grow in particular directions[108–110] leading to the exposure of a particular surface facet to the electrolyte. Theoretical calculations have shown that anatase surface orientation[111] and nanosheet thickness[112] play an important part in determining the material behavior. Previous research on anatase TiO_2 nanosheets[113–115] has shown improved electrochemical behavior, but in these cases the energy storage properties were investigated with composite electrodes that utilized carbons and binders. While such electrodes are essential for device applications, they make the determination of fundamental behavior difficult. Here, thin-film electrodes without any carbon or binder are utilized in order to characterize the behavior of only the nanosheets.

8.2 Methods

Synthesis. The solvothermal synthesis of anatase TiO_2 NS with exposed {001} facets has been reported previously.[109] Briefly, 5 mL of benzyl alcohol, 2 mL of oleylamine, and 0.25 mL of titanium isopropoxide are sealed in a Teflon-lined autoclave and heated at 180°C for 1 day. The resulting solution is centrifuged and the white precipitates washed with alternating cycles of chloroform and ethanol. The addition of a small amount of water (60 μL) leads to the growth of anatase NCs with exposed (010) facets. To yield dispersions in ethanol, the TiO_2 went through a 7 day ion-exchange process in tetrabutylammonium hydroxide in ethanol to replace the

oleylamine. For electrochemical measurements, the concentration of TiO_2 in ethanol was 1 mg mL^{-1}.

Characterization. Electrochemical behavior was investigated using drop-cast films (~20 μg cm^{-2}) of NS and NCs on stainless steel. The three-electrode measurements were performed with lithium metal counter and reference electrodes and 1 M $LiClO_4$ in PC as the electrolyte. For the Na-ion experiments, the cell consisted of sodium metal counter and reference electrodes and 1 M $NaClO_4$ in PC as the electrolyte. Cyclic voltammetry was performed from 1 to 100 mV s^{-1} between 1 and 3 V (*vs.* Li/Li^+ or Na/Na^+). All electrochemical cells were tested in an argon-filled glovebox with H_2O and O_2 levels < 1 ppm.

Powder X-ray diffraction (XRD) was performed on the Rigaku Miniflex II. X-ray photoelectron spectroscopy (XPS) measurements were taken with the Kratos AXIS Ultra using a monochromated Al X-ray source at 10 mA and 15 kV and a 20 eV pass energy. XPS of cycled electrodes was performed by rinsing the samples with dimethyl carbonate (DMC) and loading them into an inert atmosphere transfer chamber, which was then connected directly to the XPS chamber. All XPS spectra were calibrated to the C 1s peak at 284.9 eV and peak fitting was performed with the Casa XPS program using a 70:30 Gaussian-Lorentzian lineshape. Transmission electron microscopy (TEM) was performed with the JEOL JEM 1200-EX. TEM of cycled NS material was performed by drop-casting a small amount of NS in ethanol onto a Cu TEM grid, which was then used as the working electrode in the electrochemical cell. Cyclic voltammetry was performed for 6 cycles at 10 mV s^{-1} between 1 and 3 V, then the grid was rinsed with DMC and transferred under an inert atmosphere into the TEM with minimal ambient atmosphere exposure. High resolution TEM (HR TEM) was performed with the FEI Titan 80/300 kV S/TEM.

8.3 Results & Discussion

XRD of TiO_2 NS before and after ion-exchange and TiO_2 NC are shown in Figure 8.1. As demonstrated previously,[109] the major peaks in the diffraction pattern of these TiO_2 NS are at 48.55 and 62.65° 2θ corresponding to the (200) and (204) reflections of anatase. The weak reflections at 25.4 and 39.25° correspond to the (101) and (004) reflections of anatase. This type of diffraction pattern is indicative of two dimensional crystal growth in the *a-b* directions with ordering along the *c* direction. It has been shown previously that the oleylamine ligand binds tightly to the (001) facet of the NS and results in a lamellar structure. After ion exchange, the NS become randomly ordered and the diffraction pattern is featureless. The addition of water to the synthesis results in NCs as demonstrated by the fact that the anatase reflections are now those of bulk TiO_2.

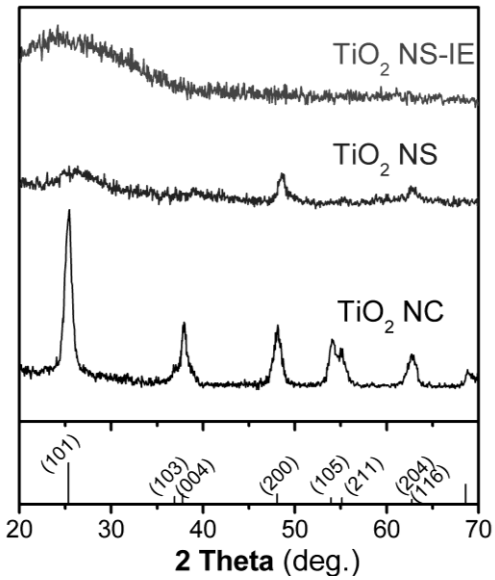

Figure 8.1. XRD of TiO_2 nanocrystals (NC), nanosheets (NS), and NS after ion-exchange (NS-IE). The reference pattern corresponds to anatase TiO_2, JCPDS card #21-1272.

TEM of the NS and NC after ion-exchange, and the electron diffraction pattern for the NS, are shown in Figure 8.2. The NS exhibit sheet-like morphology, and the thickness of each

sheet was previously measured to be approximately 7.5 Å corresponding to molecular layer thickness. The electron diffraction pattern corresponds to anatase TiO_2. The intensity of the diffraction rings correlates well with the high intensity peaks in the XRD pattern of the NS before ion exchange. The NCs grow in a rhombohedral morphology of approximately 70 nm in length and 40 nm in width. The HR TEM micrograph for the NS after ion exchange is shown in Figure 8.3. The thin sheet like morphology of the NS is clearly evidenced at the edges of the material.

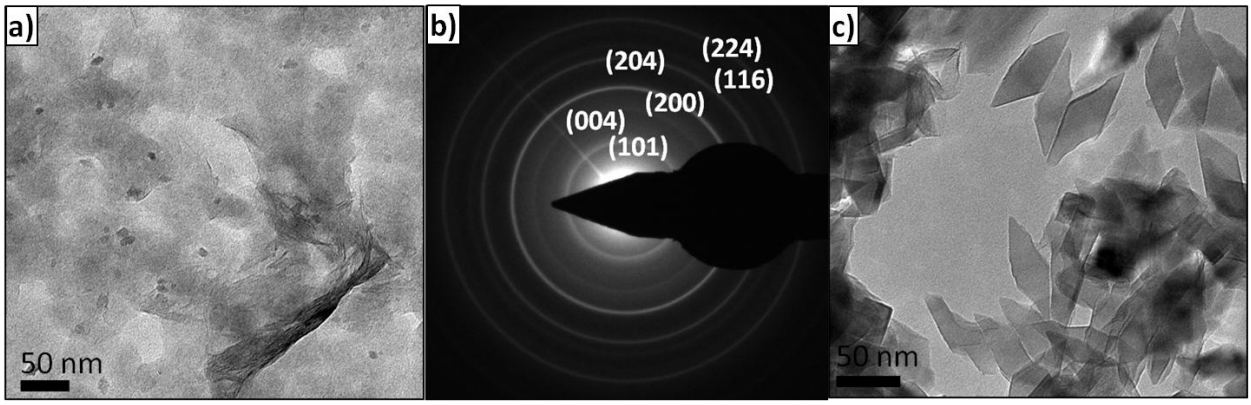

Figure 8.2. **a)** TEM of NS after ion-exchange and **b)** corresponding electron diffraction pattern indexed to anatase; **c)** TEM of NC after ion-exchange.

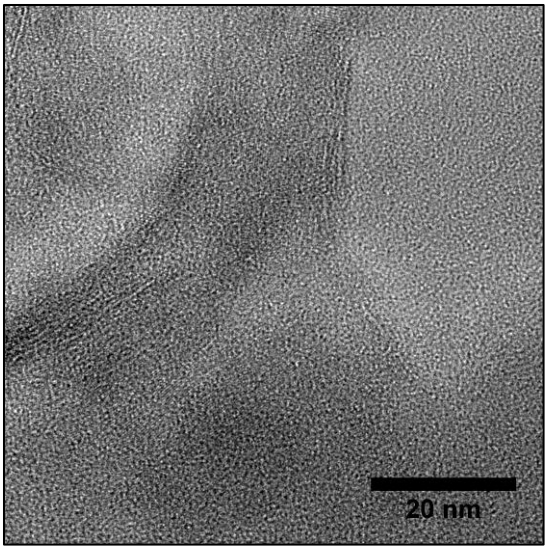

Figure 8.3. HR-TEM of the NS after ion-exchange.

The cyclic voltammogram (CV) for the first 10 cycles at 10 mV s^{-1} of NS and NCs are shown in Figure 8.4a and b. In the case of the NS, cycling between 1 and 3 V *vs*. Li/Li^+ initially results in a low capacity with cathodic peaks at 2.1, 1.57, and 1.1 V and anodic peaks at 1.44 and 2 V. After 10 cycles the CV becomes stable and there is one set of broad peaks at 1.3 and 1.48 V for the cathodic and anodic currents, respectively. During the first 10 cycles, the capacity of the NS electrode increases from 99 to 135 mAh g^{-1}. In addition, there was obvious blue electrochromism of the electrode, indicative of reduction of TiO_2. A TEM micrograph of the NS after cycling is shown in the inset of Figure 8.4a. While the material appears to remain in a sheet-like morphology, the surface is covered entirely by the SEI layer. In the case of the NCs, the first cycle in the CV results in a set of sharp peaks (at 1.65 and 2.3 V for the cathodic and anodic currents, respectively) corresponding to Li^+ insertion/de-insertion in bulk anatase. There is an additional cathodic peak at 1 V due to either the irreversible insertion of Li^+ into the NCs or the growth of the SEI on the surface. Further cycling down to 1 V at 10 mV s^{-1} reduced the capacity from 136 to 67 mAh g^{-1}.

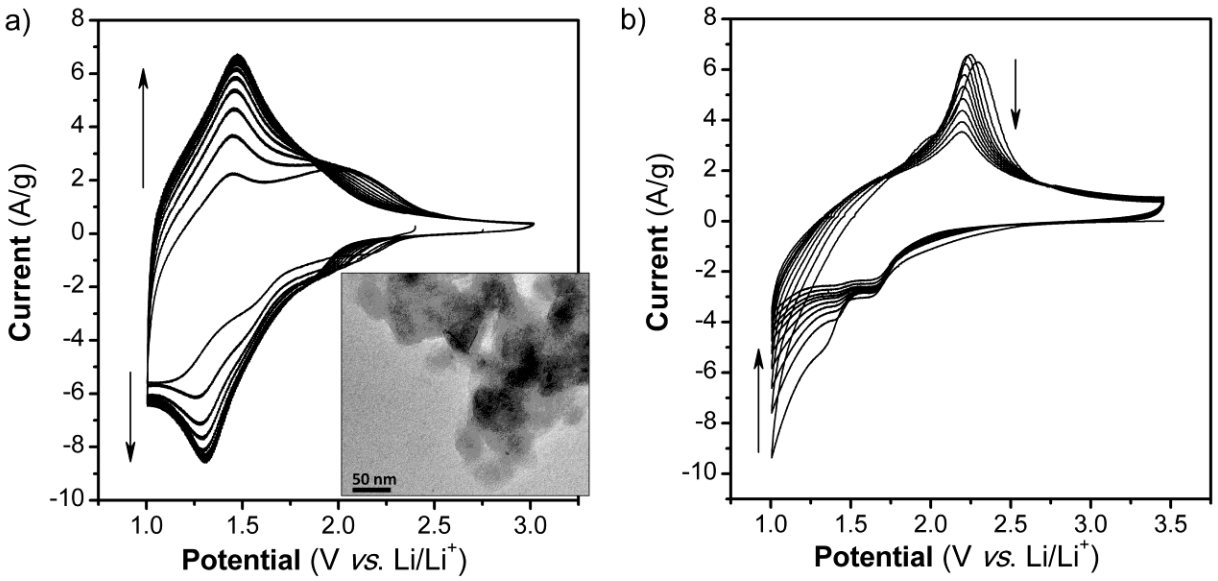

Figure 8.4. CVs at 10 mV s^{-1} in Li^+ for TiO_2 **a)** NS and **b)** NC. The inset of a) shows a TEM micrograph of the NS after cycling. After 10 cycles at this rate, the capacity of the NS increases while in the case of the NC, it fades.

The significant peak shift to lower potentials indicates that the lithium storage sites in the NS are different from those in the NC. The shape of the NS CV in Li^+ electrolyte has more in common with that of TiO_2(B)[116,117] and particularly hydrogen titanate ($H_2Ti_3O_7$)[118,119] than anatase. While there is a possibility of the NS undergoing a phase transformation during the ion-exchange in TBAOH,[120] there are no reports of such processes occurring at room temperature. In addition, the electron diffraction pattern taken after ion-exchange does not index to $H_2Ti_3O_7$ or TiO_2(B) and furthermore, the ion-exchange process does not transform the NC. During the first 10 cyclic voltammetry cycles, the NS undergo some kind of transformation *in situ* as the capacity increases. According to theoretical work, the transition from anatase to lepidocrocite TiO_2 can occur with no energy barrier for a bilayer of anatase oriented along the (001) direction.[121] Lepidocrocite TiO_2 is a building block of the titanates[122] which, when dehydrated, transform into TiO_2(B).[117] This close structural relationship between anatase NS of

only a few molecular layers and lepidocrocite TiO_2 may explain the reason why the NS store Li^+ at potentials commonly associated with hydrogen titanate and TiO_2(B).

The XPS scans of the O 1s, Ti 2p and N 1s regions in TiO_2 NS before and after cycling at 10 mV s^{-1} are shown in Figure 8.5. For the O 1s region (Figure 8.5a), initially there is a large peak corresponding to Ti-O bonds in TiO_2 and a smaller broad peak corresponding to hydroxide bonds, presumably due to the presence of tetrabutylammonium hydroxide. After cycling, the O 1s region contains additional contributions from O-C, O-N, and O-Cl bonds which have to do with the composition of the SEI layer. In the Ti 2p region (Figure 8.5b), before and after cycling the oxidation state of Ti corresponds to Ti^{4+} in TiO_2. The slight shift in the binding energy after cycling indicates that some Li^+ may remain in the NS. In the N 1s region (Figure 8.5c) initially there is one peak corresponding to the presence of tetrabutylammonium. After cycling, that peak disappears and instead there is a peak corresponding to nitrate, presumably due to the presence of lithium nitrate in the SEI products.

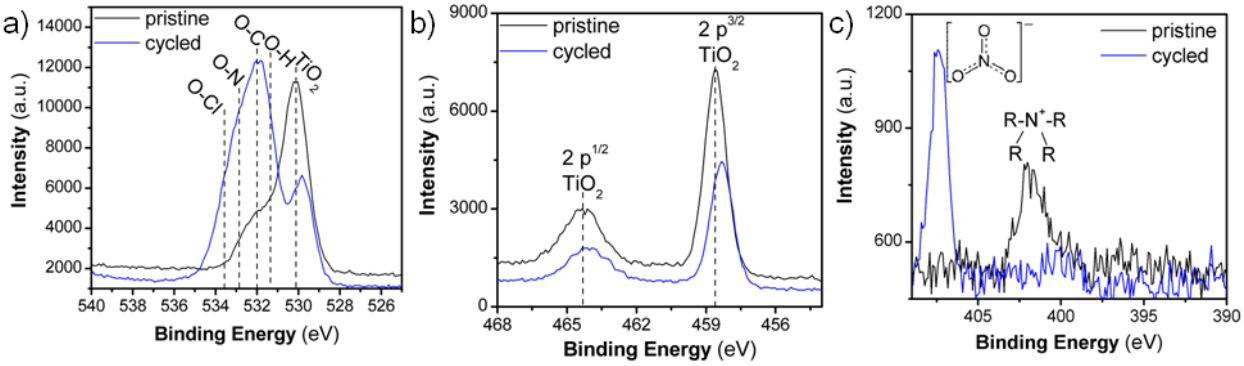

Figure 8.5. Core XPS spectra of the **a)** O 1s, **b)** Ti 2p, and **c)** N 1s regions of TiO_2 NS before and after cycling in a Li^+ electrolyte at 10 mV s^{-1}.

We investigated the kinetics of the NS (Figure 8.6) using several different analytical techniques that take advantage of the differences between diffusion and capacitive charge storage processes, as described in the previous two chapters. In Figure 8.6a, the capacity of the

NS (Q) is plotted *vs.* $v^{-1/2}$ from 1 to 100 mV s^{-1}. For the NS, up to 20 mV s^{-1} the Q *vs.* $v^{-1/2}$ plot is relatively constant. At this sweep rate the charging time is only 60 sec. In this region, the kinetics are not controlled by semi-infinite diffusion, corresponding well with the fact that the material is mostly surface. After 20 mV s^{-1} the capacity begins to change rapidly in a linear fashion corresponding to diffusion-controlled behavior.

In Figure 8.6b, the b-value for the cathodic and anodic peak currents in TiO_2 NS is 0.9 from 1 to 100 mV s^{-1}. There is a small amount of current that is diffusion-controlled since the b-value is not 1. While a small deviation in the linear fit is observed at 20 mV s^{-1} ($\log(v) = 1.3$), the shift to diffusion-control is not as obvious as in the Q *vs.* $v^{-1/2}$ plot of Figure 8.6a.

Lastly, one hallmark of surface-controlled reactions are small peak voltage offsets, with perfect surface-controlled behavior exhibiting 0 V offset at slow rates.[101] The ΔE_p *vs.* $\log(v)$ plot is shown in Figure 8.6c. In the case of the NS, at 1 mV s^{-1} the peak voltage offset is 0.14 V (Figure 8.7) and remains relatively constant up to 5 mV s^{-1} followed by significant increase above 20 mV s^{-1} which correlates well with the switch to fully diffusion-controlled behavior at faster sweep rates.

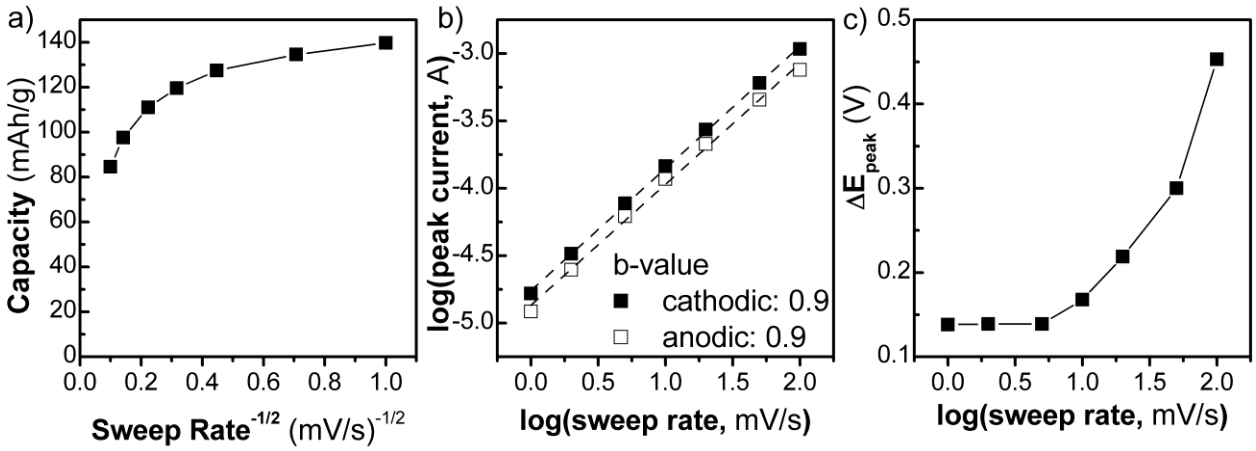

Figure 8.6. Kinetic analysis of the TiO_2 NS cycled in Li^+ at various sweep rates, from 1-100 mV s^{-1}. **a)** Capacity *vs.* sweep rate$^{-1/2}$, **b)** determination of the b-value using the peak current relationship to sweep rate, and **c)** peak voltage separation, ΔE_p as a function of sweep rate.

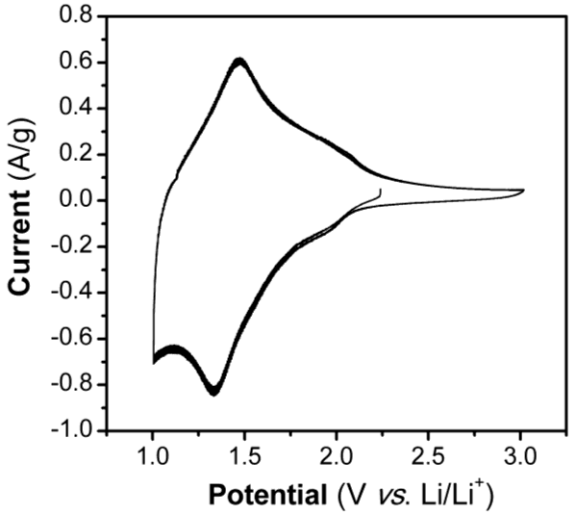

Figure 8.7. CV at 1 mV s^{-1} for TiO_2 NS in a Li^+ electrolyte for 3 cycles. The peak voltage offset at this rate is 0.14 V.

To determine where the diffusion contributions occur in the CV plots, we performed a more detailed analysis of the current, this time at all potential values for sweep rates from 1 to 10 mV s^{-1} (Figure 8.8). In this analysis, the current at a particular voltage again contains contributions from diffusion and capacitive processes:[123]

$$i(V) = k_1 v + k_2 v^{1/2} \quad (8.1)$$

here, k_1 and k_2 are constants for a particular potential. Plotting $i(V)/v^{1/2}$ *vs.* $v^{1/2}$ allows for the determination of k_1 and k_2 and thus the capacitive and diffusion contributions for each potential. At 1 mV s^{-1}, the result of this analysis is shown in Figure 8.8a. At this rate 83% of the total current (therefore, the capacity) are capacitive in nature. In the cathodic sweep, the diffusion-controlled currents appear during the initial Li^+ insertion at approximately 1.8 V, at the peak voltage, and at 1 V. In the anodic sweep, there are some diffusion-controlled contributions at the peak voltage but mostly around the end of the Li^+ de-insertion around 2 V. At 10 mV s^{-1} (Figure 8.8b) the charge storage is 94% capacitive. The change in kinetic behavior when the morphology of TiO_2 is varied from NC to NS can be observed by comparing the NS behavior to 7

nm NCs.[90] In this study, the capacitive contribution at 0.5 mV s^{-1} was 55%, with the diffusion contributions arising at the peak potentials. The *b*-value at the cathodic peak potential was 0.55 in contrast with 0.9 for the NS described here.

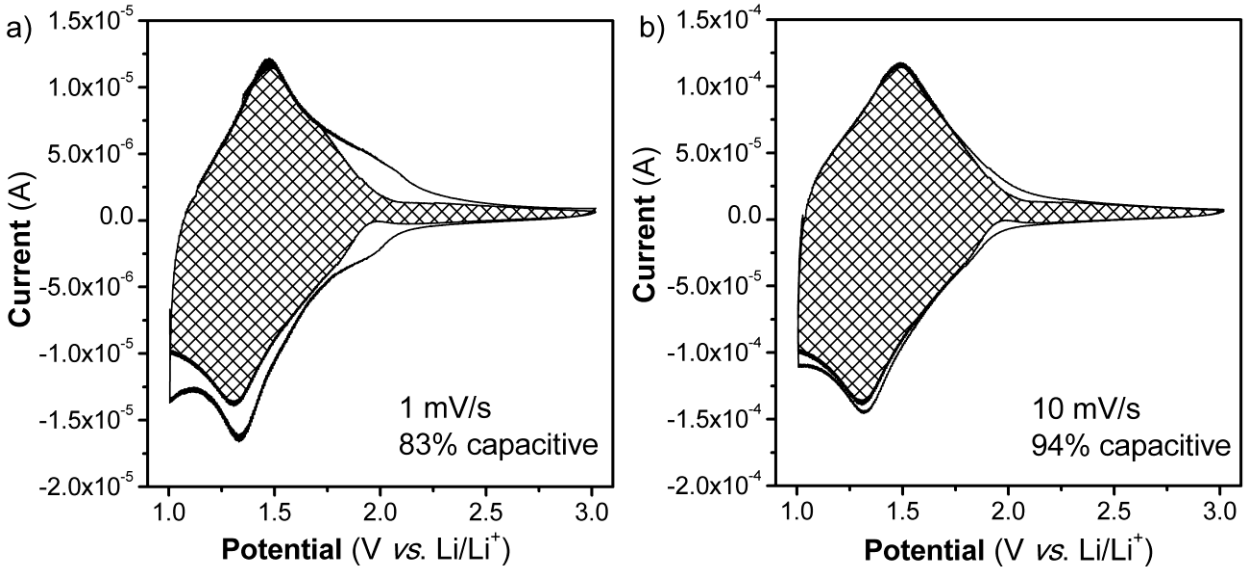

Figure 8.8. Separation of the capacitive and diffusion currents in TiO_2 NS cycled in Li^+, using sweep rates from 1-10 mV s^{-1}. **a)** The capacitive contribution (shaded) at 1 mV s^{-1} and **b)** at 10 mV s^{-1}.

There appear to be two different diffusion limitations in TiO_2 NS: one that appears at slow rates and another that appears at fast rates. The slow-rate diffusion is apparent in Figure 8.8a and constitutes a small percentage of the overall charge storage. The other can be visualized in Figure 8.6a or c and constitutes the total charge storage at high rates. The rationalization of two different diffusion limitations in electrochromic materials has been proposed by Bisquert.[124] In this model, there are two types of intercalation sites in a material: fast ones, that rapidly transport ions, and slow ones that act as ion-trapping sites. While the NS are considered to be essentially all-surface, the organization of the NS may play a large role in

determining the kinetics of the charge storage process and therefore intercalation-like behavior is likely taking place.

We also performed the electrochemical analysis of NS in a Na^+ non-aqueous electrolyte. The CVs for TiO_2 NS and NCs cycled in this manner are shown in Figure 8.9a. At 1 mV s^{-1}, the NS exhibit a CV that has broad peaks and a reversible capacity of 50 mAh g^{-1}. The NCs, on the other hand, exhibit a mostly rectangular CV except for a cathodic peak at 1 V. The capacity for the NC is 30 mAh g^{-1}. While in the case of the NC the capacity is probably only due to double-layer processes (for a TiO_2 surface area of 150 m^2 g^{-1}, the surface capacitance is 36 µF cm^{-2}), the peaks in the CV of the NS indicates that some redox reactions are taking place. The capacity of the NS as a function of sweep rate is shown in Figure 8.9b. The charge storage is highly reversible, and while the capacity is not as high as in the Li^+ electrolyte there is evidence that the open morphology of the NS allows for the storage of the bulkier Na^+.

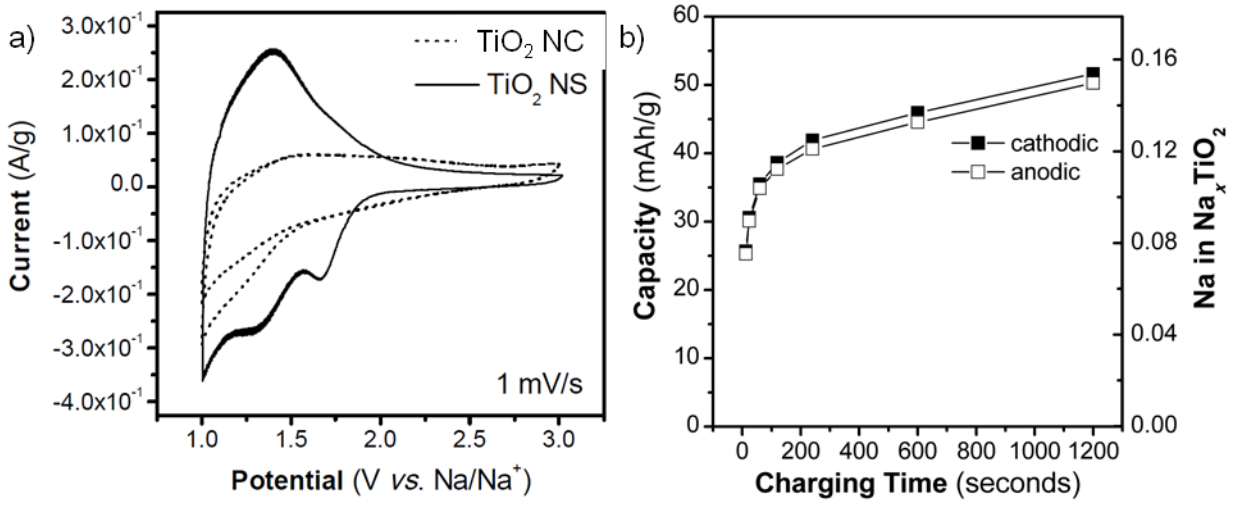

Figure 8.9. TiO_2 NS cycled in a Na^+ non-aqueous electrolyte. **a)** CV at 1 mV s^{-1} for NS and NC and **b)** capacity *vs.* sweep rate for NS.

8.4 Conclusions

TiO_2 NS exhibit highly reversible and high-rate charge storage in Li^+ and Na^+ non-aqueous electrolytes and their CVs are significantly different from those of nanocrystals. These results show that the 2D nanosheet morphology has a profound influence on the potentials and the reaction kinetics associated with energy storage in anatase. Due to the large exposed surface of the nanosheets, the rate limiting step for ion storage is a surface-limited process and solid-state ion diffusion is no longer rate-limiting, even at the peak voltage. As compared to nanoparticles, the peak voltage for lithium insertion in the nanosheets occurs 0.4 V lower. The peak voltage separation is also affected by the change in morphology. At a cyclic voltammetry sweep rate of 1 mV s^{-1}, the peak voltage separation is decreased from 0.36 in the nanoparticles to 0.13 V for the nanosheets indicating the highly reversible nature of the redox reaction. In addition, at a sweep rate of 100 mV s^{-1} the nanosheets retain approximately 70% of the capacity at 1 mV s^{-1} *vs.* 20% for the nanoparticles. Nanosheets possess several features that are advantageous for energy storage. The fact that the thickness is limited to a few atomic layers leads to high rate energy storage as all storage sites are located very close to or on the surface. Moreover, the openness of the structure enables charge storage to occur with larger ions such as sodium. The results of this fundamental study demonstrate that the nanosheet architecture allows for the tuning of energy storage properties beyond what is observed with other nanostructured morphologies.

Chapter 9. Conclusions

This dissertation describes the characterization and benefits of nanostructured materials for batteries and electrochemical capacitors. Previous research on nanomaterials for EES has focused on the improved kinetics with decreasing particle size. The research presented here reaffirms this idea as well as presents other advantages of these materials for high energy and high power EES devices. The nanostructured materials described— V_2O_5 aerogels, Nb_2O_5 nanocrystals, and TiO_2 nanosheets— enable energy storage mechanisms that are not possible in the bulk, either due to poor reversibility or poor rate capability. The characterization methods developed in the study of these materials, both *in situ* electrochemistry and *ex situ* physical characterization, are versatile and can be applied to the characterization of other materials for EES.

By utilizing V_2O_5 aerogels, a mesoporous, nanostructured morphology led to improved reversibility of a high-capacity Li^+ reaction. For both the crystalline bulk material and the aerogel, the first cycle capacity was over 1,000 mAh g^{-1} when cycled to 0.1 V. However, on subsequent cycles the capacity of the crystalline material decreased while that of the aerogel increased then stayed the same. The reversibility of the aerogel appears nestled in its ability to accommodate a large volume expansion from the storage of more than 5 Li^+/V_2O_5 along with any structural changes that occur. In this research, an energy storage reaction that is irreversible in the bulk is rendered reversible by using a highly porous material.

In Nb_2O_5, nanoscale dimensionality combined with appropriate atomic-scale structure led to intercalation pseudocapacitance, a mechanism whereby intercalation occurs in a capacitive manner. Intercalation pseudocapacitance results in high capacity and high power densities because the mechanism is not limited by solid-state lithium-ion diffusion. This results in kinetic behavior that is capacitive, similar to what is observed for EDLCs and surface redox pseudocapacitance mechanisms. However, in these latter mechanisms, surface area is the predominant material property that leads to high capacitance values. For intercalation

pseudocapacitance, crystallinity is also necessary, and may be more important than surface area in realizing the best high rate performance. The benefit of this mechanism for EES is that ultra-high surface area materials are not necessary, and that exposure of the surface to the electrolyte is not as critical as it is for EDLCs and surface redox pseudocapacitance. This should result in simple electrode architectures for advanced EES devices.

Finally, in the case of TiO_2 nanosheets the 2D morphology led to an entirely different behavior from TiO_2 nanocrystals. These results demonstrated that when materials are ultrathin, on the order of a few nm, their properties become even more unlike those of the bulk material. While TiO_2 nanocrystals exhibit redox peaks and peak voltage offsets at similar potentials to bulk anatase, the nanosheets store lithium ions at a lower voltage but with smaller peak offsets. This is likely due to the structural organization of several molecular layers of TiO_2 which results in different lithium-ion site energies from bulk TiO_2. It is now well-known that the 2D material graphene exhibits properties that are quite unlike the 3D structure, graphite. The electrochemical behavior of TiO_2 nanosheets suggests that 2D analogues of transition metal oxides will also differ significantly in their properties from the 3D structures.

The performance of EES technologies is limited by the materials that make up the electrodes and electrolyte. The nanostructured materials presented here exhibit properties that are significantly better than the currently-available technology in both capacity and power capability. One challenge for nanostructured materials in EES devices is that their integration in practical electrode architectures remains a challenge. Their enhanced reactivities extend to undesirable side reactions, and these must be mitigated while retaining the benefits of a nano-architecture. The challenge is greatest for ultrathin materials such as TiO_2 nanosheets and highly porous materials such as V_2O_5 aerogels, which will require advanced electrode architectures. Once these engineering challenges are met, nanostructured materials will lead to tremendous improvements in the current EES technologies and extend their use, particularly into grid-level energy storage.

Chapter 10. Future Work on Metal Organic Frameworks for Electrochemical Energy Storage

10.1 Introduction

Transition metal oxides represent the most well-studied class of energy storage materials. In the previous sections, V_2O_5, Nb_2O_5, and TiO_2 were investigated. In this section, a new class of materials is presented for EES: metal-organic framework (MOF) materials. There are several reasons why MOFs could be interesting for EES. As in other applications, the ability to design energy storage materials from the bottom-up is a tantalizing opportunity. A wide array of organic linkers can be joined with numerous transition metal oxides to yield new materials.[125] The linkers can be chosen so that they are electronically conductive for high power, and the incorporation of redox active sites or small nanoparticles would increase the energy density. Lastly, these materials offer a cheap alternative for EES materials since their composition consists primarily of carbon, oxygen, and hydrogen atoms. Minimizing the cost of EES is an important goal for the development of grid-scale energy storage.[27]

Recently, the synthesis of a class of MOFs utilizing the catecholate linker has been reported, termed CAT.[126] The catecholate in this case was 2, 3, 6, 7, 10, 11-hexahydroxytriphenylene ($H_{12}C_{18}O_6$, HHTP), which is a highly conjugated molecule. This type of moiety is interesting for EES because as a result of the conjugation, the CATs exhibit single crystal conductivity values between $1.8\text{-}2.1 \times 10^{-1}$ S cm^{-1}.(Ref. 126) In this section, the electrochemical behavior of a CAT MOF with a copper transition metal (Cu-CAT) will be examined for EES (Figure 10.1).

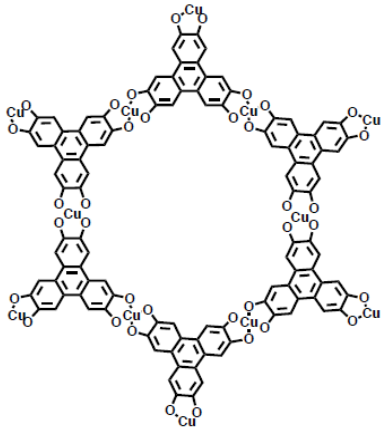

Figure 10.1. Molecular structure of the Cu-CAT.

10.2 Methods

Synthesis. The synthesis of various CATs was reported previously.[126] For the Cu-CAT, 1 equivalent of HHTP was combined with 2 equivalents of copper (II) acetate in water then heated at 85°C for 24 hours. The resulting crystals are ~40 nm in width and 100 nm in length (Figure 10.2). The color of the Cu-CAT powder is brown.

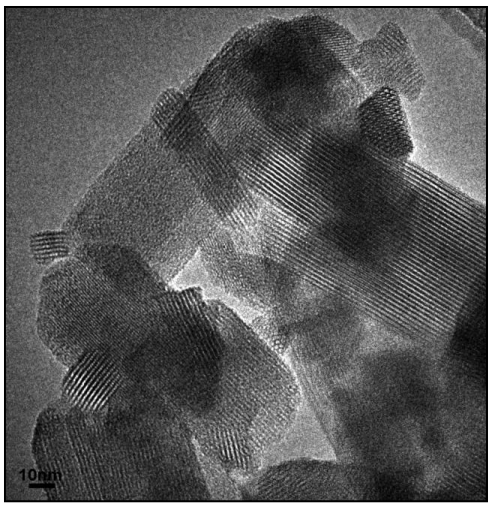

Figure 10.2. HR-TEM of the Cu-CAT demonstrates large, layered single crystals. The actual crystal structure of the Cu-CAT is currently unknown.

Electrochemical characterization. The electrochemical behavior of the Cu-CAT was investigated by using composite electrodes that consisted of 75 wt.% Cu-CAT, 15 wt.% carbon black (Ketjen black), and 15 wt.% PVDF. The powders were stirred with propylene carbonate to form a slurry that was then pasted onto a stainless steel mesh. The electrode was heated at 110°C for 12 hours to dry. Active material loading was between 0.4-1.4 mg cm^{-2}. The three-electrode electrochemical cell consisted of 1 M $LiClO_4$ in PC as the electrolyte and lithium foil as the reference and counter electrodes. Cyclic voltammetry was performed between 1.5 and 4 V and galvanostatic cycling was performed between 1.8 and 4 V.

10.3 Results and Discussion

The CVs at 10 mV s^{-1} for the Cu-CAT, the HHTP molecule, and Ketjen black in a Li^+ non-aqueous electrolyte are shown in Figure 10.3. The Ketjen black provides minimal capacity (14 mAh g^{-1}) and its charge storage is due to the double-layer adsorption process since there are no redox peaks in the CV. The HHTP molecule also exhibits a low capacity (33 mAh g^{-1}) but in this case, several cathodic and anodic peaks are present so the capacity is partially due to redox reactions. The Cu-CAT exhibits a broad cathodic current consisting of multiple overlapping peaks and there are four identifiable peaks in the anodic sweep. At this sweep rate, the capacity is 70 mAh g^{-1}. From the figure, it is evident that the electrochemical behavior of the Cu-CAT is not due to the conductive additive or the linker molecule by itself. The Cu-CAT is behaving like an entirely new material.

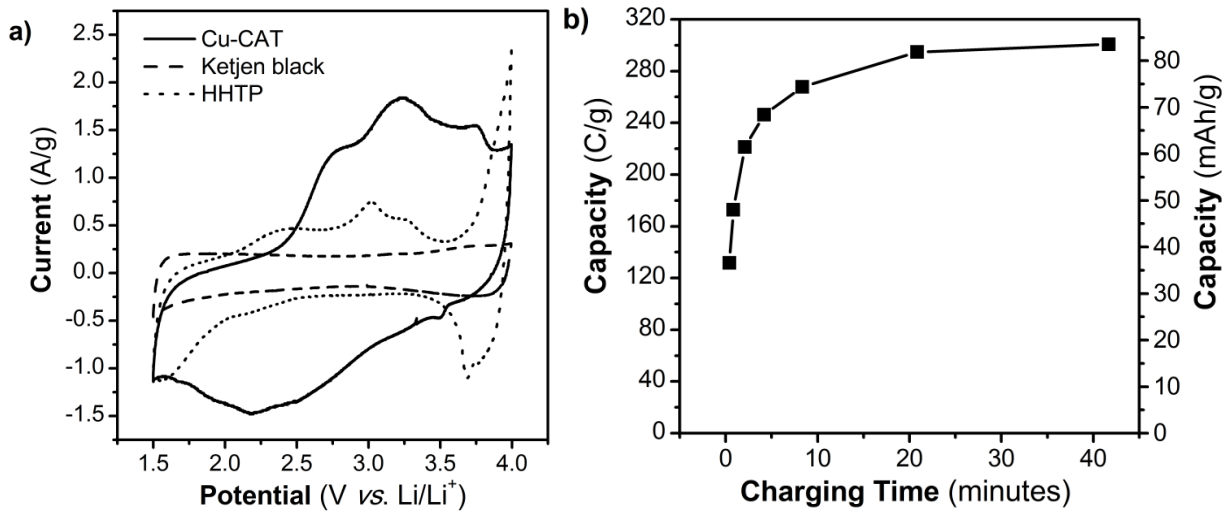

Figure 10.3. **a)** CVs at 10 mV s^{-1} for the Cu-CAT, Ketjen black, and HHTP in 1 M $LiClO_4$ in PC electrolyte. **b)** Capacity *vs*. charging time for the Cu-CAT at sweep rates of 1-100 mV s^{-1}.

The capacity of the Cu-CAT as a function of charging time (based on a 2.5 V potential window) is shown in Figure 10.3b. The plot exhibits a plateau region after 20 minutes corresponding to a stable capacity of 80 mAh g^{-1}. Diffusion limitations appear after 10 minutes and the capacity decreases quickly at faster timescales. The maximum capacity of 140 mAh g^{-1} was determined by performing a galvanostatic experiment at a C/83 rate (Figure 10.4) between 1.8 and 4 V. Even at this slow rate, the hysteresis between lithiation and delithiation is *ca*. 500 mV, implying the kinetics are fundamentally slow in this material. The maximum capacity is 140 mAh g^{-1}.

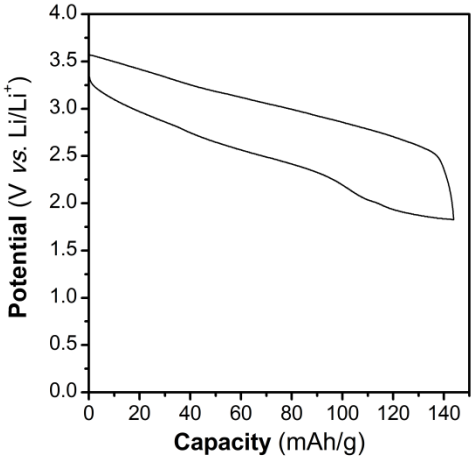

Figure 10.4. Galvanostatic cycling of the Cu-CAT composite electrode at a C/83 rate between 1.8 and 4 V.

The cycling stability of the Cu-CAT is shown in Figure 10.5 at a 1C rate. The capacity after 50 cycles is 78 mAh g^{-1}. It is interesting to note the increasing hysteresis in the galvanostatic plot in Figure 10.5a, which correlates to poorer reversibility as the amount of lithium in the material increases. The material exhibits essentially 100% coulombic efficiency over the 50 cycles, and minimal capacity fading is observed (Figure 10.5b). The first cycle capacity is higher than the second, but by the 50th cycle the first cycle lithiation capacity is fully recovered.

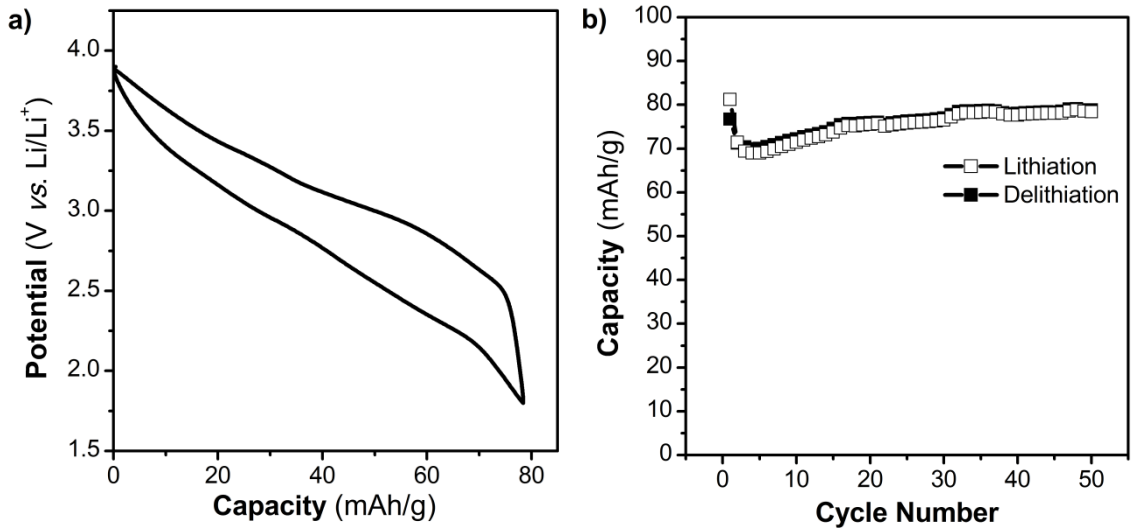

Figure 10.5. **a)** Galvanostatic cycling profile of the Cu-CAT at a 1C rate between 1.8 and 4 V, 50th cycle shown. **b)** Cycling stability for 50 cycles at a 1C rate.

10.4 Conclusions

The charge storage mechanism of the Cu-CAT is unknown because the crystal structure has not been identified. While its capacity and rate capability do not outperform the best lithium-ion battery materials, they are significantly better than the only other lithium insertion MOF reported in the literature, MIL-53. This MOF, which is based on the oxidation/reduction of Fe^{+3}/Fe^{+2}, can achieve a capacity of 70 mAh g^{-1} at a C/40 rate between 1.5 and 3.5 V. Approximately 56 mAh g^{-1} is achieved for a 1C rate.[127] The cycling stability of the Cu-CAT at the same rate is 76 mAh g^{-1}. Other MOFs reported for lithium-ion storage do so by undergoing a conversion reaction mechanism at low potentials that results in a decomposition of the MOF architecture.[128] The Cu-CAT is a promising material for EES due to the low cost and toxicity of the Cu transition metal. It shows good energy storage properties, with a capacity of ~80 mAh g^{-1} at a 1C rate that is stable over 50 cycles.

References

1. Melot, B. C. & Tarascon, J.-M. Design and Preparation of Materials for Advanced Electrochemical Storage. *Accounts of chemical research* **46**, 1226-1238 (2013).

2. Levin, A. Cartoon. *New Yorker* (1993).

3. Conway, B. E. *Electrochemical Supercapacitors: Scientific Fundamentals and Technological Applications*. (Kluwer-Academic: 1999).

4. James, F. A. J. L. Michael Faraday's First Law of Electrochemistry: How Context Develops New Knowledge. *Electrochemistry: Past and Present* 32–47 (1989).

5. Das Gupta, S. The Search for Portable Electricity: History of High Energy-Density Batteries. *Electrochemistry: Past and Present* 543–553 (1989).

6. Becker, H. E. Low voltage electrolytic capacitor. U.S. Patent #2800616 (1957).

7. Trasatti, S. & Buzzanca, G. Ruthenium dioxide: a new interesting electrode material. Solid state structure and electrochemical behaviour. *Electroanalytical chemistry and interfacial electrochemistry* **29**, App. 1–5 (1971).

8. Huggins, R. A. *Advanced Batteries: Materials Science Aspects*. (Springer: New York, 2009).

9. Frackowiak, E. & Béguin, F. Carbon materials for the electrochemical storage of energy in capacitors. *Carbon* **39**, 937–950 (2001).

10. Simon, P. & Gogotsi, Y. Materials for electrochemical capacitors. *Nature Materials* **7**, 845–54 (2008).

11. Rauda, I. E., Augustyn, V., Dunn, B. & Tolbert, S. H. Enhancing Pseudocapacitive Charge Storage in Polymer Templated Mesoporous Materials. *Accounts of chemical research* **46**, 1113-1124 (2013).

12. Grahame, D. C. The electrical double layer and the theory of electrocapillarity. *Chemical Reviews* **41**, 441–501 (1947).

13. Merlet, C. *et al.* On the molecular origin of supercapacitance in nanoporous carbon electrodes. *Nature materials* **11**, 306–10 (2012).

14. Long, J. W. *et al.* Asymmetric electrochemical capacitors—Stretching the limits of aqueous electrolytes. *MRS Bulletin* **36**, 513–522 (2011).

15. Gogotsi, Y. & Simon, P. True performance metrics in electrochemical energy storage. *Science* **334**, 917–918 (2011).

16. Lokhande, C. D., Dubal, D. P. & Joo, O.-S. Metal oxide thin film based supercapacitors. *Current Applied Physics* **11**, 255–270 (2011).

17. Choi, D., Blomgren, G. E. & Kumta, P. N. Fast and Reversible Surface Redox Reaction in Nanocrystalline Vanadium Nitride Supercapacitors. *Advanced Materials* **18**, 1178–1182 (2006).

18. Mastragostino, M., Arbizzani, C. & Soavi, F. Polymer-based supercapacitors. *Journal of Power Sources* **98**, 812–815 (2001).

19. Zhang, L. L. & Zhao, X. S. Carbon-based materials as supercapacitor electrodes. *Chemical Society Reviews* **38**, 2520–2531 (2009).

20. Fic, K., Frackowiak, E. & Béguin, F. Unusual energy enhancement in carbon-based electrochemical capacitors. *Journal of Materials Chemistry* **22**, 24213–24223 (2012).

21. Vincent, C. A. & Scrosati, B. *Modern Batteries: An Introduction to Electrochemical Power Sources*. (Butterworth-Heinemann: Oxford, 1997).

22. CAP-XX. *An introduction to BriteFlash*. (2009).

23. Huggins, R. Supercapacitors and electrochemical pulse sources. *Solid State Ionics* **134**, 179–195 (2000).

24. Wohlgemuth, J., Miller, J. & Sibley, L. B. *Investigation of Synergy Between Electrochemical Capacitors, Flywheels, and Batteries in Hybrid Energy Storage for PV Systems*. Sandia National Laboratories (1999).

25. Nocera, D. G. Personalized energy: the home as a solar power station and solar gas station. *ChemSusChem* **2**, 387–390 (2009).

26. Simon, P. & Gogotsi, Y. Charge storage mechanism in nanoporous carbons and its consequence for electrical double layer capacitors. *Philosophical Transactions of the Royal Society A* **368**, 3457–3467 (2010).

27. Dunn, B., Kamath, H. & Tarascon, J.-M. Electrical energy storage for the grid: a battery of choices. *Science* **334**, 928–35 (2011).

28. Eyer, J. & Corey, G. *Energy Storage for the Electricity Grid: Benefits and Market Potential Assessment Guide. A Study for the DOE Energy Storage Systems Program*. (Albuquerque, 2010).

29. Delmer, O., Balaya, P., Kienle, L. & Maier, J. Enhanced Potential of Amorphous Electrode Materials: Case Study of RuO_2. *Advanced Materials* **20**, 501–505 (2008).

30. Bruce, P. G., Scrosati, B. & Tarascon, J.-M. Nanomaterials for rechargeable lithium batteries. *Angewandte Chemie (International ed. in English)* **47**, 2930–2946 (2008).

31. Murphy, D. W. & Christian, P. A. Solid State Electrodes for High Energy Batteries. *Science* **205**, 651–656 (1979).

32. Tarascon, J.-M. & Armand, M. Issues and challenges facing rechargeable lithium batteries. *Nature* **414**, 359–367 (2001).

33. Goodenough, J. B. & Park, K.-S. The Li-ion rechargeable battery: a perspective. *Journal of the American Chemical Society* **135**, 1167–1176 (2013).

34. Yabuuchi, N. & Ohzuku, T. Novel lithium insertion material of $LiCo_{1/3}Ni_{1/3}Mn_{1/3}O_2$ for advanced lithium-ion batteries. *Journal of Power Sources* **119-121**, 171–174 (2003).

35. Park, S., Kang, S., Johnson, C., Amine, K. & Thackeray, M. Lithium–manganese–nickel-oxide electrodes with integrated layered–spinel structures for lithium batteries. *Electrochemistry Communications* **9**, 262–268 (2007).

36. Thackeray, M. M. *et al.* Li_2MnO_3-stabilized Li*M*O2 (*M* = Mn, Ni, Co) electrodes for lithium-ion batteries. *Journal of Materials Chemistry* **17**, 3112 (2007).

37. Tripathi, R., Ramesh, T. N., Ellis, B. L. & Nazar, L. F. Scalable synthesis of tavorite $LiFeSO_4F$ and $NaFeSO_4F$ cathode materials. *Angewandte Chemie (International ed. in English)* **49**, 8738–42 (2010).

38. Kraytsberg, A. & Ein-Eli, Y. Higher, Stronger, Better… A Review of 5 Volt Cathode Materials for Advanced Lithium-Ion Batteries. *Advanced Energy Materials* **2**, 922–939 (2012).

39. Poizot, P., Laruelle, S., Grugeon, S., Dupont, L. & Tarascon, J.-M. Nano-sized transition-metal oxides as negative-electrode materials for lithium-ion batteries. *Nature* **407**, 496–499 (2000).

40. Cabana, J., Monconduit, L., Larcher, D. & Palacín, M. R. Beyond intercalation-based Li-ion batteries: the state of the art and challenges of electrode materials reacting through conversion reactions. *Advanced Materials* **22**, E170–E192 (2010).

41. Tarascon, J.-M. *et al.* New concepts for the search of better electrode materials for rechargeable lithium batteries. *Comptes Rendus Chimie* **8**, 9–15 (2005).

42. Poizot, P., Laruelle, S., Grugeon, S. & Tarascon, J.-M. Rationalization of the Low-Potential Reactivity of 3d-Metal-Based Inorganic Compounds toward Li. *Journal of The Electrochemical Society* **149**, A1212–A1217 (2002).

43. Li, H., Balaya, P. & Maier, J. Li-storage via heterogeneous reaction in selected binary metal fluorides and oxides. *Journal of The Electrochemical Society* **151**, A1878–A1885 (2004).

44. Doe, R. E., Persson, K. A., Meng, Y. S. & Ceder, G. First-Principles Investigation of the Li–Fe–F Phase Diagram and Equilibrium and Nonequilibrium Conversion Reactions of Iron Fluorides with Lithium. *Chemistry of Materials* **20**, 5274–5283 (2008).

45. Dalverny, A.-L., Filhol, J.-S. & Doublet, M.-L. Interface electrochemistry in conversion materials for Li-ion batteries. *Journal of Materials Chemistry* **21**, 10134–10142 (2011).

46. Tang, P. E., Sakamoto, J. S., Baudrin, E. & Dunn, B. V_2O_5 aerogel as a versatile host for metal ions. *Journal of Non-Crystalline Solids* **350**, 67–72 (2004).

47. Le, D. B. *et al.* High Surface Area V_2O_5 Aerogel Intercalation Electrodes. *Journal of the Electrochemical Society* **143**, 2099–2104 (1996).

48. Sakamoto, J. S. & Dunn, B. Vanadium Oxide-Carbon Nanotube Composite Electrodes for Use in Secondary Lithium Batteries. *Journal of the Electrochemical Society* **149**, A26–A30 (2002).

49. Dong, W., Rolison, D. R. & Dunn, B. Electrochemical Properties of High Surface Area Vanadium Oxide Aerogels. *Electrochemical and Solid-State Letters* **3**, 457–459 (2000).

50. West, K., Zachau-Christiansen, B., Jacobsen, T. & Skaarup, S. Vanadium oxide xerogels as electrodes for lithium batteries. *Electrochimica Acta* **38**, 1215–1220 (1993).

51. Petkov, V. *et al.* Structure of $V_2O_5{\cdot}nH_2O$ Xerogel Solved by the Atomic Pair Distribution Function Technique. *Journal of the American Chemical Society* **124**, 10157–10162 (2002).

52. Mansour, A. N., Dallek, S., Smith, P. H. & Baker, W. M. Thermogravimetry and X-Ray Absorption Spectroscopy Study of Heated $V_2O_5{\cdot}nH_2O$ Aerogels and Ambigels. *Journal of the Electrochemical Society* **149**, A1589–A1597 (2002).

53. Delmas, C., Cognacauradou, H., Cocciantelli, J., Menetrier, M. & Doumerc, J. The $Li_xV_2O_5$ system: An overview of the structure modifications induced by the lithium intercalation. *Solid State Ionics* **69**, 257–264 (1994).

54. Liu, P., Lee, S.-H., Tracy, C.E., Turner, J.A. Stable cycling of thin-film vanadium oxide electrodes between 4 and 0 V in lithium batteries. *Journal of Power Sources* **119-121**, 305–309 (2003).

55. Almeida, E. C., Abbate, M. & Rosolen, J. M. Formation of Li_2O in a chemically Li-intercalated V_2O_5 xerogel. *Solid State Ionics* **140**, 241–248 (2001).

56. Poizot, P., Laruelle, S., Grugeon, S., Dupont, L. & Tarascon, J.-M. From the vanadates to 3d-metal oxides negative electrodes. *Ionics* **6**, 321–330 (2000).

57. Chaput, F., Dunn, B., Fuqua, P. & Salloux, K. Synthesis and characterization of vanadium oxide aerogels. *Journal of Non-Crystalline Solids* **188**, 11–18 (1995).

58. Umeda, G. A. *et al.* Protection of lithium metal surfaces using tetraethoxysilane. *Journal of Materials Chemistry* **21**, 1593–1599 (2011).

59. Sudant, G., Baudrin, E., Dunn, B. & Tarascon, J.-M. Synthesis and Electrochemical Properties of Vanadium Oxide Aerogels Prepared by a Freeze-Drying Process. *Journal of The Electrochemical Society* **151**, A666–A671 (2004).

60. Gachot, G. *et al.* Deciphering the multi-step degradation mechanisms of carbonate-based electrolyte in Li batteries. *Journal of Power Sources* **178**, 409–421 (2008).

61. Laruelle, S. *et al.* On the Origin of the Extra Electrochemical Capacity Displayed by MO/Li Cells at Low Potential. *Journal of The Electrochemical Society* **149**, A627–A634 (2002).

62. Cohen, Y. S. & Aurbach, D. Surface films phenomena on vanadium-pentoxide cathodes for Li and Li-ion batteries: in situ AFM imaging. *Electrochemistry Communications* **6**, 536–542 (2004).

63. Fan, H. *et al.* Modulus-density scaling behaviour and framework architecture of nanoporous self-assembled silicas. *Nature materials* **6**, 418–423 (2007).

64. Lee, S.-H. *et al.* Reversible Lithium-Ion Insertion in Molybdenum Oxide Nanoparticles. *Advanced Materials* **20**, 3627–3632 (2008).

65. Wang, F. *et al.* Conversion reaction mechanisms in lithium ion batteries: study of the binary metal fluoride electrodes. *Journal of the American Chemical Society* **133**, 18828–18836 (2011).

66. Latimer, W. M. *The Oxidation States of the Elements and Their Potentials in Aqueous Solutions*. (Prentice Hall: New York, 1952).

67. Wu, Q.-H., Thißen, A. & Jaegermann, W. Photoelectron spectroscopic study of Li intercalation into V2O5 thin films. *Surface Science* **578**, 203–212 (2005).

68. Dedryvère, R. *et al.* Contribution of X-ray Photoelectron Spectroscopy to the Study of the Electrochemical Reactivity of CoO toward Lithium. *Chemistry of Materials* **16**, 1056–1061 (2004).

69. Benedek, R., Vaughey, J. & Thackeray, M. M. Theory of Overlithiation Reaction in LiMO_2 Battery Electrodes. *Chemistry of Materials* **18**, 1296–1302 (2006).

70. Vaughey, J. T. *et al.* Studies of layered lithium metal oxide anodes in lithium cells. *Journal of Power Sources* **174**, 1052–1056 (2007).

71. Conway, B. E. & Pell, W. G. Double-layer and pseudocapacitance types of electrochemical capacitors and their applications to the development of hybrid devices. *Journal of Solid State Electrochemistry* **7**, 637–644 (2003).

72. Galizzioli, D., Tantardini, F. & Trasatti, S. Ruthenium dioxide: a new electrode material. I. Behaviour in acid solutions of inert electrolytes. *Journal of Applied Electrochemistry* **4**, 57–67 (1974).

73. Dmowski, W., Egami, T., Swider-Lyons, K. E., Love, C. T. & Rolison, D. R. Local Atomic Structure and Conduction Mechanism of Nanocrystalline Hydrous RuO_2 from X-ray Scattering. *The Journal of Physical Chemistry B* **106**, 12677–12683 (2002).

74. Liu, Y., Zhou, F. & Ozolins, V. Ab Initio Study of the Charge-Storage Mechanisms in RuO_2 -Based Electrochemical Ultracapacitors. *Journal of Physical Chemistry C* **116**, 1450–1457 (2012).

75. Long, J. W., Swider, K. E., Merzbacher, C. I. & Rolison, D. R. Voltammetric Characterization of Ruthenium Oxide-Based Aerogels and Other RuO_2 Solids: The Nature of Capacitance in Nanostructured Materials. *Langmuir* **15**, 780–785 (1999).

76. Reichman, B. & Bard, A. J. Electrochromism at Niobium Pentoxide Electrodes in Aqueous and Acetonitrile Solutions. *Journal of The Electrochemical Society* 241–242 (1980).

77. Reichman, B. & Bard, A. J. The application of Nb_2O_5 as a cathode in nonaqueous lithium cells. *Journal of The Electrochemical Society* **128**, 344–346 (1981).

78. Kodama, R., Terada, Y., Nakai, I., Komaba, S. & Kumagai, N. Electrochemical and In Situ XAFS-XRD Investigation of Nb_2O_5 for Rechargeable Lithium Batteries. *Journal of The Electrochemical Society* **153**, A583–A588 (2006).

79. Orel, B., Maček, M., Grdadolnik, J. & Meden, A. In situ UV-Vis and ex situ IR spectroelectrochemical investigations of amorphous and crystalline electrochromic Nb_2O_5 films in charged/discharged states. *Journal of Solid State Electrochemistry* **2**, 221–236 (1998).

80. Ghodbane, O., Pascal, J.-L. & Favier, F. Microstructural effects on charge-storage properties in MnO_2-based electrochemical supercapacitors. *ACS applied materials & interfaces* **1**, 1130–1139 (2009).

81. Brezesinski, K. *et al.* Pseudocapacitive Contributions to Charge Storage in Highly Ordered Mesoporous Group V Transition Metal Oxides with Iso-Oriented Layered Nanocrystalline Domains. *Journal of the American Chemical Society* **132**, 6982–6990 (2010).

82. Nowak, I. & Ziolek, M. Niobium Compounds: Preparation, Characterization, and Application in Heterogeneous Catalysis. *Chemical reviews* **99**, 3603–3624 (1999).

83. Ohzuku, T., Sawai, K. & Hirai, T. Electrochemistry of L-niobium pentoxide a lithium/non-aqueous cell. *Journal of Power Sources* **19**, 287–299 (1987).

84. Rosario, A. V. & Pereira, E. C. Influence of the crystallinity on the Li^+ intercalation process in Nb_2O_5 films. *Journal of Solid State Electrochemistry* **9**, 665–673 (2005).

85. Schmitt, M. & Aegerter, M. A. Electrochromic properties of pure and doped Nb2O5 coatings and devices. *Electrochimica Acta* **46**, 2105–2111 (2001).

86. Kumagai, N., Koishikawa, Y., Komaba, S. & Koshiba, N. Thermodynamics and Kinetics of Lithium Intercalation into Nb2O5 Electrodes for a 2 V Rechargeable Lithium Battery. *Journal of The Electrochemical Society* **146**, 3203–3210 (1999).

87. Kumagai, N., Ishiyama, I. & Tanno, K. Electrochemical and structural characteristics of niobium (V) oxide in a rechargeable lithium battery. *Journal of Power Sources* **20**, 193 – 198 (1987).

88. Ardizzone, S., Fregonara, G. & Trasatti, S. “Inner” and “outer” active surface of RuO_2 electrodes. *Electrochimica Acta* **35**, 263–267 (1989).

89. Baronetto, D., Krstajic, N. & Trasatti, S. Reply to "Note on a method to interrelate inner and outer electrode areas" by H. Vogt. *Electrochimica Acta* **39**, 2359–2362 (1994).

90. Wang, J., Polleux, J., Lim, J. & Dunn, B. Pseudocapacitive Contributions to Electrochemical Energy Storage in TiO_2 (Anatase) Nanoparticles. *Journal of Physical Chemistry C* **111**, 14925–14931 (2007).

91. Ma, S.-B. *et al.* Electrochemical properties of manganese oxide coated onto carbon nanotubes for energy-storage applications. *Journal of Power Sources* **178**, 483–489 (2008).

92. Jirkovský, J., Makarova, M. & Krtil, P. The Effect of Coherent Domain Size on the Insertion Activity of Nanocrystalline RuO_2. *Journal of The Electrochemical Society* **152**, A1613–A1619 (2005).

93. Chervin, C. N. *et al.* Making the most of a scarce platinum-group metal: conductive ruthenia nanoskins on insulating silica paper. *Nano letters* **9**, 2316–2321 (2009).

94. Cava, R. *et al.* Electrical and magnetic properties of $Nb_2O_{5-\delta}$ crystallographic shear structures. *Physical Review B* **44**, 6973–6981 (1991).

95. Filho, D. de A. B., Franco, D. W., Filho, P. P. A. & Alves, O. L. Niobia films: surface morphology, surface analysis, photoelectrochemical properties and crystallization process. *Journal of Materials Science* **33**, 2607–2616 (1998).

96. Maček, M., Orel, B. & Opara Kraošvec, U. The Effect of Lithiation on the Electrochromism of Sol-Gel Derived Niobium Oxide Films. *Journal of The Electrochemical Society* **144**, 3002–3010 (1997).

97. Kılıç, C. & Zunger, A. N-Type Doping of Oxides By Hydrogen. *Applied Physics Letters* **81**, 73 (2002).

98. Come, J., Taberna, P.-L., Hamelet, S., Masquelier, C. & Simon, P. Electrochemical Kinetic Study of $LiFePO_4$ Using Cavity Microelectrode. *Journal of The Electrochemical Society* **158**, A1090–A1093 (2011).

99. Lindström, H. *et al.* Li^+ Ion Insertion in TiO_2 (Anatase). 2. Voltammetry on Nanoporous Films. *The Journal of Physical Chemistry B* **101**, 7717–7722 (1997).

100. Park, M., Zhang, X., Chung, M., Less, G. B. & Sastry, A. M. A review of conduction phenomena in Li-ion batteries. *Journal of Power Sources* **195**, 7904–7929 (2010).

101. Conway, B. E. Transition from "Supercapacitor" to "Battery" Behavior in Electrochemical Energy Storage. *Journal of The Electrochemical Society* **138**, 1539–1548 (1991).

102. Xia, H., Lu, L. & Ceder, G. Substrate effect on the microstructure and electrochemical properties of $LiCoO_2$ thin films grown by PLD. *Journal of Alloys and Compounds* **417**, 304–310 (2006).

103. Zhang, N. *et al.* Facile preparation of nanocrystalline $Li_4Ti_5O_{12}$ and its high electrochemical performance as anode material for lithium-ion batteries. *Electrochemistry Communications* **13**, 654–656 (2011).

104. Kato, K. & Tamura, S. Die kristallstruktur von *T*-Nb_2O_5. *Acta Crystallographica* **B31**, 673 (1975).

105. Liu, C.-P., Zhou, F. & Ozolins, V. First Principles Study for Lithium Intercalation and Diffusion Behavior in Orthorhombic Nb_2O_5 Electrochemical Supercapacitor. *American Physical Society Meeting* (2012).<http://meetings.aps.org/link/BAPS.2012.MAR.B26.3>

106. Kim, J. W., Augustyn, V. & Dunn, B. The Effect of Crystallinity on the Rapid Pseudocapacitive Response of Nb_2O_5. *Advanced Energy Materials* **2**, 141–148 (2012).

107. Zheng, J. P., Cygan, P. J. & Jow, T. R. Hydrous Ruthenium Oxide as an Electrode Material for Electrochemical Capacitors. *Journal of The Electrochemical Society* **142**, 2699–2703 (1995).

108. Han, X., Kuang, Q., Jin, M., Xie, Z. & Zheng, L. Synthesis of titania nanosheets with a high percentage of exposed (001) facets and related photocatalytic properties. *Journal of the American Chemical Society* **131**, 3152–3153 (2009).

109. Wu, B., Guo, C., Zheng, N., Xie, Z. & Stucky, G. D. Nonaqueous Production of Nanostructured Anatase with High-Energy Facets. *Journal of the American Chemical Society* **130**, 17563–17567 (2008).

110. Chemseddine, A. & Moritz, T. Nanostructuring Titania: Control over Nanocrystal Structure, Size, Shape, and Organization. *European Journal of Inorganic Chemistry* **1999**, 235–245 (1999).

111. Hengerer, R., Kavan, L., Krtil, P. & Grätzel, M. Orientation Dependence of Charge-Transfer Processes on TiO_2 (Anatase) Single Crystals. *Journal of The Electrochemical Society* **147**, 1467–1472 (2000).

112. Vittadini, A. & Casarin, M. Ab initio modeling of TiO_2 nanosheets. *Theoretical Chemistry Accounts* **120**, 551–556 (2008).

113. Ding, S. *et al.* Graphene-supported anatase TiO_2 nanosheets for fast lithium storage. *Chemical communications* **47**, 5780–5782 (2011).

114. Chen, J. S., Liu, H., Qiao, S. Z. & Lou, X. W. Carbon-supported ultra-thin anatase TiO2 nanosheets for fast reversible lithium storage. *Journal of Materials Chemistry* **21**, 5687–5692 (2011).

115. Wu, H. B., Lou, X. W. & Hng, H. H. Titania nanosheets hierarchically assembled on carbon nanotubes as high-rate anodes for lithium-ion batteries. *Chemistry - A European Journal* **18**, 3132–3135 (2012).

116. Dylla, A. G., Xiao, P., Henkelman, G. & Stevenson, K. J. Morphological Dependence of Lithium Insertion in Nanocrystalline TiO_2(B) Nanoparticles and Nanosheets. *Journal of Physical Chemistry Letters* **3**, 2015–2019 (2012).

117. Zukalová, M., Kalbáč, M., Kavan, L., Exnar, I. & Graetzel, M. Pseudocapacitive Lithium Storage in TiO_2(B). *Chemistry of Materials* **17**, 1248–1255 (2005).

118. Li, J., Tang, Z. & Zhang, Z. H-titanate nanotube: a novel lithium intercalation host with large capacity and high rate capability. *Electrochemistry Communications* **7**, 62–67 (2005).

119. Wei, M., Wei, K., Ichihara, M. & Zhou, H. High rate performances of hydrogen titanate nanowires electrodes. *Electrochemistry Communications* **10**, 1164–1167 (2008).

120. Alvarez-Ramirez, F. & Ruiz-Morales, Y. Ab Initio Molecular Dynamics Calculations of the Phase Transformation Mechanism for the Formation of TiO_2 Titanate-Type Nanosheets from Anatase. *Chemistry of Materials* **19**, 2947–2959 (2007).

121. Orzali, T., Casarin, M., Granozzi, G., Sambi, M. & Vittadini, A. Bottom-Up Assembly of Single-Domain Titania Nanosheets on (1×2)-Pt(110). *Physical Review Letters* **97**, 156101 (2006).

122. Casarin, M., Vittadini, A. & Selloni, A. First Principles Study of Hydrated/Hydroxylated TiO_2 Nanolayers: From Isolated Sheets to Stacks and Tubes. *ACS nano* **3**, 317–324 (2009).

123. Liu, T.-C., Pell, W. G., Conway, B. E. & Roberson, S. L. Behavior of Molybdenum Nitrides as Materials for Electrochemical Capacitors. *Journal of The Electrochemical Society* **145**, 1882–1888 (1998).

124. Bisquert, J. Analysis of the kinetics of ion intercalation. Ion trapping approach to solid-state relaxation processes. *Electrochimica Acta* **47**, 2435–2449 (2002).

125. Yaghi, O. M. *et al.* Reticular synthesis and the design of new materials. *Nature* **423**, 705–714 (2003).

126. Hmadeh, M. *et al.* New Porous Crystals of Extended Metal-Catecholates. *Chemistry of Materials* **24**, 3511–3513 (2012).

127. Férey, G. *et al.* Mixed-valence Li/Fe-based metal-organic frameworks with both reversible redox and sorption properties. *Angewandte Chemie (International ed. in English)* **46**, 3259–3263 (2007).

128. Morozan, A. & Jaouen, F. Metal organic frameworks for electrochemical applications. *Energy & Environmental Science* **5**, 9269–9290 (2012).